University of Windsor
Scholarship at UWindsor

Electronic Theses and Dissertations

2010

Robust Vision-based Thermal Control Systems with Industrial Applications

Tie Bao Yang
University of Windsor

Follow this and additional works at: http://scholar.uwindsor.ca/etd

Recommended Citation

Yang, Tie Bao, "Robust Vision-based Thermal Control Systems with Industrial Applications" (2010). *Electronic Theses and Dissertations.* Paper 441.

Robust Vision-based Thermal Control Systems with Industrial Applications

by

Tie Bao Yang

A Dissertation

Submitted to the Faculty of Graduate Studies

through the Department of Electrical and Computer Engineering

in partial fulfillment of the requirements for

the Degree of Doctor of Philosophy at the

University of Windsor.

Windsor, Ontario, Canada

2009

Robust Vision-based Thermal Control Systems with Industrial Applications
by
Tie Bao Yang

APPROVED BY:

_____

Dr. C.-Y. Su, External Examiner
Concordia University

_____

Dr. J. Sokolowski
Department of Mechanical, Automotive & Materials Engineering

_____

Dr. N. Kar
Department of Electrical & Computer Engineering

_____

Dr. K. Tepe
Department of Electrical & Computer Engineering

_____

Dr. X. Chen, Co-Advisor
Department of Electrical & Computer Engineering

_____

Dr. H. Hu, Co-Advisor
Department of Mechanical, Automotive & Materials Engineering

_____

Dr. S. Nkurunziza, Chair of Defense
Department of Mathematics and Statistics

Author's Declaration of Originality

I hereby certify that I am the sole author of this dissertation and that no part of this dissertation has been published or submitted for publication.

I certify that, to the best of my knowledge, my dissertation does not infringe upon anyone's copyright nor violate any proprietary rights and that any ideas, techniques, quotations, or any other material from the work of other people included in my dissertation, published or otherwise, are fully acknowledged in accordance with the standard referencing practices. Furthermore, to the extent that I have included copyrighted material that surpasses the bounds of fair dealing within the meaning of the Canada Copyright Act, I certify that I have obtained a written permission from the copyright owner(s) to include such material(s) in my dissertation and have included copies of such copyright clearances to my appendix.

I declare that this is a true copy of my dissertation, including any final revisions, as approved by my dissertation committee and the Graduate Studies office, and that this dissertation has not been submitted for a higher degree to any other University or Institution.

Abstract

As multimodal camera networks have been deployed in various environment, image fusion is playing a critical role for better visual perception and process parameter measurement. The objective of the dissertation is to design robust vision-based thermal control systems to tolerate uncertainties for industrial automaton. To be specific, two new methods have been proposed, one for robust shape fitting in visual images and another for packet loss recovery in thermal images.

Firstly, an adaptive curve fitting technique is proposed based on prediction error sum of squares for the sampled data set containing outliers. The method converges very fast and can achieve superaccuracy under certain conditions when compared with other algorithms. The method is applied to estimate an optimal curve equation of a casting die in the visual images.

Secondly, the thermal image loss generated by network traffic from camera nodes to fusion center is modeled as a Markov chain. A graph cuts method is proposed to recover the loss based on thermal pattern classification. Simulation results show that thermal information can be partially retrieved, which may greatly increase the robustness of a thermal management system.

The proposed methods are tested with a laboratory die casting process simulator with two visual cameras and one thermal camera. A simple fuzzy PID controller is designed to integrate the visual sensors into a control loop. The experimental results show that the homogeneity of the temperature distribution in a die may become achievable through the vision based thermal control system.

To

My wife Yi Han and son Kevin

Acknowledgements

In the opening lines of "A Tale of Two Cities" Charles Dickens wrote, "It was the best of times, it was the worst of times; it was the age of wisdom, it was the age of foolishness." When I first came to Canada after 9·11, the dot-com bubble burst. So I decided to go to school. When I am about to graduate, here comes the financial market meltdown. However, under no circumstances should I regret to fulfill my dream of getting the degree, and nothing can compare to what I have learned from my great teachers in this school and beyond.

First and for most, I would like to express my sincere gratitude to my supervisors, Drs. Xiang Chen and Henry Hu, whose guidance and support made the completion of this dissertation possible. Their insightful thoughts, enthusiasm and confidence have had a great impact on me both academically and professionally. I highly appreciate all they have done to help me in the hard times. They are among the ones who have changed my life course toward the right way.

Very special recognition needs to be given to Dr. Chun-Yi Su, the external examiner, for spending considerable time evaluating the design, experiment and analysis in the dissertation. He is always willing to support when I need help.

I have been fortunate to have Dr. Jerry Sokolowski as the outside reader whose understanding of casting industry made him an invaluable resource throughout the research. I appreciate every thoughtful question and valuable advice toward the completion of this project.

Extra special thanks are due to my committee members, Drs. Narayan Kar and Kemal Tepe. They tolerated the mistakes and ambiguities I have made in my research

and presentation, and encouraged me to improve every time. Thank you for your kindness, encouragement and inspiration. My special thanks also go to Dr. Sévérien Nkurunziza for chairing my defense. I have taken two statistic courses from him, and the courses are very helpful to this research.

My thanks are also due to Dr. Maher Sid-Ahmed, the department head, for his help during my graduate studies. I also highly appreciate the generous help from Mr. Frank Cicchello, Mr. Don Tersigni, the department technicians, and Ms. Andria Ballo, Ms. Shelby Marchand, the department secretaries.

I am also in debt to Dr. Yeou-li Chu and Patrick Cheng at Roybi Die Casting (USA) Inc. for not only sharing their unique experience and knowledge on die casting but also providing equipment for this research.

"It is a far, far better thing that I do, than I have ever done; it is a far, far better rest that I go to than I have ever known," that book concludes with this great passage. Once again, thank you all, mentioned here or not, for the good things I shall carry forward.

Contents

List of Figures

List of Tables

Chapter 1

Introduction

This chapter contains a brief introduction to die casting processes, including structure of a casting machine and four stages of a complete casting cycle. Research motivation and literature survey are discussed thereinafter. The outline of this dissertation is provided in the last section.

1.1   Background

It is argued that robust computer vision is the key bottleneck to the development of autonomous systems such as industrial automation in a less structured or unstructured real environment [1]. Furthermore, the manufacturing processes are now mostly operated and coordinated through industrial communication networks which bring extra difficulties to the visual sensor network based control.

In the past, multimodal visual sensors, which may contain a large number of thermal cameras and ordinary visual cameras, have been widely deployed in video surveillance. A great amount of algorithms have been proposed to fuse thermal and visual image together to generate one picture containing information of both images

for better human perception. However, there are big differences in camera usage between surveillance and industrial process. For a multimodal camera network that monitoring human activities on the street, the image of a single human being only occupies a small portion of the entire image. While for the industrial thermal control, the image of the target has to be large enough for accurate temperature measurement. Therefore, the algorithms for video surveillance have to be carefully examined before it can be applied to an industrial process, since they are built for different purpose.

Deployment of multimodal visual sensors in a manufacturing factory may have some special challenges that video surveillance does not. Although the surveillance images are transferred through LAN/WAN for a large amount of nodes, the loss of one or two data packets or even one or two image frames will not cause any serious problems to its observer since human beings possess rather fantastic reasoning ability than computers. However, things are quite different for industrial processes. The loss of even one packet may cause the failure of the whole system, let alone the whole image frame. For example, if thermal image, which conveys the temperature signal, is used as a temperature feedback for a thermal management system, the measurement may become inaccurate when there are packet losses in the thermal image. Malfunction may be caused by the inaccuracy. Furthermore, a factory is usually noisier than the street in terms of the working environment for a camera. There may be thousands of machines running at the same time in a factory which may have electromagnetic interference with the camera, and hence further corrupts the performance of the vision guided control system.

As theories on computer vision advance, vision-guided control is a relatively new addition to the research field of systems and control. In the wake of the realities,

fundamental research has to be conducted with a focus on developing new methods to guarantee operation performance of the vision-based control systems in a network environment. Two of the fundamental questions can be formulated as:

1. Is it possible to localize an object accurately in a visual image that contains lots of outliers/noise?

2. Can the thermal image be partially recovered after a lossy network?

The answer to these questions will lead to build a robust vision based thermal control system. The purpose of this research is to integrate manufacturing systems with vision sensor networks as feedback and/or feedforward signals, specifically, to develop robust network based intelligent control algorithms for vision guided industrial processes, based on techniques from image processing, pattern recognition, computer vision, and large-scale computing.

1.2   Motivation

The research is motivated from an industrial problem. High pressure die casting is a manufacturing process accomplished by injecting molten metal into a reusable mould, called the die, in which the metal solidifies rapidly into nearly net-shape, smooth-surface components such as engine blocks and transmission cases. A die usually consists of two sections: one is stationary (fixed die half) while another is movable (injector die half) to permit easy removal of the finished castings [2, 3, 4]. The schematic view of a die-casting machine is depicted in Figure 1.1. A complete casting cycle can be roughly divided into four stages.

1. Cavity filling: The two die halves are clamped together tightly by a die casting machine at the start of each casting cycle. Molten alloy is poured into the shot sleeve, and then injected into the die cavity by the piston. The time for cavity filling varies from 5 ms to 150 ms dependent on the casting size.

2. Solidification: The molten metal solidifies in the die cavity under certain applied pressure, usually from 10 to 30 MPa, to reduce the formation of the porosity and to increase the dimensional accuracy of the part. The die is also chilled by internal cooling water lines to yield high productivity.

3. Casting Ejection: After the molten alloy solidifies, the die halves are separated; the ejectors that are usually driven by hydraulic power expel the casting part, and the part is taken out of platens by a robot or operator.

4. Die Lubrication: The surface of the die is then sprayed by water-based lubricant, and is blown by compressed air in order to further reduce the temperature of the die and oil its surface for next cycle.

Basically there are two functions for a casting die. One is to retain the desired shape of the casting, and another is to remove the heat from the molten metal in a reasonable amount of time. Therefore, the die plays a critical role in removing heat from the molten metal. Proper control of die temperature is essential for producing superior quality components and yielding high production rates.

A die may consist of dozens of die inserts, which are smaller units made of tool steel. Each die insert has at least one internal cooling water line to allow its temperature being controlled properly. Very often, each cooling line is operated with maximum flow rate running through it. The conventional approach to control die
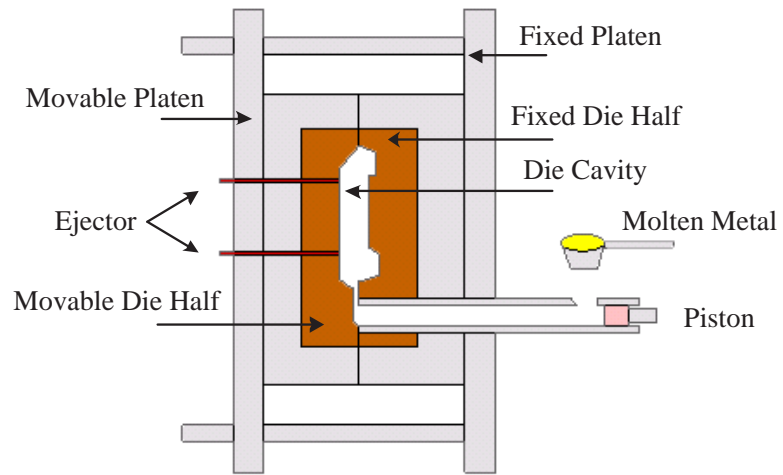
Figure 1.1: Structure of a typical casting die for high pressure die casting manufacturing processes.
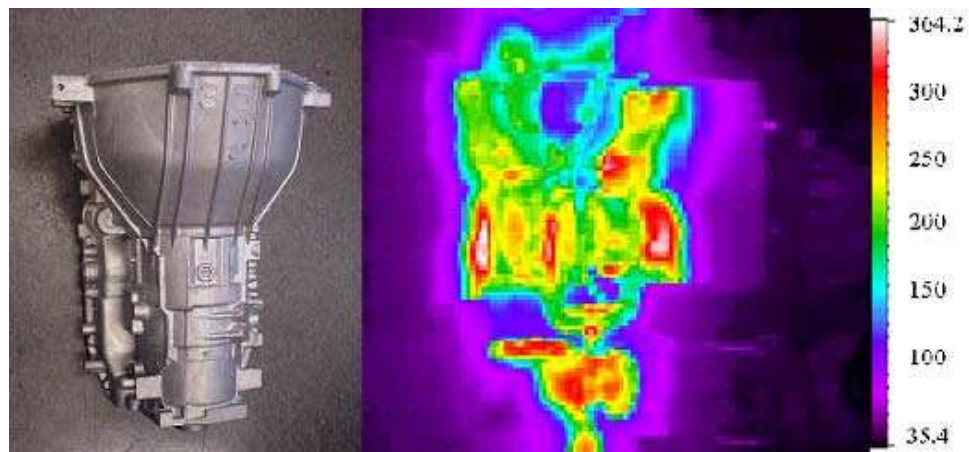
Figure 1.2: Visual image and its thermal counterpart (in ^oC) of a casting (color online, photo courtesy of Ryobi Die Casting (USA) Inc., Shelbyville IN, USA).

temperature is based on the operators' experience and trial-and-error. However, the temperature distribution on a die surface is not homogeneous when controlled by traditional method as illustrated in Figure 1.2, where the picture on right was taken by an infrared camera immediately after a casting part is ejected form a die which produces transmission cases shown by the left picture. The temperature distribution varies significantly from 200^oC to 400^oC . It is implied that those areas with relatively high temperatures are less efficient at removing heat from the molten metal.

The improper distribution of die temperatures may cause many casting defects. On the one hand, localized over-cooling which leads to the formation of defects such as poor fill can be manually adjusted by decreasing water flow rate in a specific cooling line. On the other hand, casting defects such as porosity and hot tearing, which result from hot spots with abnormal high temperatures present in the die, become difficult to alleviate due to the fact that the established cooling lines are already running at their maximum flow rates.

Owing to the increasing costs of raw materials, workmanship, energy, and the growing competition, die casting manufacturers are motivated to fabricate products with higher quality but lower cost, with greater quantity but smaller scrap rates. One of the objectives of current research is to study the possibility of designing a vision-based intelligent real-time monitoring and control system capable of intelligently and continuously managing the water flow rates of cooling lines in a die, which makes its desired thermal pattern achievable.

1.3 Literature Survey on Casting Control

Since the literatures related to the topic of machine vision and vision guided control are immense, the majority of the articles in this area will be reviewed in each chapter thereinafter. In this section, only the literature survey on casting control is covered.

In the past, various efforts have been made to develop thermal management systems and a number of commercial temperature control units were designed to help control the die temperature. Some major results are discussed as follows:

On-off Control [5]: Solenoid valves are employed as control actuators to vary the flow rate in cooling water lines, while die temperatures are used as control feedback. Specifically, the valve is fully opened to charge cooling water into a die when die surface temperature reaches a set point, and vice versa. It is obvious that the die temperature tends to oscillate around the set point continuously by this control scheme so that it cannot achieve precise results.

Proportional Control [6, 7]: To overcome the oscillation problem associated with the on-off control, the proportional control was proposed by varying the casting cycle time based on the die surface temperature. It alters the on-off ratio of solenoid valves to control the flow rate of cooling waterlines. The ratio is fixed at 1:1 at a specific temperature set point. Once die temperature is beyond the set point, solenoid valves become fully opened to allow excessive amount of water running through the cooling lines, and vice versa. It can be expected that this approach has a very slow response time and may significantly reduce the productivity.

Proportional-Integral-Differential (PID) Control [8]: Although over 60 years have been past since the first introduction of PID control, the first controller for die thermal management appeared in 1999. This control scheme not only improves the response

time but also enhances the control precision. However, due to the fact that the die temperature distribution depends on various die design and process variables for which first principles models are very difficult to be obtained, the three control parameters, proportional, integral and derivative terms, must be tuned individually for particular system through trial-and-error.

Fuzzy PID Control [9]: A fuzzy PID controller is designed to minimize the temperature differences between channels. Although the control system is capable of adjusting the desired supply of cooling water into multiple cooling lines, it is based on the so-called point measurement method, and can only solve a localized problem.

Local Temperature Controller [10]: In most recent advancement, a local controller has been designed to confine the temperature fluctuation of a die insert into a given range. However, the inhomogeneity of die temperature distribution can not be minimized globally through this approach.

In all of the work mentioned above, only thermocouples are employed as temperature sensor. To measure the die insert temperature through thermocouples, holes need to be drilled from the rear of the die insert. There are many disadvantages for using the thermocouple. First, although thermocouple is rugged and inexpensive, the cost of placement is very high. Temperature measurement is sensitive to the thermocouple's location. A small deviation from the desired location because of workmanship can cause a big error in output. Second, it is a kind of sluggish device that needs time to response to a transient process, such as temperature drops in this study. Last but not the least, drilling a hole may upset the maintenance of the die insert, and consequently may reduce its service life.

In [11, 12], a thermal camera is employed to take photos of casting dies to deter-

mine the hot/cold spots in an effort of re-designing the layout of cooling waterlines to improve cooling water flow rate and reduce casting defects. However, due to high cost, the process is not automated.

So far no work has been found that establishes a vison-based thermal control system to address the problem of die thermal management. The existing system lacks the capability of continuously and intelligently controlling the water flow rates in multiple cooling lines in accordance with the fluctuation of global die temperatures, and consequently are not able to correct the problems which are currently present in most dies used in the industry.

1.4   Dissertation Outline

The dissertaion is organized as follows: after the Introduction, Chapter 2 provides hardware and software structures of a vison-based thermal management system. In Chapter 3, the emissivity measurement of casting dies is presented under different conditions. The proposed robust curve fitting technique is covered in Chapter 4. Reconstruction of three dimensional thermal image is studies in Chapter 5. Robust temperature measurement against network packet loss is presented in Chapter 6. A simple fuzzy PID control system is implemented in Chapter 7 for multiple die inserts. Finally, the conclusions and suggestions for future work can be found in Chapter 8.

The main contributions are in Chapter 4 and 6.

Chapter 2

Vision-based Thermal Control System

This chapter presents the hardware and software structures of a vision-based thermal control system that has been built for experiments. The key sensing components of the system are two visual cameras and one infrared/thermal camera that enable the system to acquire thermal information from the three dimensional (3D) geometry of an object. A laboratory die casting simulator is also introduced in an effort of testing the performance of the system.

2.1   System Overview

Digital image is formed by mapping the 3D structure of the viewed scene to a 2-Dimensional (2D) array of numbers, which can be interpreted as a transformation of the state of the world into a set of lower dimensionality. It is obvious that the mapping is a many-to-one process. In order to recover 3D geometric information of an object from 2D images, three configurations are widely used in practice:

- Eye-on-hand: A camera is attached to a moving mechanism such as robotic

manipulator. Digital images are taken when camera is moving around the scene, and the 3D structure is re-constructed from multiple redundant images. In this configuration, only one camera is needed, but it does not have real-time performance since camera has to be moved around in order to acquire enough images. Therefore, it is not suitable for this application.

- Active 3D vision: A camera is combined with a dedicated light source, such as laser line projector. The 3D structure of an object is inferred from the shape distortion that the line exhibits when it contacts an object in view of the camera. The full structure of an object can be obtained only when the projector finishes the scanning process of the object. Therefore, real-time performance can not be achieved for an object with large and complex area.

- Passive 3D vision: Two cameras are grouped together to form the so-called stereo pair just like human being's left and right eyes. The 3D structure and distance of a scene can be inferred from two images taken from different viewpoints. Despite that this configuration needs complicated algorithms for 3D reconstruction, it has the best real time performance and therefore will be adopted in this study.

Since a stereo vision pair can only determine the geometric information of an object, additional infrared/thermal camera is a must to measure the surface temperature of the object. Therefore, three cameras are needed for the vision based thermal control system. The schematic diagram of the system is shown in Figure 2.1. In this system, personal computer (PC) with a data acquisition board is the command center. The system monitors the temperature signals that are measured by the cameras,
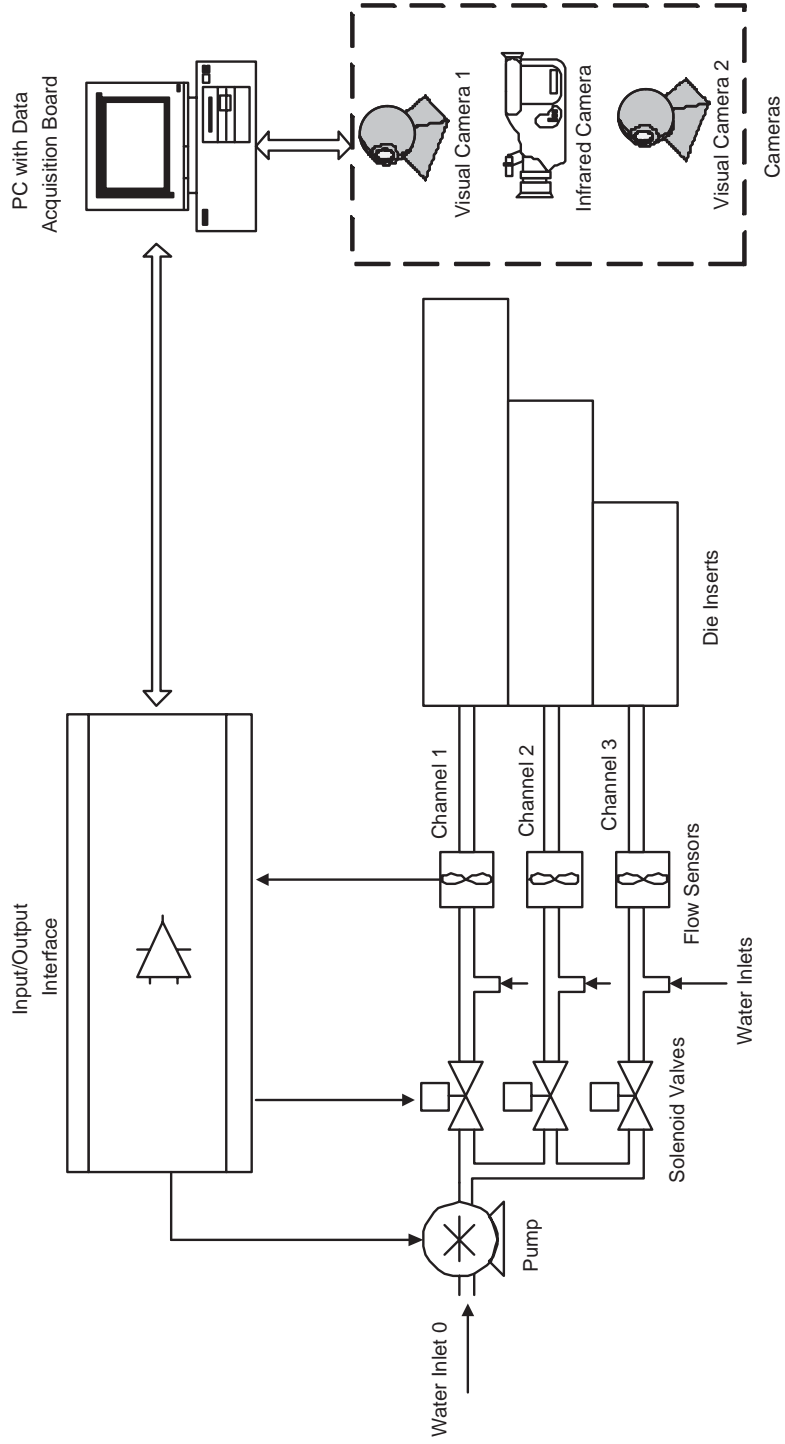
Figure 2.1: System overview: the key sensing components are two visual cameras and one infrared/thermal camera that enable the system to acquire 3D thermal information of a casting die.

Infrared Camera   Visual Camera 1   Visual Camera 2

| Thermal Image | | Visual Image 1 | | Visual Image 2 |

| 2D Thermal Image | | 3D Geometric Structure |

| 3D Thermal Image |
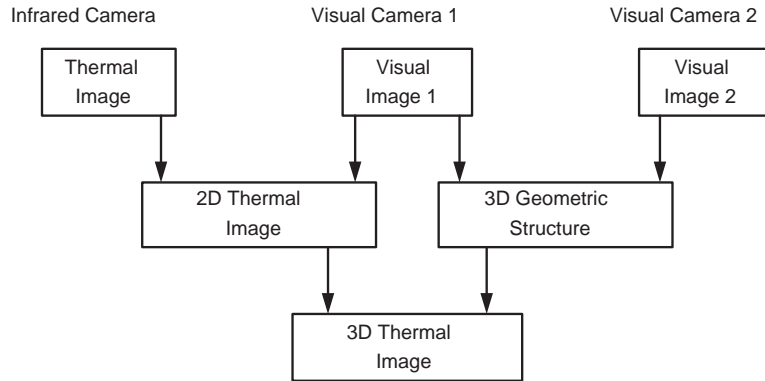
Figure 2.2: Formation of the 3D thermal image.

and flow rate signals that are measured through the flow sensors. To achieve the desired thermal pattern on the die surface, pump and solenoid valve can be actuated through the interface board to continuously adjust the flow rate of the cooling water.

It should be noted that the three cameras are the key sensing components of the thermal control system. The path to form the 3D thermal image can be shown in Figure 2.2. The temperature measurement procedures can be summarized as follows:

1. Acquire three digital pictures from three cameras simultaneously;

2. Fuse thermal image and visual image 1, which comes from visual camera 1, to form a 2D thermal image;

3. Reconstruct 3D geometry of the object from visual image 1 and 2;

4. Compute the 3D thermal image from the 2D thermal and 3D geometric image using visual image 1 as a medium.

While image fusion in Step 2 will be discussed in Chapter 4, and structure reconstruction involved in Step 3 and 4 will be addressed in Chapter 5.
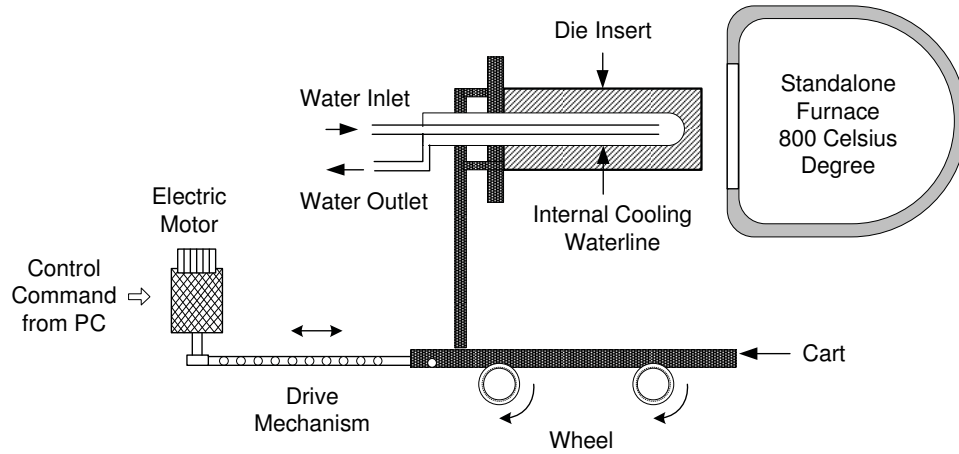
Figure 2.3: Die casting process simulator.

2.2 Die Casting Process Simulator

Numerous experiments need to be carried out in order to design and implement the vision-based thermal control system for die casting processes involving cooling of a die with multiple channels. Since it would be very costly to conduct experiments directly on a real die casting machine, a die casting process simulator has been built in laboratory. The simulator is employed to preheat the die insert to certain temperature, then cooling water is applied to cool down the insert.

The schematic diagram of the die casting process simulator is shown in Figure 2.3. Instead of heating the die by directly pouring molten metal onto it, a 3kW furnace is employed to preheat the die inserts. The inserts are mounted to a movable supporting cart and can be pushed into the furnace by an electric motor until it is completely enclosed by the furnace. An insulating plate, made of fiberglass, is placed between the contact surface of the insert and the metal rack. The die insert is preheated in the furnace to a certain temperature, then cooling water is applied to chill the insert.

14

One complete experimental cycle, which simulates the real casting process can be summarized as follows:

1. Preheat the die inserts in the furnace for 30 minutes;

2. Computer sends a command to the electric motor to pull the die inserts out of the furnace;

3. Apply cooling water to the inserts for 20 seconds;

4. Computer sends another command to the motor to push the inserts into the furnace. The system is ready for the next cycle.

The experimental cycle repeats itself automatically. The insert cooling stage is used to simulate the solidification stage of a real die casting process. It should be mentioned that it is the cooling stage of the die inserts, other than the heating period, that was used to simulate the solidification stage of a real die casting process [3, 10], since the die temperature is not constant in practice, high during mold filling and low when the castings are being ejected.

The schematic diagram of the die inserts used in the experiment are shown in Figure 2.4. Each insert is made of H13 tool steel and contains one cooling waterline. To create a temperature field for control purpose, the three inserts are designed with three different lengths to generate different thermal behavior under the same cooling pattern.
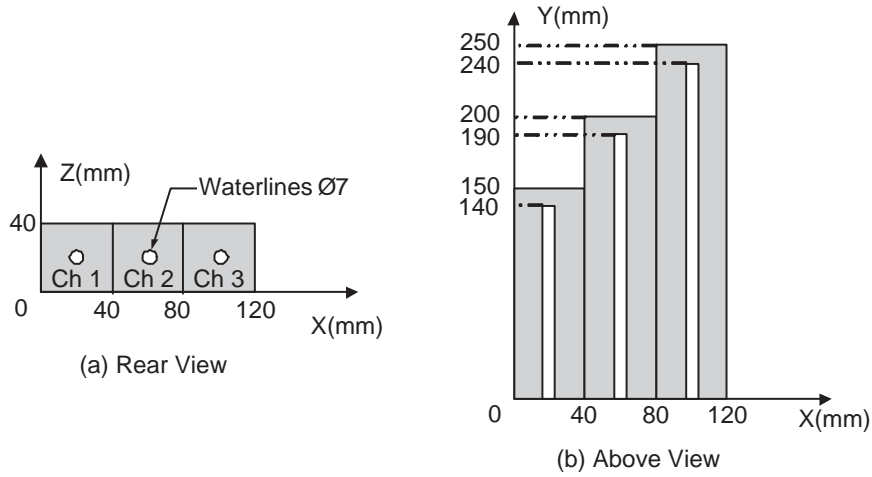
Figure 2.4: Die inserts.

2.3 Selection and Design of Hardware

A computerized vision-based thermal control system (VTCS) has been designed and implemented in this study. The schematic diagram of the hardware structure is illustrated in Figure 2.5, where a personal computer (PC) with a data acquisition board serves as a command center. In the present study, the VTCS is required to measure 2 types of analogue signals and output 2 kinds of digital signals. The inputs to be measured are: 1) temperature signals along with geometric locations from cameras; 2) flow rate signals from flow sensors. The main function of digital outputs is to control pump speed and solenoid valves. The workflow of the system can be summarized as follows:

1. Visual and thermal pictures are taken by the system through cameras to generate 2D/3D thermograph of the die inserts;

2. After the thermal pattern being processed, the size and location of the hot spots

16
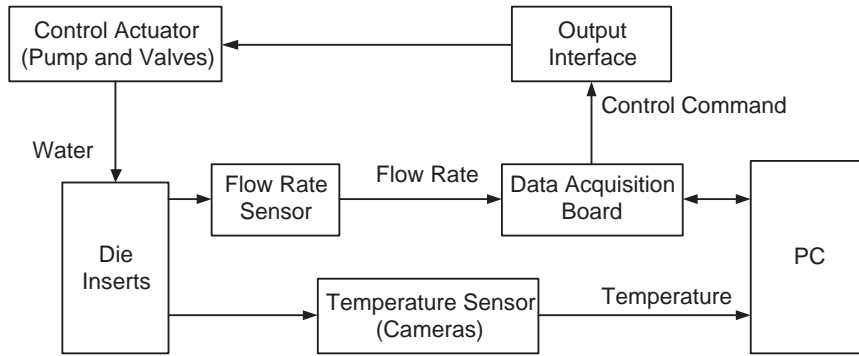
Figure 2.5: Hardware structure and information flow.

or cold spots on the die surface is computed;

3. Control algorithm of the system sends out control command to pump and valves to adjust the flow rate of cooling channels such that the temperature of the hot spots decreases more rapidly and the temperature of the cold spots decreases more slowly than those of their surrounding areas. Through this approach, the homogenous temperature distribution on the die surface may become achievable.

The desired measurement range for the temperature signal is from 0^oC to 500^oC with accuracy $\pm 10^oC$, which covers the window of die temperature variation in the real die casting process [2]. For the water flow rate signal, the desired measurement range is selected in a range from 2.08 L/min (0.55 GPM) to 9.46 L/min (2.5 GPM) with a resolution of 0.0379 L/min (0.01 GPM). The main parts contained in the VTCS are listed thereinafter.

Figure 2.6: PC hosted data acquisition board.

2.3.1 PC Hosted Data Acquisition Board

There are two main functions of a PC hosted data acquisition board used in this system: to convert analogue signals such as flow rate to their digital counterparts that can be read by PC, and to transmit control commands to actuators such as pump and valves. The Cyberresearch® 330k Hz 12-bit board with 8-channel differential inputs or 16-channel single-ended inputs, part number PCI-DAS 1602/12 as shown in Fugure 2.6, is selected due to its functionality and relatively low cost. The smallest voltage that can be detected by this board with an input range from 0 to 10 V can be calculated as:

$$\Delta U = \frac{10V}{2^{12}} = 2.44mV$$

2.3.2 Visual and Thermal Cameras

Infrared sensors are non-contacting devices that infer temperature by measuring the thermal radiation emitted by a material. It can measure the temperature of a large area instead of one spot at one time performed by a thermocouple. In this project, a two-dimensional real thermograph can be directly determined by an infrared camera

18

(a) Visual Camera   (b) Thermal Camera

Figure 2.7: (a)Visual and (b) thermal camera for temperature measurement.
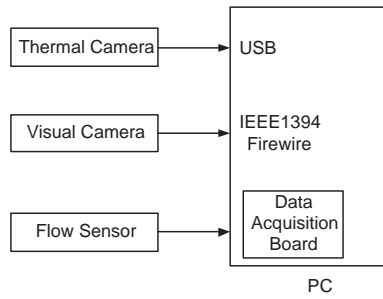
Figure 2.8: The usage of computer ports for external communications.

system with high accuracy and fast response time.

The infrared camera used in this study is called MIDAS thermal imager from Mikron Infrared Inc (Figure 2.7). Its resolution is 320×240 pixels; spectral band is from 8.0 to 14.0 μm; temperature range is from 0 to $500^{o}C$; and measurement accuracy is $\pm 2K$ or $\pm 2\%$ reading. It communicate with the PC via USB port. The visual camera used in this study is Prosilica® EC1350 imager with maximum resolution 1360×1024 pixels. It has IEEE1394 fireware port that can communicate directly with a PC. The usage of the computer ports is shown in Figure 2.8. Two visual cameras and one thermal camera are configured to a resolution of 320×240 pixels with maximum image update rate 30 fps (frame per second).

19

(a) Pump   (b) Solenoid valve

Figure 2.9: Control actuators: (a) pump and (b) solenoid valve.

2.3.3   Pump and Solenoid Valve

An electrical-pulse-controlled, air-operated, double-diaphragm pump (Figure 2.9(a)) made by Wilden®is chosen as control actuator. Through altering the pulse frequency, the pump speed, which is denoted as stroke per minute (SPM), is changed accordingly to vary water flow rates. The pump is capable of increasing water flow rate up to 9.46 liter/minute (L/min) or 2.5 gallon/minute (GPM).

Solenoid valves, model number SV-301 from OMEGA, are employed to open or shut down extra cooling waterlines (Figure 2.9(b)).

2.3.4   Water Flow Rate Sensor

The cooling water flow rates in die insert are measured by the RotoFlow®flow sensors in Figure 2.10 manufactured by GEMS Sensors Inc. The output range of the sensor is from 0 to 10V DC proportional to the flow rate from 2.08 L/min (0.55GPM) to 18.9 L/min (5 GPM) as shown in Figure 2.11. This signal can be read directly by the data acquisition board without signal amplifier. The minimum detectable flow rate

Figure 2.10: Flow sensor.
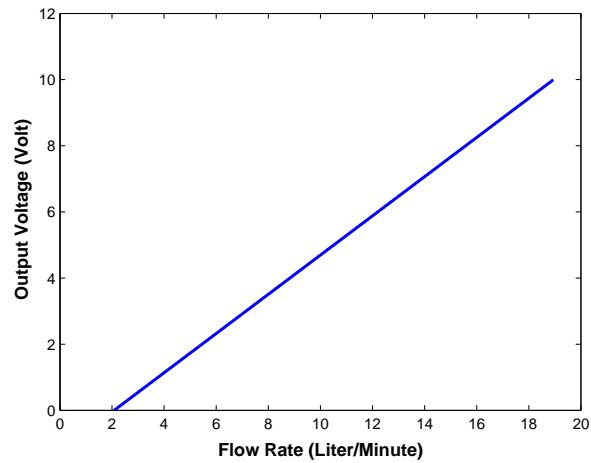
Figure 2.11: Output characteristics of the flow sensor.

can be calculated as

$$\Delta F = \frac{18.9 L/min}{10 \times 10^3 mV} \times 2.44 mV = 0.0046 L/min$$

2.3.5   Input/Output Interface Box

All the flow rate signals and control signals are connected to or from the data acquisi-
tion board through the interface box (Figure 2.12). There are four main parts inside
the box: (1) adaptor board converts the 100-pin port of the data acquisition board

21
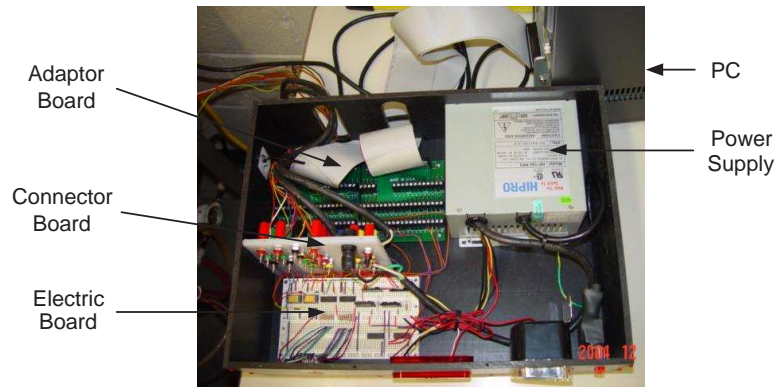
Figure 2.12: Input/output interface box.

through a ribbon cable to a 100-connector mount for easy wiring; (2) connector board contains several wiring terminals that all sensor and actuator wires go through them; (3) chips and other electric parts are installed on the electric board; and (4) power supply provides +5VDC, +12VDC power sources that the system needs.

Digital output pins on the data acquisition board are used as control outputs. Solid-state relays are engaged to isolate the data acquisition board from the electrical circuits of the pump, solenoid valves, warning light and alarm. The typical operating current of solid-state relay in this study is about 20 mA, despite that the maximum digital output current of the data acquisition board is only 2.5 mA, hence the inverter chips (7406) are occupied to provide sufficient current sink to drive the solid-state relay. The schematic diagram of the electric circuits in the interface box is shown in Figure 2.13.
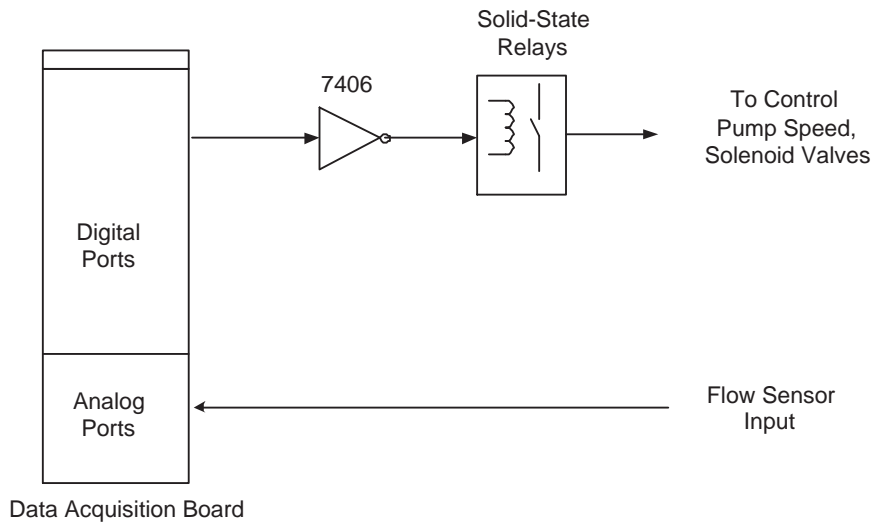
Figure 2.13: Schematic diagram of the electric circuit in the interface box.

2.4 Software Design

The software program running on a PC is designed to acquire, monitor, and process data in real-time, and then to send control command according to the temperature fluctuation of the die inserts, all through interfacing to the plug-in data acquisition board housed in the PC. The graphic user interface (GUI) is mainly responsible for displaying real-time digital images of the die inserts and flow rate curves for each cooling channel.

The main program routine consists of four sub-function modules (Figure 2.14): data sampling, data display, data saving, and control. The data-sampling module is responsible for acquiring images from cameras and flow rate data from flow sensors at a sampling rate that can be specified by users. The data-displaying module displays images and other data on the screen in the format of curves and values. The data-saving module saves images in JPEG format, and temperature and flow rate data in
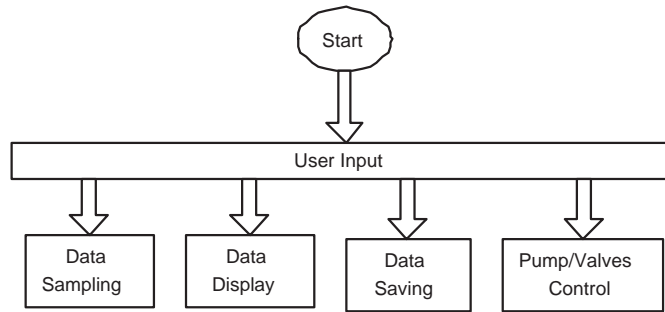
Figure 2.14: Software subroutines.

an ASCII text file format to the hard disk for further analysis. The control module can actuate solenoid valves and adjust pump speed manually or automatically based on its built-in control algorithms.

2.5 Summary

The hardware and software structures of the vision-based thermal control system have been introduced. The experiment carried out in next chapters will be based on these structures.

Chapter 3

Emissivity Determination

Different influential factor on the emissivity of a die surface is examined. Experiments are carried out to determine the emissivity of a die surface both qualitatively and quantitatively.

3.1   Introduction

Infrared camera has been employed to measure the temperature of a die surface [11]. Although emissivity, as a crucial parameter for temperature measurement, should be determined case by case, no paper or book can be found as a reference for the effect of different influential factor on the emissivity of a die surface. In this chapter this problem will be examined both qualitatively and quantitatively.

Infrared ray, like radio waves, is part of electromagnetic spectrum in which the major difference between each spectral band is in their wavelength. The wavelength of the infrared radiation, which lies roughly from 0.70 to $1000 \mu m$, is longer than that of visible light yet shorter than that of microwaves (Figure 3.1).

All materials above 0 degrees Kelvin emit infrared energy except black body, which
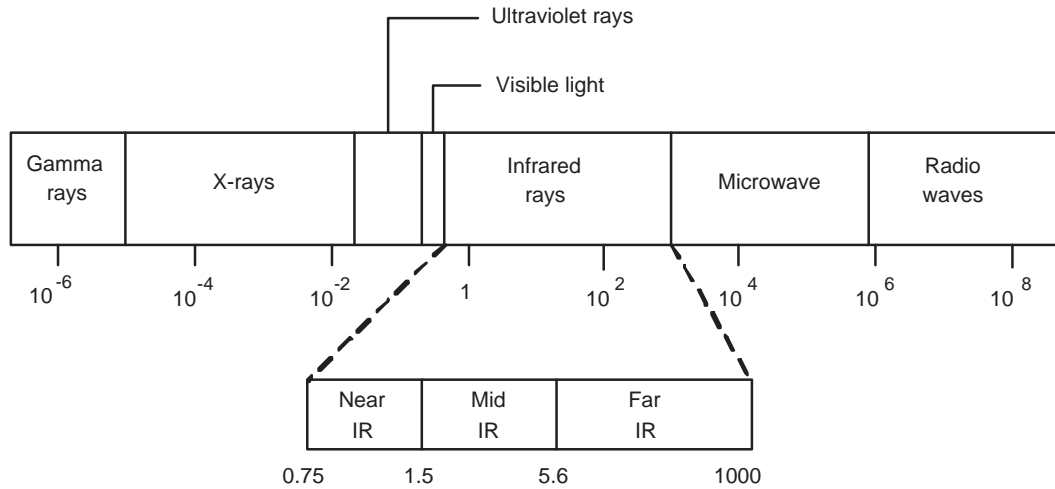
Figure 3.1: Wavelengths of electromagnetic spectrum (in μm).

is a theoretical surface that absorbs all incident radiation from all directions and at all wavelengths. The intensity of the emittance has a positive relationship with the temperature of the material. In other words, the higher the temperature, the greater the intensity of infrared energy that is emitted. Therefore, the temperature of an object can be inferred by measuring the infrared energy it emits. The energy sensor, which is made of semiconductor and is also called microbolometer, changes its resistance when infrared rays are incident onto it. The resistance is then converted into an electrical signal such as voltage to indicate the amplitude of the sensed energy or temperature. The planar detector of the infrared camera usually contains thousands of the microbolometers, which defines the resolution of the camera. The output voltages of the detector are usually transferred into an intensity image for better visual effect.
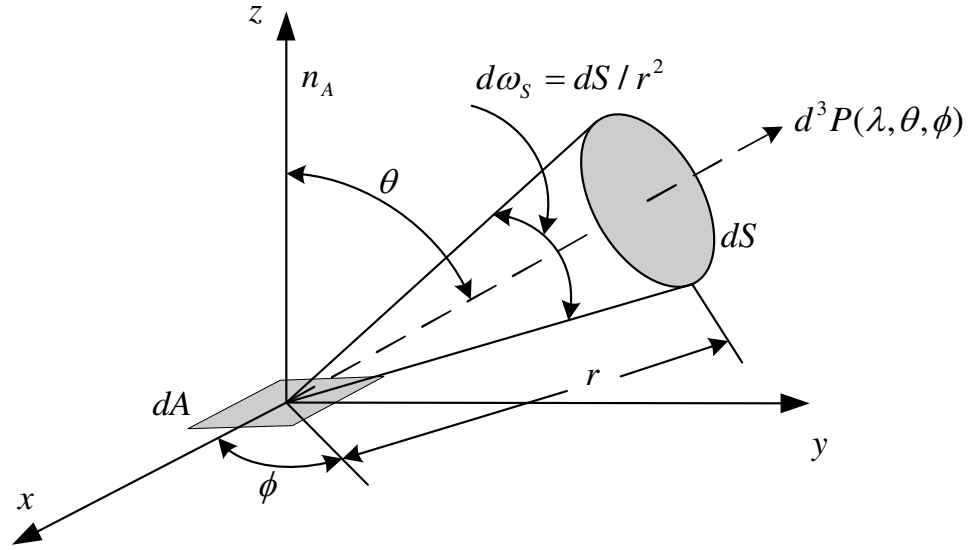
Figure 3.2: Spectral intensity.

3.2 Influential Factors on Emissivity

The spectral intensity of a plane source is defined as the power per unit wavelength in wavelength interval $d\lambda$ centered at a specific wavelength λ, per unit projected area of the source, per unit solid angle, passing in a given direction θ and ϕ. As shown in Figure 3.2, the spectral intensity can be written as

$$i_\lambda(\lambda, \theta, \phi) = \frac{d^3 P(\lambda, \theta, \phi)}{dA cos\theta d\omega_S d\lambda} \quad (W/m^2 \cdot sr \cdot \mu m)$$

where $d^3 P(\lambda, \theta, \phi)$ is the power (W) leaving the element of the source plane surface dA (m^2) in direction θ and ϕ; dS is the element of the projected area; $d\omega_s$ (sr) is the solid angle; and n_A is the normal to dA.

As well as emitting infrared energy, materials also reflect, absorb and transmit infrared energy. According to the theory of conservation of energy, the extent to which materials reflect, absorb and transmit infrared energy is known as the emissivity of

27

the material.

The directional spectral emissivity $\varepsilon_\lambda(\lambda, T, \theta, \phi)$ is defined as the ratio of the spectral intensity emitted by a body in direction θ and ϕ to the intensity that would be emitted by a blackbody at the same temperature and wavelength.

$$\epsilon_\lambda(\lambda, T, \theta, \phi) = \frac{i_{\lambda,o}(\lambda, T, \theta, \phi)}{i_{\lambda,b}(\lambda, T)}$$

where $i_{\lambda,o}(\lambda, T, \theta, \phi)$ and $i_{\lambda,b}(\lambda, T)$ are the spectral intensity of the object and a blackbody at the same temperature T respectively.

The emissivity is a dimensionless quantity. For a blackboy, it equals to 1. It is clear that the emissivity of an object is dependent on the specific wavelength, temperature and gazing direction θ and ϕ. The total directional total emissivity can be calculated by:

$$\begin{aligned}
\epsilon(T, \theta, \phi) &= \frac{\int_{\lambda=0}^{\infty} \epsilon_\lambda(\lambda, T, \theta, \phi) i_{\lambda,b}(\lambda, T) d\lambda}{\int_{\lambda=0}^{\infty} i_{\lambda,b}(\lambda, T) d\lambda} & (3.1) \\
&= \frac{\pi}{\sigma T^4} \int_{\lambda=0}^{\infty} \epsilon_\lambda(\lambda, T, \theta, \phi) i_{\lambda,b}(\lambda, T) d\lambda & (3.2)
\end{aligned}$$

In the last step, the Stefan-Bolzmann's Law is used. It states that the directional total emissive power for a blackbody is given by

$$e_b = \pi \int_{\lambda=0}^{\infty} i_{\lambda,b}(\lambda, T) d\lambda = \sigma T^4 \quad (W/m^2)$$

As a real object never behaves as an ideal blackbody, the emissivity depends on factors such as temperature, emission angle, and wavelength. However, it is typical in engineering to assume that the spectral emissivity of an object does not depend on wavelength and emission angle, which leads to the diffuse and grey body assumption. A surface is said to be grey in a given direction if its directional spectral emissivity

28
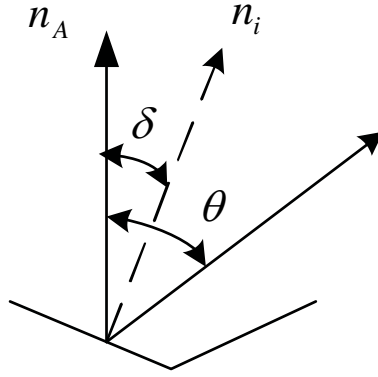
Figure 3.3: A model for rough surface.

is independent of wavelength; and is said to be diffuse at a given wavelength if its directional spectral emissivity is independent of direction. For a diffuse gray body, its emissivity is given as

$$\epsilon_\lambda = \epsilon_\lambda(T)$$

That is to say that by assumption, the emissivity is only a function of the temperature. The assumption will lead to measurement error, and it can be corrected by thorough experiments or advanced approach, such as Monto-carlo ray-trace method.

The die surface may become rough after extensively usage when compared to a new one. The emissivity could be greatly affected by the roughness of the die surface. Figure 3.3 illustrates a model for rough surface constituted of facets with inclination angle δ to the normal with a Gaussian distribution [19]:

$$f(\delta) = exp(-q) \cdot tan^2\delta$$

where q is a parameter measuring the degree of roughness inversely. The directional total emissivity in a given direction θ can be written as [19]:

$$\epsilon = \epsilon_e + \epsilon_r$$

29

where ϵ_e is the emissivity corresponding to the intensity directly emitted and received from the surface, and ϵ_r is the emissivity corresponding to the intensity emitted by one facet and received after reflection on another facet. It follows that

$$\epsilon_e = \frac{1}{cos\theta} \int_{-\pi/2+\theta}^{\pi/2-\theta} \epsilon(\delta - \theta) \frac{cos(\delta - \theta) f(\delta)}{cos\delta} d\delta + 2 \int_{\pi/2-\theta}^{\pi/2} \epsilon(\delta - \theta) f(\delta) d\delta$$

And for a relatively small angle [19],

$$
\begin{aligned}
\epsilon_r = \ & \frac{1}{cos\theta} \int_{-\pi/4+\theta/2}^{-\pi/6+\theta/3} (1 - \epsilon(\delta - \theta)) \epsilon(\pi - 3|\delta| - \theta) \frac{cos(3\delta - \theta) f(\delta)}{cos\delta} d\delta \\
& + \frac{1}{cos\theta} \int_{\pi/6+\theta/3}^{\pi/4+\theta/2} (1 - \epsilon(\delta - \theta)) \epsilon(\pi - 3\delta + \theta) \frac{cos(3\delta - \theta) f(\delta)}{cos\delta} d\delta \\
& + \frac{1}{cos\theta} \int_{-\pi/2+\theta}^{-\pi/4+\theta/2} (1 - \epsilon(\delta - \theta)) \epsilon(\pi - 3|\delta| - \theta) \frac{cos(\delta - \theta) f(\delta)}{cos\delta} d\delta \\
& + \frac{1}{cos\theta} \int_{\pi/4+\theta/2}^{\pi/2-\theta} (1 - \epsilon(\delta - \theta)) \epsilon(\pi - 3\delta + \theta) \frac{cos(\delta - \theta) f(\delta)}{cos\delta} d\delta \\
& + 2 \int_{\pi/2-\theta}^{\pi/2} (1 - \epsilon(\delta - \theta)) \epsilon(\pi - 3\delta + \theta) f(\delta) d\delta
\end{aligned}
$$

It is clear that, for the same material, the emissivity is also a function of the roughness of the surface.

3.3 Measurement Methodology

While standardized emissivity values for most materials are available, emissivity for the same material is different under different condition such as surface roughness. Therefore, the standard emissivity table can only be used as a reference. For accurate temperature measurement, emissivity has to be determined case by case. Basically there are two method to determine the emissivity: direct and indirect. For direct

method, a calorimetric or radiometric technique is used with a blackbody as a reference [28, 29, 30]. While the indirect method uses the Kirckhoff's law by measuring the reflectivity first and then deducing the emissivity from it [31]. The emissivity can also be determined through an infrared camera as it often contains an internal function [32, 33].

Generally speaking, if an infrared camera is available, there are three ways to determine the emissivity of the material, to ensure accurate temperature measurements:

1. Heat the die insert to a known temperature and measure the temperature of the die surface using the infrared camera. Then adjust the emissivity value to force the image to display the known temperature;

2. Attach a piece of masking tape with known emissivity to the insert surface, or scorch a small area of the die surface with soot, or coat with a dull black paint. Measure the temperature of the tape/soot first and use it as a reference, then adjust the emissivity value to force the temperature of the other areas display the reference temperature.

3. Drill a hole into the object with depth at least 6 times the diameter. This hole acts as a blackbody with emissivity of 1.0 [28, 29, 30]. Measure the temperature in the hole first as a reference, then adjust the emissivity value to force the temperature of the other areas display the reference temperature.

The third method will be adopted in this study due to accuracy. A die insert, which is made of the same material with the same surface condition, is used as a sample to determined the emissivity. The schematic diagram of the cylindric insert is shown in Figure 3.4. A small hole is drilled through the back with the length to radius ratio
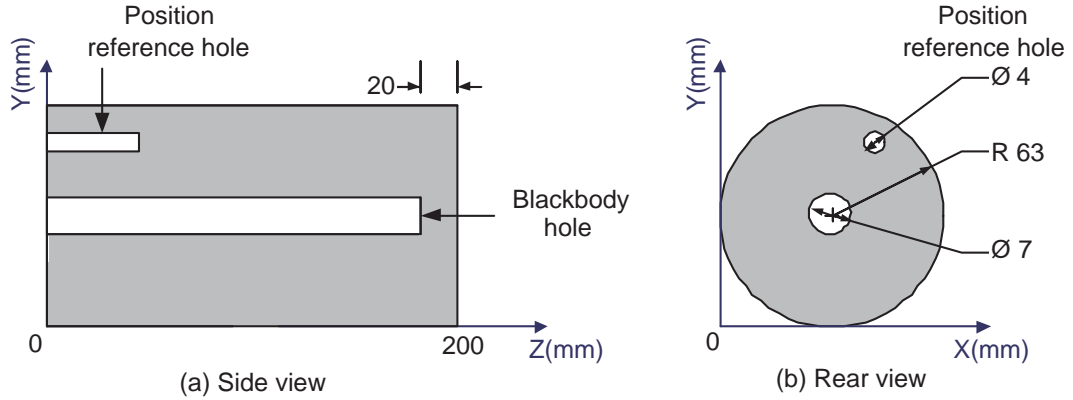
Figure 3.4: A die insert as a blackbody-type source for emissivity calibration.

given by $L/r = 180/7 = 25.7 \gg 7$. Thus the radiation leaving this hole should closely approximate that of a blackbody. The system setup for the emissivity determination is illustrated in Figure 3.5. The insert is heated and kept in the furnace at a constant temperature, and its temperature is uniformly distributed as there is only a relatively small window open for the infrared camera to acquire images.

According to Planck's Law, the blackbody radiation emitted per unit area as a function of wavelength is given by:

$$i_{\lambda,b}(\lambda, T) = \frac{C_1}{\lambda^5 (exp(C_2/\lambda T - 1))} \tag{3.3}$$

where C_1 and C_2 are the first and second radiation constants, and λ is the wavelength. For a gray-body object, the radiation emitted per unit area can be written as

$$i_{\lambda,g}(\lambda, T_g) = \frac{\epsilon_g C_1}{\lambda^5 (exp(C_2/\lambda T_g - 1))} \tag{3.4}$$

where T_g is the actual temperature of the insert, and ϵ_g is the emissivity of the insert at the wavelength λ. The radiation measured by the infrared camera is through the equation:

$$i_{\lambda,g}(\lambda, T_g, \epsilon_g) = i_{\lambda,c}(\lambda, T_c, \epsilon_c) \tag{3.5}$$

32
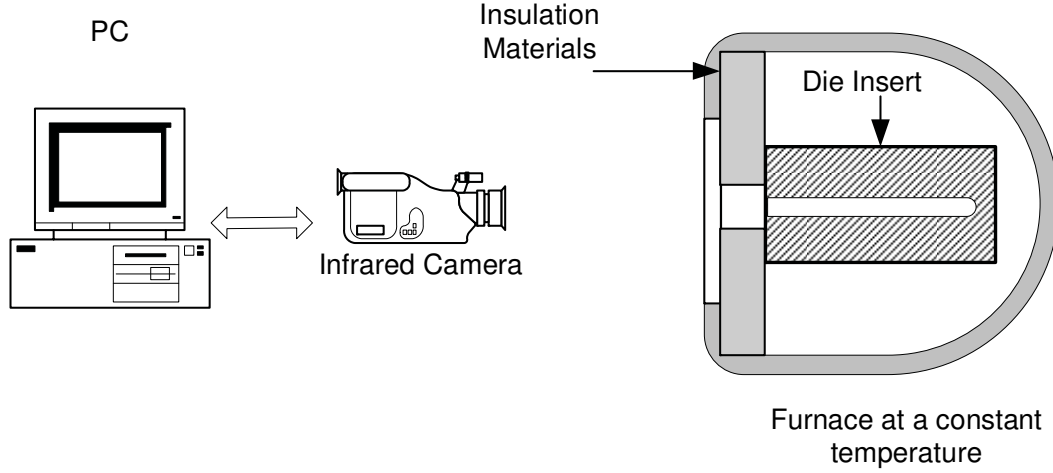
Figure 3.5: System setup for emissivity determination.

where T_c is the measured apparent temperature of the insert, and ϵ_c is the emissivity parameter that is built in and can be adjusted through the camera. From Equations (3.3)–(3.5), the real insert temperature T_g can be solved from its measured apparent temperature T_c and is given by [26]:

$$T_g = \frac{1}{\frac{1}{T_c} - \frac{\lambda}{C_2} ln \frac{\epsilon_c}{\epsilon_g}} \tag{3.6}$$

It is obvious that $T_g = T_C$ if and only if $\epsilon_c = \epsilon_g$. The real temperature and emissivity can be obtained from the above equation.

3.4 Experimental Results

It is clear from above analysis that the emissivity of a die surface is dependent on its temperature, gazing angle and surface condition. Therefore, three experiments are designed and carried out to investigate : 1) the effect of die temperature; 2) the effect of measuring angle θ; and 3) the effect of roughness on the emissivity of the

33

die surface. The emissivity mentioned thereinafter is the directional total emissivity otherwise specified.

Experiment Procedures 3.1. *The general experiment procedures to determine the emissivity of the die surface can be summarized as follows:*

1. *Heat die insert in the furnace at about 500ºC for about 30 minutes; turn off the furnace and wait for 30 minutes to let the insert temperature become more uniformly distributed;*

2. *Set the emissivity parameter of the camera to 1, and measure the temperature of the hole and die surface via infrared camera. Use the hole temperature as the reference temperature;*

3. *Adjust the emissivity parameter of the camera according to Equation 3.6 such that the apparent temperature on die surface equals to the reference temperature (i.e., the hole temperature in above step as it is a black-body type source); and*

4. *Repeat the above procedure for temperature 450ºC, 400ºC, 350ºC, 300ºC, 250ºC, 200ºC, 150ºC, and 100ºC.*

3.4.1   Effect of temperature on emissivity

For the emissive angle θ at 0 in Figure 3.2, the typical thermal images of the insert surface are shown in Figure 3.6, where only two pictures at about $500^{o}C$ and $300^{o}C$ are selected for illustration only. The average temperature of area 1, where the blackbody hole locates, and the average temperature of area 2 on the insert surface are acquired and denoted as T_1 and T_2 respectively. The determined emissivity is illustrated in

34
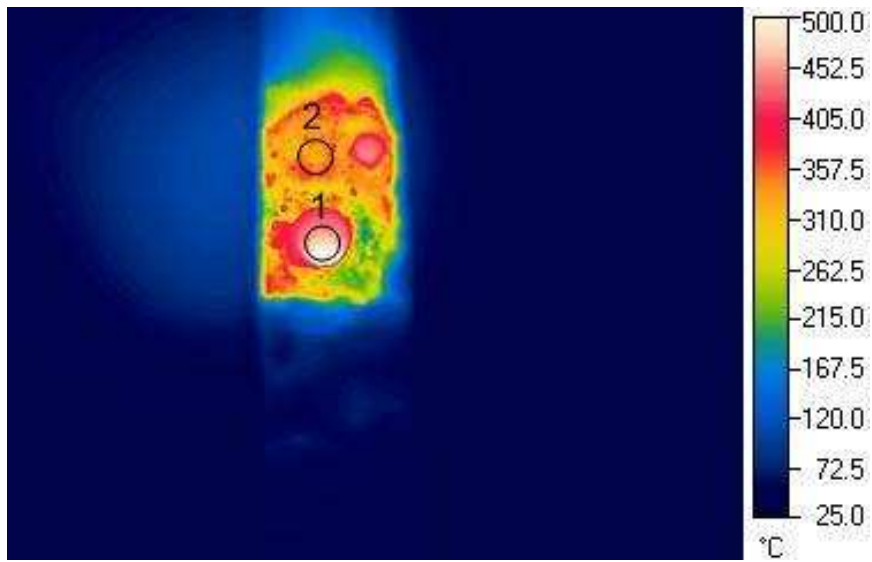
(a) Thermal image at temperature about $500^{o}C$
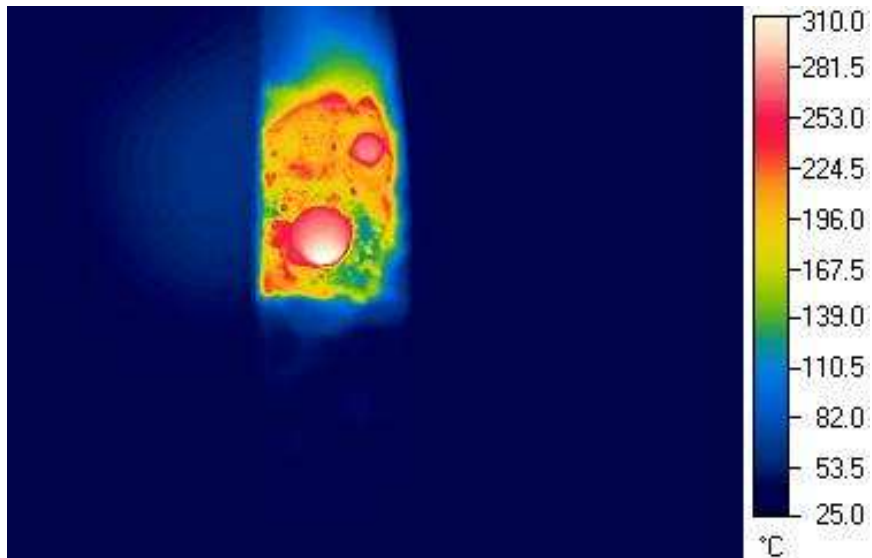
(b) Thermal image at temperature about $300^{o}C$

Figure 3.6: Thermal images for emissivity determination: (a) $500^{o}C$, (a) $300^{o}C$. (color online).

Table 3.1: Emissivity variations of an insert with different temperature settings

$T_1(^oC)$	99.6	152.9	199.8	250.2	299.9	350.1	399.4	448.7	495.5
$T_2(^oC)$	63.3	95.9	130.6	184.3	215.8	254.7	296.5	325.2	370.1
$\Delta T(^oC)$	36.3	57.0	69.2	65.9	84.1	95.4	102.9	123.5	125.4
ϵ	0.50	0.52	0.52	0.58	0.59	0.61	0.63	0.63	0.64

Table 3.1, where the temperature difference $\Delta T = T_1 - T_2$. The measured emissivity of the die surface along with T_1 is also plotted in Figure 3.7. It can be seen that the emissivity is not constant, and it increases as the temperature increases. The temperature difference ΔT also increases as the real surface temperature T_1 increases.

The relationship between the emissivity of the insert surface and the temperature T_1 and T_2 can be modeled as:

$$\epsilon = 0.00038 * T_1 + 0.46$$

with the coefficient of determination between measured and predicted values $R^2 = 0.9675$, and

$$\epsilon = 0.0005 * T_2 + 0.47$$

with the coefficient of determination between measured and predicted values $R^2 = 0.9742$. The R^2 value, which is no more than 1.0, measures how well the model fits the original data [60]. The closer to 1.0, the better. The above equations are valid when the environmental temperature is at 22.3^oC; and can be used to adjust the emissivity parameter of the camera according to its measured temperature at $\epsilon = 1$.
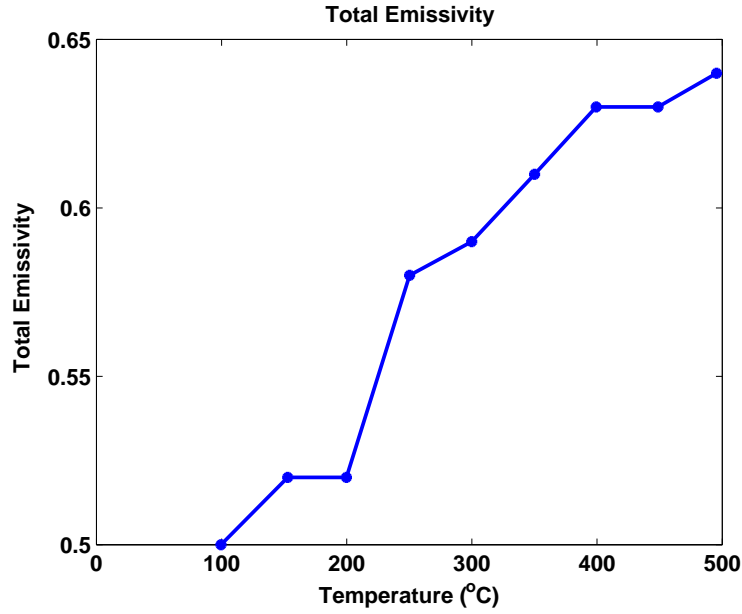
Figure 3.7: Measured emissivity of the die surface along with T_1.

3.4.2 Effect of emissive angle on emissivity

In order to determine the effect of emissive angle on the emissivity of the die surface, the zenith angle θ (the angle between the normal of the die insert surface and the image plane of the camera) is set at 15°, 30°, 45° and 60° respectively. The experiment results are shown in Table 3.2, and illustrated in Figure 3.8. It can be seen that the emissivity of the same θ increases as the temperature increases, however, the slope for different θ is different. The bigger the emissive angle, the less the slope. It also implies that the bigger the θ, the bigger the temperature difference ΔT. If the emissivity of the die surface is not properly determined, measurement error will occur and measured temperatures become unacceptable.

37

Table 3.2: Emissivity variations with different emissive angle

$T_1(^oC)$	99.6	152.9	199.8	250.2	299.9	350.1	399.4	448.7	495.5
$\epsilon(\theta = 0^o)$	0.50	0.52	0.52	0.58	0.59	0.61	0.63	0.63	0.64
$\epsilon(\theta = 15^o)$	0.49	0.51	0.50	0.55	0.55	0.57	0.60	0.61	0.61
$\epsilon(\theta = 30^o)$	0.48	0.50	0.50	0.53	0.54	0.55	0.57	0.57	0.57
$\epsilon(\theta = 45^o)$	0.46	0.47	0.48	0.50	0.51	0.51	0.52	0.53	0.53
$\epsilon(\theta = 60^o)$	0.43	0.43	0.44	0.45	0.45	0.46	0.45	0.46	0.45
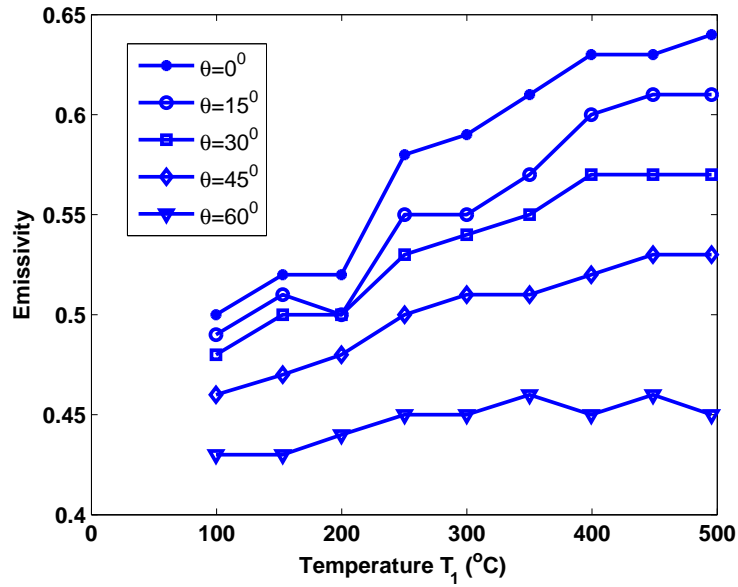
Figure 3.8: Effect of emissive angle on the measured emissivity.

(a) surface 1   (b) surface 2   (c) surface 3

Figure 3.9: Three die inserts to be measured for the effect of surface roughness on emissivity, (a) the least used, (b) moderately used, and (c) extensively used.

3.4.3 Effect of surface roughness on emissivity

A thick layer of oxide may deposit on the die surface after it has been used for a period of time, which could change the color and the roughness of the surface, and hence have greatly influence on the emissivity. To determine the effect of roughness on the emissivity, three die inserts have been used for measurement as shown in Figure 3.9, where surface 1, 2 and 3 are selected as the least used, moderately used, and extensively used die insert respectively, and the roughnesses of these surfaces are in an increasing order. The experiment results are shown in Table 3.3, and illustrated in Figure 3.10. The blackbody temperature T_1 has been rounded up to its nearest hundredth digit as the exactly same temperature can not be obtained after changing die inserts in the furnace. It is evident that the emissivity of all surfaces increases as the temperature increases. But the increasing rates of the emissivity with temperatures for different surface conditions are different. The larger the roughness, the higher the increasing rate of the emissivity. It may also imply that a high emissivity should be used when temperature measurements are performed on extensively used die inserts.

Table 3.3: Emissivity variations with different die surface condition

$T_1(^oC)$	100	150	200	250	300	350	400	450	495
$\epsilon(1)$	0.43	0.44	0.45	0.46	0.47	0.47	0.47	0.47	0.47
$\epsilon(2)$	0.50	0.52	0.52	0.58	0.59	0.61	0.63	0.63	0.64
$\epsilon(3)$	0.65	0.66	0.67	0.72	0.73	0.74	0.76	0.76	0.77
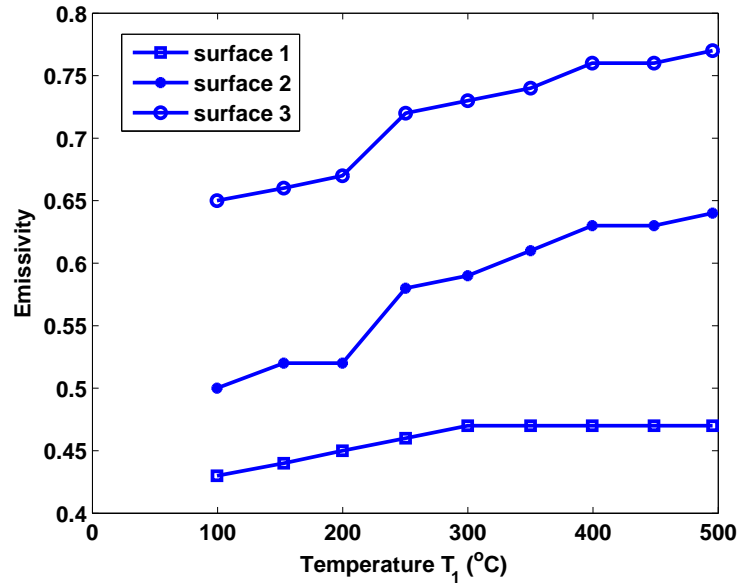
Figure 3.10: Effect of die surface conditions on the measured emissivity.

Table 3.4: Effect of Emissivity on Measured Temperature

$T_{S2}(^{o}C)$	100	150	200	250	300	350	400	450	495
$\epsilon(2)$	0.50	0.52	0.52	0.58	0.59	0.61	0.63	0.63	0.64
$T_{S1}(^{o}C)$	88.4	128.1	170.6	209.3	248.5	288.3	323.6	352.8	387.2
$T_{S3}(^{o}C)$	121.3	170.7	226.2	289.5	339.7	399.6	453.4	491.1	539.7

3.4.4 Effect of emissivity on measured temperature

As mentioned above, the emissivity is a critical parameter for temperature measurement. One experiment has been carried out to understand the effect of emissivity on the measured temperature, if the emissivity is not appropriately calibrated. The two die inserts in Figure 3.9 (a) and (c) from above experiment are used. The temperatures of the inserts are measured by the infrared camera while the emissivity value is set to be the value of the insert (b). The results are summarized in Table 3.4 and plotted in Figure 3.11, where T_{S2} represents the temperature of moderately used die Surface 2, T_{S1} is the temperature of barely used die Surface 1, and T_{S3} stands for the temperature of extensively used die Surface 3. Since the emissivity is set to that of Surface 2, T_{S2} is the true temperature of the die surface. It is clear from Figure 3.11 that the measured temperature of the Surface 3 is higher than that of its true temperature, while the measured temperature of the Surface 1 is lower. The similar phenomena can also be observed as follows: 1) if the emissivity is set to that of Surface 1, then the measured temperature of both Surface 2 and 3 is higher than that of true temperature; 2) if the emissivity is set to that of Surface 3, then the measured temperature of both Surface 1 and 2 is lower than that of true temperature.
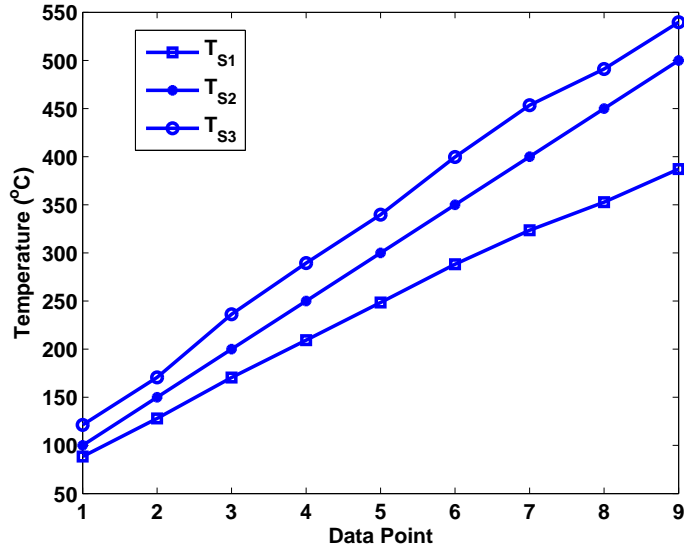
Figure 3.11: Measured emissivity of the die surface along with T_1.

3.5   Summary

The emissivity of a die insert depends on many factors such as temperature, emissive angle, and surface condition. As the die insert does not behave as a blackbody object, extra caution has to be taken when deducing the real temperature from a thermal imager. The real temperature obtained from a thermograph is very sensitive to the emissivity settings. If the emissivity has not been carefully determined, measurement error may accumulate to an unacceptable level. From above experiment, the following phenomena have been observes: 1) the emissivity of the die insert increases as the temperature climbs; 2) the emissivity decreases as the emissive angle increases; and 3) the roughness of the die insert may change as it has been used in production, and hence may also have great impact on the measured emissivity.

Chapter 4

Two–Dimensional Temperature Measurement

This chapter presents the method on how to obtain the temperature of a 2D surface from one visual image and one thermal image. Fundamental theories on digital image are introduced first. An adaptive curve fitting method is proposed for robust object localization against measurement outliers/noises. Visual image and thermal image are then fused together to retrieve the 2D temperature from a surface.

The proposed robust method is to be examined extensively. Superaccuracy of curve fitting can be achieved under certain conditions.

4.1   Introduction and Problem Formulation

The fitting of geometric primitives to a set of data points is one of the basic tasks in machine vision. It has been widely used in industrial automation, medical diagnosis, military robots, civil surveillance, and etc. Implementation of the fitting algorithms may become challenging where real-time performance is required. Basically the algorithms can be divided into two broad categories:

```
                          ┌──────────────┐
                          │  Emissivity  │
                          │  Correction  │
                          └──────────────┘
                                 │
                                 ▼
┌──────────────┐      ┌──────────────┐      ┌──────────────┐
│              │      │    Image     │      │              │
│ Visual Image │─────▶│Correspondence/│◀────│ Thermal Image│
│              │      │ Registration │      │              │
└──────────────┘      └──────────────┘      └──────────────┘
       │                     │                     │
       ▼                     │                     │
┌──────────────┐             │                     │
│    Image     │             │                     │
│  Processing  │             │                     │
└──────────────┘             ▼                     │
       │             ┌──────────────┐              │
       └────────────▶│ Image Fusion │◀─────────────┘
                     └──────────────┘
```
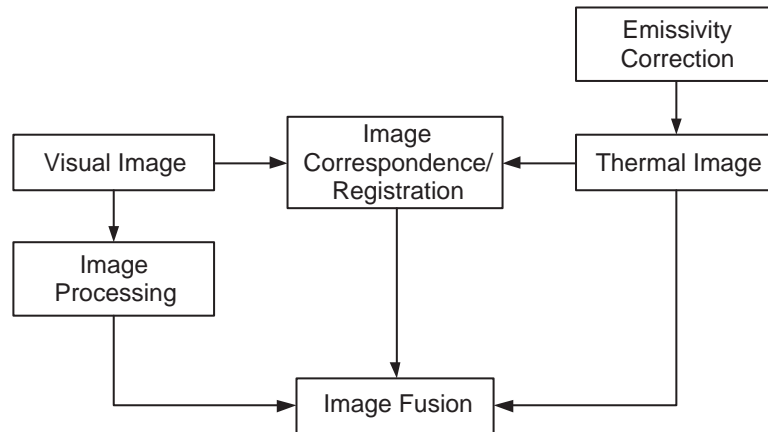
Figure 4.1: Flow chart of 2D temperature measurement.

1. Clustering/voting techniques. Each data point is first classified into one or more classes according to some criteria, then the optimal solution can be obtained by a voting process. It includes RANSAC, Hough transform, Kalman filtering, fuzzy cluster and etc [38, 39, 40]. These methods are generally robust, but are time-demanding. Therefore, they are not suitable for real-time application;

2. Least square method. It uses geometric or algebraic distance as a cost function to be minimized [41, 42, 43, 44, 45, 46, 47, 48]. It is generally computationally efficient, but suffers from the outliers in the data set. A simple example is illustrated in Figure 4.2, where the dotted line is the true ellipse, the small circles are noise-free data point sampled from the ellipse with only one outlier added (very right). The solid line is the fitted ellipse, which is severely biased by the least square method.

So the question to be addressed in this chapter can be formulated as: is it possible to find an algorithm that can tolerate the measurement outliers or noises to achieve

44
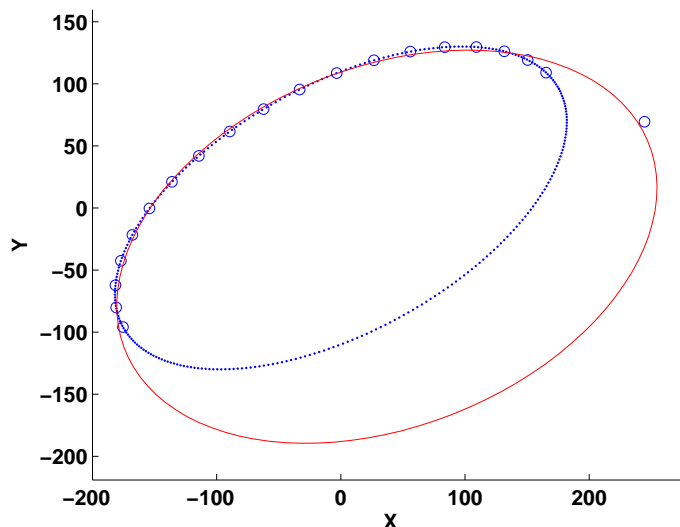
Figure 4.2: Failure of least square method to find an appropriate solution: the dotted line is the true ellipse (inner circle), the small circles are noise-free data point sampled from the ellipse with only one outlier (very right), and the solid line is the ellipse obtained through least square method (outer circle).

superaccuracy while has a fast convergence rate? In [49], the author claims that the regression diagnostics approach depends heavily on a priori knowledge in choosing the thresholds for outlier rejection. It will be shown in this section that the claim is no longer hold for the proposed method.

The flowchart of the 2D temperature measurement is illustrated in Figure 4.1. It is clear from the flowchart that the following problems have to be addressed for a 2D thermal measurement system:

1. Emissivity of the die insert must be determined as it is a critical parameter for an infrared thermometer;

2. Image registration/correspondence has to be performed to align the thermal and visual images such that cross reference between images can be established; and

3. Local shape of a target will be carefully extracted from the visual image in order to get accurate temperature of each die insert.

The concept of 'adaptive' will be adopted from signal processing field [35] to describe the converging behavior of the proposed ellipse fitting technique.

4.2   Digital Images

Gray level digital images are presented as a two-dimensional array of numbers with each element in the array called a pixel. Each number stands for the intensity of the image at that relative position. Each gray level is represented with 8-bit, 10-bit, 12-bit, 14-bit, 16-bit or floating points encoding. For an 8-bit encoding, the intensity is allowed 2^8 or 256 possible values. These values are usually assigned integer values ranging from 0 to 255 with 0 being the darkest gray level and 255 the brightest intensity level. Figure 4.3 shows a four pixel digital image, where it can be interpreted as an intensity (or brightness) map I defined on a discretized compact region Ω of a two-dimensional surface:

$$I : \Omega \subset \mathbb{Z}^2 \rightarrow \mathbb{Z}_+; \quad (x, y) \mapsto I(x, y)$$

For an 8-bit gray level image, $I(x, y) \in [0, 255]$.

The most commonly used color image is encoded as either a red, green and blue (RGB) image or hue, saturation and luminance (HSL) image. The representation of
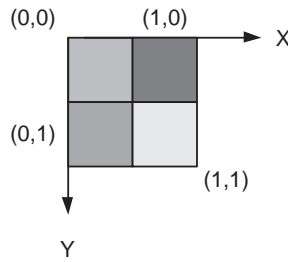
Figure 4.3: Representation of a four-pixel digital image.

a color image is similar to that of a gray level image except that the number of each pixel represents three primitives: red, green and blue (if in RGB) or hue, saturation and luminance (if in HSL). For example, if each primitive is encoded as 8-bit value, then a color pixel is represented as 32-bit with the first 8-bit as unused alpha plane.

As mentioned before, thermal image is formed by measuring the infrared energy emitted by an object. Originally, it is a gray level image that the intensity is proportional to the surface temperature of the object. False or artificial color palette is added to transform the original image to its color counterpart for better visual effect. Extra care should be taken when manipulating thermal image since it contains the temperature information of the object. Image processing algorithm may alter the gray level value hence the temperature map of the object, which is unacceptable for accurate temperature measurement.

4.3 Visual Image Processing

Since digital image is a typical two-dimensional sampled signal, it can be processed as a two-dimensional systems as illustrated in Figure 4.4, where $I(x, y)$ is the intensity value of an image at location (x, y) and $h(x, y)$ is the impulse response of a two-

$$I(n_1, n_2) \quad\longrightarrow\quad \boxed{h(n_1, n_2)} \quad\longrightarrow\quad y(n_1, n_2)$$
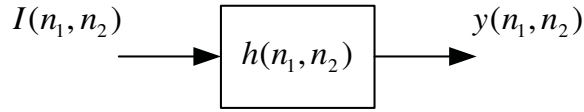
Figure 4.4: Processing of a two-dimensional digital image.

Visual Image $\longrightarrow$ | Image Enhancement | $\longrightarrow$ | Edge Detection | $\longrightarrow$ | Object Localization |
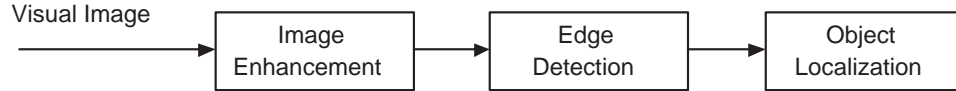
Figure 4.5: Visual image processing.

dimensional system such as a high pass filter. For a linear shift-invariant system (LSI), the output $Y(x, y)$ can be determined by [50]:

$$Y(x, y) = I(x, y) \circledast h(x, y)$$

where $\circledast$ denotes convolution. The above equation can be further written as

$$Y(x, y) = \sum_{k_1=-\infty}^{\infty} \sum_{k_2=-\infty}^{\infty} I(k_1, k_2) h(x - k_1, y - k_2)$$

As image and its filter have finite size in practice, for an $M \times N$ sized image and an $m \times m$ filter where m is a positive odd number and $m < N, m < M, N \in \mathbb{Z}_+, M \in \mathbb{Z}_+$, the above equation can be rewritten as

$$Y(x, y) = \sum_{k_1=-\frac{m-1}{2}}^{\frac{m-1}{2}} \sum_{k_2=-\frac{m-1}{2}}^{\frac{m-1}{2}} I(k_1, k_2) h(x - k_1, y - k_2) \qquad (4.1)$$

The above equation plays a critical role in image filtering theory, which lays the foundation for the image processing algorithms.

The main purpose of the visual image processing is to estimate the shape and location of the die inserts from their images. A snapshot of the inserts from visual

camera 1 is illustrated in Figure 4.6(a). Before the shape of each channel can be localized, the image must undergo some algorithms in order to extract its global or local features. The process is illustrated in Figure 4.5 and carried out from Algorithm 5.7 to 4.3.

4.3.1   Image enhancement

Since the insert surface is very dark (having a low intensity value in the image), the original image is transformed to turn the dark region into bright one for better visual perception.

Algorithm 4.1. *Image enhancement [36, 50, 73].*

1. *Image inverse: For each pixel in the image $I(x, y)$, let*

$$I_N(x, y) = 255 - I(x, y)$$

   where $I_N(x, y)$ stands for the new intensity value for the transformed image. After inversion, the bright regions are now containing useful information of the image.

2. *A look-up table transformation is adopted to extract the images of the insert surfaces. For each image pixel $I_N(x, y)$, let $I'_N(x, y)$ be the new pixel value such that*

$$I'_N(x, y) = \begin{cases} I_N(x, y) & if \quad I_N(x, y) \in [220, 255] \\ 0 & otherwise \end{cases}$$

3. *(optional) Exponential transformation: to further decrease the brightness and contrast in dark regions, an exponential transformation can be applied. This operation will also increase the contrast in bright regions.* ◇

The output of the algorithm is shown in Figure 4.6(b), where the insert surfaces are highlighted after enhancement for further processing.

4.3.2   Edge detection

The most commonly used image feature is edges that are defined as pixels at or around which the image values change sharply. It is assumed that the acquired image is noisy, so a Gaussian filter is applied to smooth the noise. A zero mean 1-D Gaussian filter with variance σ is given by

$$g(x) = \frac{1}{\sqrt{2\pi}\sigma} exp(-\frac{x^2}{2\sigma^2})$$

Since image can be deemed as a two dimensional system, convolving it with a 2-D Gaussian kernel $g(x,y)$ as in Equation (4.1) can be written as [36, 73]

$$
\begin{aligned}
I_g(x,y) &= I(x,y) \circledast g(x,y) \\
&= \sum_{k_1=-\frac{m-1}{2}}^{\frac{m-1}{2}} \sum_{k_2=-\frac{m-1}{2}}^{\frac{m-1}{2}} g(k_1,k_2) I(x-k_1, y-k_2) \\
&= \frac{1}{2\pi\sigma^2} \sum_{k_1=-\frac{m-1}{2}}^{\frac{m-1}{2}} \sum_{k_2=-\frac{m-1}{2}}^{\frac{m-1}{2}} exp(-\frac{k_1^2+k_2^2}{2\sigma^2}) I(x-k_1, y-k_2) \\
&= \frac{1}{2\pi\sigma^2} \sum_{k_1=-\frac{m-1}{2}}^{\frac{m-1}{2}} exp(-\frac{k_1^2}{2\sigma^2}) \sum_{k_2=-\frac{m-1}{2}}^{\frac{m-1}{2}} exp(-\frac{k_2^2}{2\sigma^2}) I(x-k_1, y-k_2) \\
&= I(x,y) \circledast g(x) \circledast g(y) \qquad (4.2)
\end{aligned}
$$

It is clear that a 2-D Gaussian mask can be separated into two kernels under convolution. Therefore, Gaussian smoothing can be computed by convolving first all rows, then all columns of an image with a 1-D Gaussian kernel. In practice, a discrete
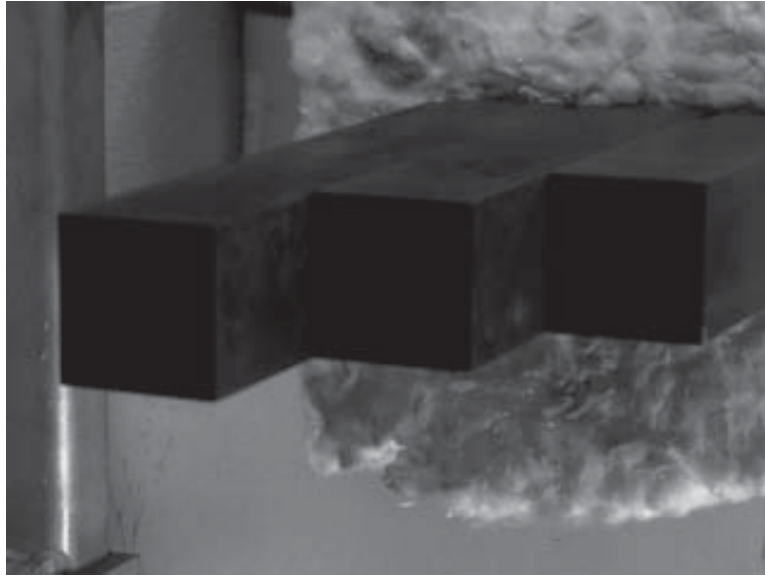
(a) original visual image
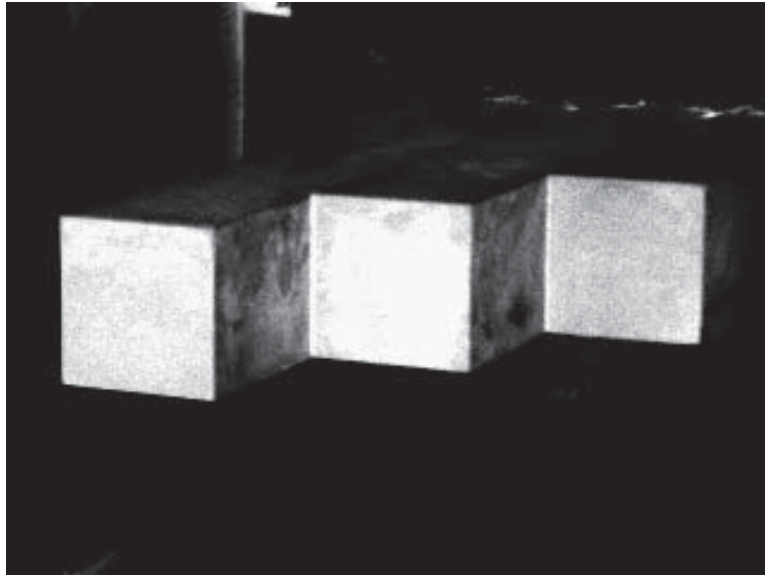
(b) enhanced image

Figure 4.6: Image enhancement: the insert surfaces are highlighted after enhancement.

Gaussian mask is obtained by sampling a continuous Gaussian via [36, 73]

$$\sigma = w/5$$

where w is the mask width taken as an odd number. The discrete type can subtends 98.76% of the area of the continuous one and can be further approximated to an integer form. Let $f[x]$ be a sampled version from a continuous signal $f(x)$

$$f[x] = f(xT), \quad x \in \mathbb{Z}$$

where T is the sampling period. From the well-known Nyquist sampling theorem [37], the band-limited continuous signal $f(x)$ can be reconstructed from its sampled signal $f[x]$ provided that the sampling frequency is at least twice than the Nyquist frequency of $f(x)$. That is

$$f(x) = f[x] \circledast h(x), \quad x \in \mathbb{R}$$

where the reconstruction filter $h(x)$ is an ideal sync function given by

$$h(x) = \frac{sin(\pi x/T)}{\pi x/T}, \quad x \in \mathbb{R}$$

The computation of the derivative of a sampled signal $f[x]$ is first by applying the derivative operator $D\{\cdot\}$ to the continuous function $f(x)$, then taking the sampling operator $S\{\cdot\}$ to the derivative. The derivative is given by

$$
\begin{aligned}
f'(x) &= D\{f(x)\} = D\{f[x] \circledast h(x)\} \\
&= D\{\sum_{k=-\infty}^{\infty} f[x]h(x-k)\} \\
&= \sum_{k=-\infty}^{\infty} f[x]D\{h(x-k)\} \\
&= f[x] \circledast D\{h(x)\} = f[x] \circledast h'(x)
\end{aligned}
$$

And the sampled version of the derivative can be calculated as

$$S\{f'(x)\} = S\{f[x] \circledast h'(x)\} = f[x] \circledast S\{h'(x)\} = f[x] \circledast h'[x]$$

An ideal sync function is infinite and in practice, it can be approximated once again by a truncated Gaussian filter.

In a similar way, a 2-D continuous signal $f(x, y)$ can be reconstructed from its sampled signal $f[x, y]$ with a sync function $h(x, y)$

$$f(x, y) = f[x, y] \circledast h(x, y), \quad x, y \in \mathbb{R}$$

with

$$h(x, y) = \frac{sin(\pi x/T) sin(\pi y/T)}{\pi^2 xy/T^2} = h(x)h(y), \quad x, y \in \mathbb{R}$$

And the partial derivatives of the sampled signal $f[x, y]$ are given by

$$f_x[x, y] = f[x, y] \circledast h'[x] \circledast h[y]$$

$$f_y[x, y] = f[x, y] \circledast h[x] \circledast h'[y]$$

Although image is a typical discrete 2-D signal, in image processing algorithms, the symbol $I(x, y)$ instead of $I[x, y]$ is adopted by convention. Under this convention, the image gradient $\nabla I(x, y) = [I_x(x, y), I_x(x, y)]^T \in \mathbb{R}^2$ at location $(x, y)^T \in \mathbb{Z}^2$ can be calculated as [36, 73]

$$
\begin{aligned}
I_x(x, y) &= \frac{\partial I(x, y)}{\partial x} = I(x, y) \circledast g'(x) \circledast g(y) \\
&= \sum_{k_1 = -\frac{m-1}{2}}^{\frac{m-1}{2}} \sum_{k_2 = -\frac{m-1}{2}}^{\frac{m-1}{2}} I(k_1, k_2) g'(x - k_1) g(y - k_2) \quad (4.3) \\
I_y(x, y) &= \frac{\partial I(x, y)}{\partial y} = I(x, y) \circledast g(x) \circledast g'(y) \\
&= \sum_{k_1 = -\frac{m-1}{2}}^{\frac{m-1}{2}} \sum_{k_2 = -\frac{m-1}{2}}^{\frac{m-1}{2}} I(k_1, k_2) g(x - k_1) g'(y - k_2) \quad (4.4)
\end{aligned}
$$

53

The algorithm implemented here is a modified Canny edge detector that can reduce the probability of false and streaking contours.

Algorithm 4.2. *Edge detection [36, 50, 73]. The input is an image $I(x, y)$ and a threshold $\tau > 0$, for each pixel at $(x, y) \in \mathbb{Z}^2$*

1. *Apply Gaussian smoothing filter to the image as per Equation (4.2);*

2. *Compute the gradient $\nabla I = [I_x, I_y]^T$ at each pixel according the formulea (4.3) and (4.4);*

3. *Estimate the edge strength*

$$\|\nabla I(x, y)\|^2 = \nabla I^T \nabla I = I_x^2 + I_y^2$$

   and the orientation of the edge normal

$$\mathbf{n}(x, y) = arctan(I_y/I_x)$$

4. *Approximate the edge normal to one of the four directions 0°, 45°, 90° and 135°, if $\|\nabla I(x, y)\|$ is smaller than at least one of its two neighbors along the direction, assign $\|\nabla I(x, y)\| = 0$ to thin the edge points;*

5. *Follow the chains of the connected local maxima, if $\|\nabla I(x, y)\| > \tau$, mark it as an edge pixel.* ◇

When real-time performance is required for an imaging system, the edge detection algorithms can be simplified in a way such that images are convoluted with predefined filters, such as Sobel filters, Laplacian kernels, Gaussian kernels, and etc [36, 50, 73]. The output of the algorithm is given in Figure 4.7.
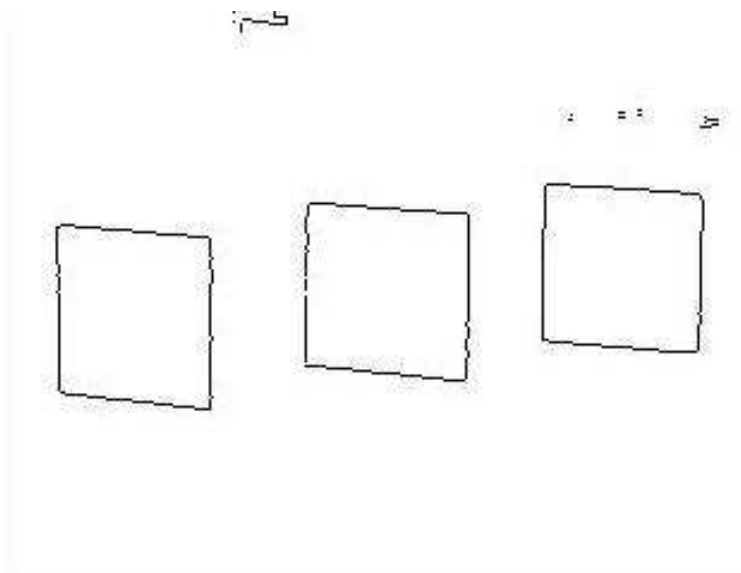
Figure 4.7: Detected edge of the insert surface.

4.3.3 Object localization

The contours of the objects are defined by the edge points detected from the above algorithm. To find an appropriate model for a local shape, there are usually two procedures to go. Firstly, the edge points must be grouped for each instance of the target curve. The step has been fulfilled in the last algorithm since the normal of the edge has been identified and the chain of the local maxima has been connected. Secondly, the best curve has to be found to interpolating the points. Hough Transform is one of the most widely used methods for curve detection [36], which divides the parameter space into small regions and counts for how many votes that each point casts for all combinations of parameters if it were part of the target curve. The transform copes well with occlusion, but becomes extensively time consuming as the size of the parameter space increases exponentially with the number of model parameters.

Once a set of image points has been identified, ellipse fitting is usually adopted to generate a function for the given points. As the acquired image is contaminated by noise, spurious peaks or outliers that do not fit the trend set by the balance of the data. Generally speaking, there are two types of outlier models:

1. Mean shift outlier model has a breakdown at the ith point, which produces a location shift;

2. Variance shift model has a breakdown at the ith point where its error variance exceeds the error variance at the other data points.

The regression model can be significantly biased if the outliers have large mean and/or variance shifts, imposing an adverse impact on the accuracy of the object localization and hence temperature measurement.

In this section, a novel robust fitting method is proposed based on statistical diagnostics. The basic idea is that the residual magnitude is expected to be large at a specific data point in the above mentioned outlier models. The outliers are first detected, a linear model is then derived to find the local shape.

Consider the generalized linear model with n observations of the paired variable $(\mathbf{X}, \mathbf{y})$:

$$\mathbf{y} = \mathbf{X}\beta + \epsilon \tag{4.5}$$

where $\mathbf{X} \in \mathbb{R}^{n \times (k+1)}$ are inputs with full column rank, $\mathbf{y} \in \mathbb{R}^{n \times 1}$ are the measured response, $\beta \in \mathbb{R}^{(k+1) \times 1}$ are unknown regression coefficients to be found, $\epsilon \in \mathbb{R}^{n \times 1}$ are the model error, and

$$
\mathbf{y} = \begin{bmatrix} y_1 \\ y_2 \\ \vdots \\ y_n \end{bmatrix}, \quad
\mathbf{X} = \begin{bmatrix} \mathbf{1} \\ \mathbf{X_1} \\ \mathbf{X_2} \\ \vdots \\ \mathbf{X_k} \end{bmatrix}^T =
\begin{bmatrix}
1 & x_{11} & x_{21} & \cdots & x_{k1} \\
1 & x_{12} & x_{22} & \cdots & x_{k2} \\
\vdots & \vdots & \vdots & & \vdots \\
1 & x_{1n} & x_{2n} & \cdots & x_{kn}
\end{bmatrix},
$$

$$
\beta = \begin{bmatrix} \beta_0 \\ \beta_1 \\ \beta_2 \\ \vdots \\ \beta_k \end{bmatrix}, \quad
\epsilon = \begin{bmatrix} \epsilon_1 \\ \epsilon_2 \\ \vdots \\ \epsilon_n \end{bmatrix}.
$$

where $\mathbf{X_i} \in \mathbb{R}^{n \times 1}$ is column vector with

$$
\mathbf{X_i} = [x_{i1}, x_{i2}, \cdots, x_{in}]^T \quad (i = 1, 2, \cdots, k).
$$

Also define a colomn vector $\mathbf{x_i} \in \mathbb{R}^{(k+1) \times 1}$ as

$$
\mathbf{x_i} = [1, x_{1i}, x_{2i}, \cdots, x_{ki}]^T
$$

Therefore, $(y_i, \mathbf{x_i})$ is the i-th observed data point with $i = 1, 2, \cdots, n$.

Let $\mathbf{b} \in \mathbb{R}^{(k+1) \times 1}$ be the estimator for the regression coefficients β, then for the least square method (LS) $\mathbf{b}$ satisfies

$$
\frac{\partial}{\partial \mathbf{b}}[(\mathbf{y} - \mathbf{Xb})^{\mathbf{T}}(\mathbf{y} - \mathbf{Xb})] = -2\mathbf{X^T y} + 2(\mathbf{X^T X})\mathbf{b} = \mathbf{0}
$$

It is easy to show that with a full column rank matrix $\mathbf{X}$

$$
\mathbf{b} = (\mathbf{X^T X})^{-1}\mathbf{X^T y} \tag{4.6}
$$

where matrix $\mathbf{X^T X}$ is symmetric and can be calculated as

$$
\mathbf{X^T X} =
\begin{bmatrix}
n & \sum_{i=1}^{n} x_{1i} & \sum_{i=1}^{n} x_{2i} & \cdots & \sum_{i=1}^{n} x_{ki} \\
& \sum_{i=1}^{n} x_{1i}^2 & \sum_{i=1}^{n} x_{1i}x_{2i} & \cdots & \sum_{i=1}^{n} x_{1i}x_{ki} \\
& & \sum_{i=1}^{n} x_{2i}^2 & \cdots & \sum_{i=1}^{n} x_{2i}x_{3i} \\
& & & \ddots & \vdots \\
& & & & \sum_{i=1}^{n} x_{ki}^2
\end{bmatrix} \in \mathbb{R}^{(k+1) \times (k+1)}
$$

It is clear that the diagonal elements of the matrix $\mathbf{X^T X}$ are the sums of the squares of the elements in $\mathbf{X_i}$, and its off diagonal elements are sums of cross products of elements in $\mathbf{X_i}$. Define a matrix $\mathbf{H} \in \mathbb{R}^{n \times n}$ as

$$\mathbf{H} = \mathbf{X(X^T X)^{-1} X^T}$$

$\mathbf{H}$ is also called HAT matrix. It can be seen that $\mathbf{H}$ is idempotent (i.e. symmetric and $\mathbf{H^2} = \mathbf{H}$) with its diagonal elements given by

$$h_{ii} = \mathbf{x_i^T (X^T X)^{-1} x_i}$$

and off-diagonal elements are given by

$$h_{ij} = \mathbf{x_i^T (X^T X)^{-1} x_j} \quad (i \neq j)$$

Then $\hat{\mathbf{y}} \in \mathbb{R}^{n \times 1}$, the predicted value of $\mathbf{y}$ can be written as

$$\hat{\mathbf{y}} = \mathbf{Xb} = \mathbf{X(X^T X)^{-1} X^T y} = \mathbf{Hy}$$

and

$$\hat{y}_i = \mathbf{x_i^T (X^T X)^{-1} X^T y} \tag{4.7}$$

and the vector of residuals $\mathbf{e} = [e_1, e_2, \cdots, e_n]^T \in \mathbb{R}^{n \times 1}$ are given by

$$\mathbf{e} = \mathbf{y} - \hat{\mathbf{y}} = \mathbf{y} - \mathbf{Xb} = \mathbf{y} - \mathbf{X(X^T X)^{-1} X^T y} = \mathbf{[I - H]y} \tag{4.8}$$

The residual of the regression is simply taken the form

$$e_i = y_i - \hat{y}_i$$

As $\mathbf{H}$ is idempotent,

$$\mathbf{H\hat{y}} = \mathbf{H(Hy)} = \mathbf{H^2 y} = \mathbf{Hy}$$

58

which implies $\mathbf{H}(\mathbf{y} - \hat{\mathbf{y}}) = \mathbf{H}\mathbf{e} = \mathbf{0}$, i.e., $\sum_{j=1}^{n} e_j h_{ij} = 0$. Also from $\mathbf{H^2} = \mathbf{H}$, it implies $\sum_{j=1}^{n} h_{ij}^2 = h_{ii}$.

Since there are $k+1$ parameters to be estimated from n observations, the unbiased estimator s^2 for the residual variance can be written as

$$s^2 = \frac{(\mathbf{y} - \mathbf{Xb})^{\mathbf{T}}(\mathbf{y} - \mathbf{Xb})}{n - (k+1)} = \sum_{i=1}^{n} \frac{(y_i - \hat{y}_i)^2}{n - (k+1)}$$

In order to detect if a set of data is an outlier or not, a PRESS (prediction sum of squares) statistic is used. First, the $i-$th observation $(y_i, \mathbf{x_i})$ is removed from the data set where $i = 1, 2, \cdots, n$, then the remaining $n-1$ observations are used to estimate a new set of regression coefficients $\mathbf{b_{-i}}$. The predicted value at point $\mathbf{x_i}$ is given by

$$\hat{y}_{i,-i} = \mathbf{x_i^T}\mathbf{b_{-i}}$$

where the subscript of $\hat{y}_{i,-i}$ means the predicted value at i-th point but the regression model is obtained excluding the i-th point. The PRESS residual is obtained as

$$e_{i,-i} = y_i - \hat{y}_{i,-i} = y_i - \mathbf{x_i^T}\mathbf{b_{-i}} \tag{4.9}$$

Accordingly, the PRESS is defined as

$$PRESS = \sum_{i=1}^{n}(e_{i,-i})^2 = \sum_{i=1}^{n}(y_i - \hat{y}_{i,-i})^2$$

It appears that for n observations, the regression process needs to be repeated n times in order to find the prediction error, but the PRESS statistic has some nice properties that can greatly simplify the computation [58, 59, 60].

Similar to Equation (4.6) if the method of sum of squares is used, the regression coefficients $\mathbf{b_{-i}}$ can be obtained as:

$$
\begin{aligned}
\mathbf{b_{-i}} &= (\mathbf{X_{-i}^T X_{-i}})^{-1} \mathbf{X_{-i}^T y_{-i}} \\
&= (\mathbf{X^T X} - \mathbf{x_i x_i^T})^{-1} \mathbf{X_{-i}^T y_{-i}} \quad (4.10)
\end{aligned}
$$

Recall that, for a $n \times n$ nonsingular matrix $\mathbf{M}$ and a $n \times 1$ vector $\mathbf{v}$, the Sherman-Morrison-Woodbury theorem states that:

$$
(\mathbf{M} - \mathbf{v v^T})^{-1} = \mathbf{M^{-1}} + \frac{\mathbf{M^{-1} v v^T M^{-1}}}{1 - \mathbf{v^T M^{-1} v}}
$$

The Equation (4.10) can be rewritten as [58, 59, 60]:

$$
\begin{aligned}
\mathbf{b_{-i}} &= \left[(\mathbf{X^T X})^{-1} + \frac{(\mathbf{X^T X})^{-1} \mathbf{x_i x_i^T} (\mathbf{X^T X})^{-1}}{1 - \mathbf{x_i^T M^{-1} x_i}} \right] \mathbf{X_{-i}^T y_{-i}} \\
&= \left[(\mathbf{X^T X})^{-1} + \frac{(\mathbf{X^T X})^{-1} \mathbf{x_i x_i^T} (\mathbf{X^T X})^{-1}}{1 - h_{ii}} \right] \mathbf{X_{-i}^T y_{-i}} \quad (4.11) \\
&= \left[(\mathbf{X^T X})^{-1} + \frac{(\mathbf{X^T X})^{-1} \mathbf{x_i x_i^T} (\mathbf{X^T X})^{-1}}{1 - h_{ii}} \right] (\mathbf{X^T y} - \mathbf{x_i} y_i) \\
&= \mathbf{b} - (\mathbf{X^T X})^{-1} \mathbf{x_i} y_i + \frac{(\mathbf{X^T X})^{-1} \mathbf{x_i x_i^T} (\mathbf{X^T X})^{-1} (\mathbf{X^T y} - \mathbf{x_i} y_i)}{1 - h_{ii}} \\
&= \mathbf{b} - (\mathbf{X^T X})^{-1} \mathbf{x_i} \frac{y_i (1 - h_{ii}) - \mathbf{x_i^T b} + h_{ii} y_i}{1 - h_{ii}} \\
&= \mathbf{b} - (\mathbf{X^T X})^{-1} \mathbf{x_i} \frac{y_i - \hat{y}_i}{1 - h_{ii}} \\
&= \mathbf{b} - \frac{(\mathbf{X^T X})^{-1} \mathbf{x_i} e_i}{1 - h_{ii}} \quad (4.12)
\end{aligned}
$$

Substituting the Equation (4.11) into (4.9), the residual can be obtained as:

$$
\begin{aligned}
e_{i,-i} &= y_i - \mathbf{x_i^T} (\mathbf{X^T X})^{-1} \mathbf{X_{-i}^T y_{-i}} - \frac{h_{ii} \mathbf{x_i^T} (\mathbf{X^T X})^{-1} \mathbf{X_{-i}^T y_{-i}}}{1 - h_{ii}} \\
&= \frac{(1 - h_{ii}) y_i - \mathbf{x_i^T} (\mathbf{X^T X})^{-1} \mathbf{X_{-i}^T y_{-i}}}{1 - h_{ii}} \\
&= \frac{(1 - h_{ii}) y_i - \mathbf{x_i^T} (\mathbf{X^T X})^{-1} (\mathbf{X^T y} - \mathbf{x_i} y_i)}{1 - h_{ii}}
\end{aligned}
$$

60

$$
\begin{aligned}
&= \frac{(1 - h_{ii})y_i - \hat{y}_i + h_{11}y_i}{1 - h_{ii}} \\
&= \frac{y_i - \hat{y}_i}{1 - h_{ii}} \\
&= \frac{e_i}{1 - h_{ii}} \quad\quad (4.13)
\end{aligned}
$$

Similarly, since there are $k+1$ parameters to be estimated from $n-1$ observations for the PRESS statistic, the unbiased estimator s^2_{-1} for the residual variance can be written as

$$
\begin{aligned}
(n - k - 2)s^2_{-i} &= (\mathbf{y} - \mathbf{Xb_{-i}})^\mathbf{T}(\mathbf{y} - \mathbf{Xb_{-i}}) \\
&= \sum_{\substack{j=1 \\ j\neq i}}^{n}(y_j - \mathbf{x_j^T b_{-i}})^2 \quad \text{(substitute Equation (4.12))} \\
&= \sum_{j=1}^{n}\left(y_j - \mathbf{x_j^T b} + \frac{\mathbf{x_j^T(X^T X)^{-1} x_i}e_i}{1 - h_{ii}}\right)^2 - \left(y_i - \mathbf{x_i^T b} + \frac{h_{ii}e_i}{1 - h_{ii}}\right) \\
&= \sum_{j=1}^{n}\left(e_j + \frac{h_{ij}e_i}{1 - h_{ii}}\right)^2 - \frac{e_i^2}{(1 - h_{ii})^2} \\
&= \sum_{j=1}^{n}e_j^2 + \frac{2e_i}{1 - h_{ii}}\sum_{j=1}^{n}e_j h_{ij} + \frac{e_i^2}{(1 - h_{ii})^2}\sum_{j=1}^{n}h_{ij}^2 - \frac{e_i^2}{(1 - h_{ii})^2} \\
&= \sum_{j=1}^{n}e_j^2 + \frac{h_{ii}e_i^2}{(1 - h_{ii})^2} - \frac{e_i^2}{(1 - h_{ii})^2} \\
&= \sum_{j=1}^{n}e_j^2 - \frac{e_i^2}{1 - h_{ii}} \\
&= (n - k - 1)s^2 - \frac{e_i^2}{1 - h_{ii}} \quad\quad (4.14)
\end{aligned}
$$

It is clear from Equations (4.9) and (4.14) that the PRESS residual and variance can be calculated directly from the ordinary residual and variance, which greatly eases the burden to repeat $n - 1$ regressions, and hence significantly reduces the computational cost. Once the residual and variance are obtained, the outliers can be

detected by hypothesis testing. For the mean shift outlier model, the mean of the i-th PRESS residual is used. The hypothesis is given by:

$$H_0 : E(e_{i,-i}) = 0$$
$$H_1 : E(e_{i,-i}) \neq 0 \qquad (4.15)$$

For the variance shift model, the so-called R-student distribution is employed, which is given by

$$t_i = \frac{e_i}{s_{-i}\sqrt{1 - h_{ii}}} \qquad (4.16)$$

In the case, s_{-i}, the estimate of true variance σ, is used. The hypothesis can be written as

$$H_0 : \sigma_i^2 = 0$$
$$H_1 : \sigma_i^2 \neq 0 \qquad (4.17)$$

The confidence level of the testing is usually taken at $\alpha = 0.05$. Once the outlier is detected, it will be excluded from the data set, then a new linear model is rebuilt and the process is repeated. In practice, the method can be combined with other curve fitting techniques to generate more robust results. One of the most useful tools for curve detection is ellipse fitting. Consider the ellipse model with a set of data point $\mathbf{p}_i = [x_i, y_i]^T$ with $i = 1, 2, \cdots, n$:

$$F(\mathbf{X}, \mathbf{b}) = \mathbf{X^T b} = ax^2 + bxy + cy^2 + dx + ey + f = 0 \qquad (4.18)$$

where $\mathbf{b} = [f, a, b, c, d, e]^T$ is the regression coefficient and $\mathbf{X} = [1, x^2, xy, y^2, x, y]^T$. $|F(\mathbf{X_i}, \mathbf{b})|$ is called the algebraic distance of a point (x_i, y_i) to the ellipse $F(\mathbf{X}, \mathbf{b}) = 0$. The purpose of the fitting is to find a curve that minimizes the cost function

$$\mathcal{D}_B(\mathbf{b}) = \sum_{i=1}^{n} (F(\mathbf{X}_i)^2$$

In order to avoid trivial solution $\mathbf{b} = \mathbf{0}$ and ensure that the curve is an ellipse, the following constrain is applied:

$$\mathbf{b}^T \begin{bmatrix} 0 & 0 & 2 & 0 & 0 & 0 \\ 0 & -1 & 0 & 0 & 0 & 0 \\ 2 & 0 & 0 & 0 & 0 & 0 \\ 0 & 0 & 0 & 0 & 0 & 0 \\ 0 & 0 & 0 & 0 & 0 & 0 \\ 0 & 0 & 0 & 0 & 0 & 0 \end{bmatrix} \mathbf{b} = \mathbf{b}^T \mathcal{C} \mathbf{b} = 1$$

Therefore the algebraic fitting problem becoms:

$$\min_{\mathbf{b}} \|\mathbf{b}^{\mathbf{T}} \mathbf{X}^{\mathbf{T}} \mathbf{X} \mathbf{b}\|$$
$$\text{subject to: } \mathbf{b}^T \mathcal{C} \mathbf{b} = 1$$

Let λ be a Lagrange multiplier, using least square method (LS), an object function can be defined as

$$\mathcal{L} = \mathbf{b}^{\mathbf{T}} \mathbf{X}^{\mathbf{T}} \mathbf{X} \mathbf{b} - 2\lambda(\mathbf{b}^T \mathcal{C} \mathbf{b} - 1)$$

The minimum value is attained when $\frac{\partial \mathcal{L}}{\partial \mathbf{b}} = 0$, which yields

$$\mathbf{X}^{\mathbf{T}} \mathbf{X} \mathbf{b} = \lambda \mathcal{C} \mathbf{b} \tag{4.19}$$

This is a generalized eigenvalue problem and the solution $\mathbf{b}_0$ is the eigenvector corresponding to the only negative eigenvalue [42]. The method has an intrinsic disadvantage that prevents it from finding an optimal solution when all the sampled data are perfectly lying on an ellipse. Under this circumstance, the matrix $\mathbf{X}^{\mathbf{T}} \mathbf{X}$ becomes identically singular and the trivial solution is $\mathbf{b} = \mathbf{0}$. There are generally two ways to fix this problem:

1. re-scaling the data points by:

$$\tilde{x}_{ij} = \frac{x_{ij} - \min\limits_{j=1}^{n}(x_{ij})}{s_x} - 1, \quad \tilde{y}_{ij} = \frac{y_{ij} - \min\limits_{j=1}^{n}(y_{ij})}{s_y} - 1$$

where the scaling factors are given by:

$$s_x = \frac{\max\limits_{j=1}^{n}(x_{ij}) - \min\limits_{j=1}^{n}(x_{ij})}{2}, \quad s_y = \frac{\max\limits_{j=1}^{n}(y_{ij}) - \min\limits_{j=1}^{n}(y_{ij})}{2}$$

The new matrix $\tilde{\mathbf{X}}^{\mathbf{T}}\tilde{\mathbf{X}}$ is partially extracted to find the eigenvalue [54].

2. re-scaling the input according to the above scheme, then adding small random noise to the data. The data is re-sampled to form the matrix $\tilde{\mathbf{X}}^{\mathbf{T}}\tilde{\mathbf{X}}$ [43].

In order to find the optimal approximation, the second method needs to be repeated for several times [43]. The final value of the ellipse parameters is taken by averaging over the replications. Therefore, it has higher computational cost than the first one, and hence is not preferred.

Algorithm 4.3. *The input to the algorithm is a set of image points. The procedures of the proposed robust object localization can be summarized as follows:*

1. *Use a numerical package to calculate the eigenvalue and hence find the solution of* **b** *in (4.19);*

2. *Construct a linear model according to Equations (4.5) and (4.6), and use the values of* **b** *from the above step as an initial guess;*

3. *Compute the PRESS residual and variance as per Equations (4.9) and (4.14) respectively;*

4. *Conduct the hypothesis testing in (4.15) and/or (4.17) to find outliers;*

5. *Exclude the outliers from the data set, then repeat above step 1-4 when necessary; The output* $\mathbf{b}_m$ *identifies the best fit ellipse .* ◇
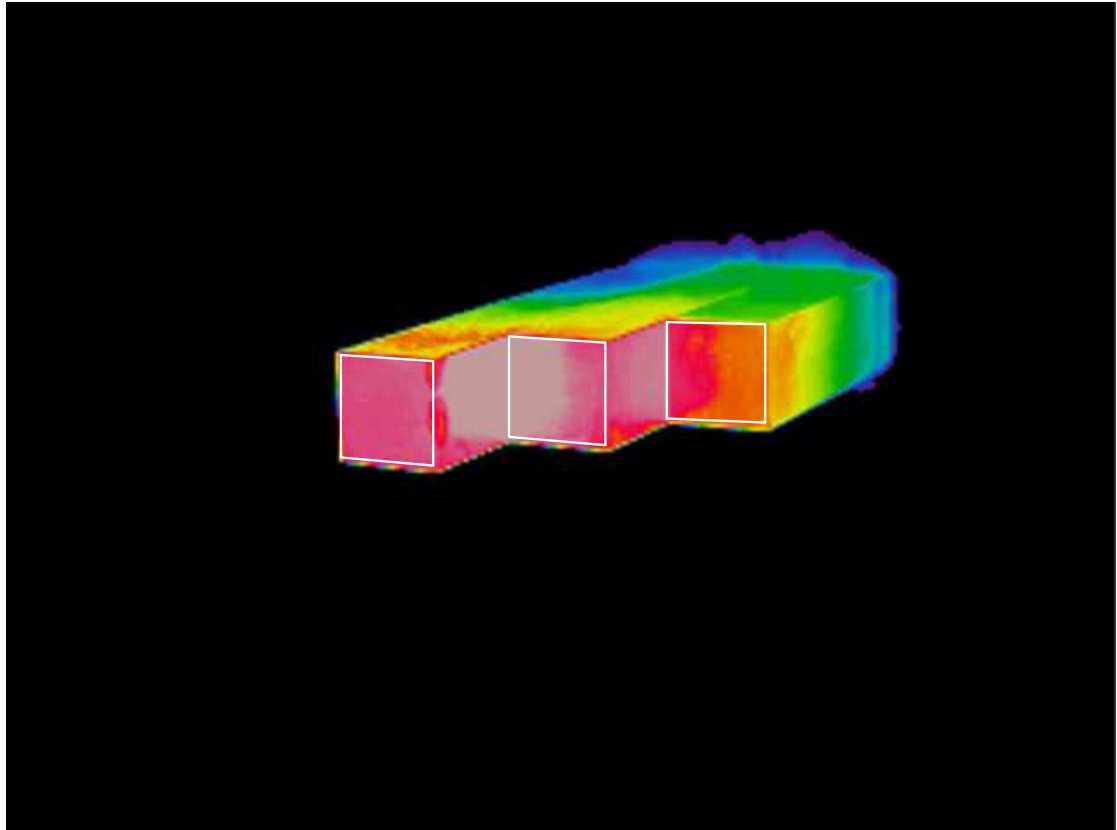
Figure 4.8: Registered and fused image: white boxes are from the visual camera (color online).

The algorithm can optimize its coefficients to achieve better robustness and accuracy. The experimental results of the object localization are presented in Section 4.5.

4.4 Image Correspondence

Image correspondence or registration is to precisely align two or more images such that the corresponding pixels in two images represent the same physical point in the

real world. There are various methods to conduct the registration, such as correlation method, Fourier method, feature-based method, active contours, point mapping, mutual information method, and etc. Reference [55] provides a recent survey on this topic.

Feature base method will be used due to simplicity and accuracy. It is assumed that: 1) there are non lens distortion in the images; 2) thermal image contains enough features such as edges, corners and etc in order to build up the correspondence, or the outer contour of the target in the thermal image is detectable. In projective geometry, straight lines in real world remain straight in images, but parallel lines converge toward so-called vanishing points. Since both visual image and thermal image are planar, they can be mapped through rigid body movement from one plane to another. The procedure is called projective transformation.

Let $[x, y, 1]^T \in \mathbb{R}^{3 \times 1}$ be the homogeneous coordinates of an image point p, and let $[X, Y, 1]^T \in \mathbb{R}^{3 \times 1}$ be the homogeneous coordinates of another image point P associated with the same object in real world, then the projective transformation can be written as

$$\kappa p = TP$$

where $k \in \mathbb{R}$ is a scale factor, and $T \in \mathbb{R}^{3 \times 3}$ is the projection matrix. The above equation can be solved to find κ and T through several linear equations. In the current setting, T for Channel 1 is given by:

$$T = \begin{bmatrix} 0.3819 & -0.0071 & 0.0000 \\ -0.0334 & 0.3429 & -0.0005 \\ 80.0661 & 59.6835 & 0.9274 \end{bmatrix}$$

The registered image are shown in Figure 4.8, where white boxes are the circumferences registered from visual image by projective transformation.

In the process of finding correspondence points, the thermal image must be properly controlled such that the corners of each insert are very clear in the image. The two camera can also be calibrated independently for feature based correspondence. More information can be found in next chapter.

4.5 Experimental Results

There are two main results to be shown in this subsection: the proposed method of robust object localization (called PRESS), and application results on the casting dies. First, the general procedures on how the Algorithm 4.3 works are explained, along with a qualitative comparison with a state-of-art robust method in [42, 43] (called B2AC), then the detailed quantitative comparisons are presented under different influential factors such as noise, occulsion. Finally, the method is applied to measure the temperature of the die surface to obtain the effect of the water flow on the die temperature.

4.5.1 Experiment 1: general results

In order to test the robustness of Algorithm 4.3, synthesized data with controlled noises are first used. Its results are compared with the so-called B2AC method or its enhanced version (EB2AC) in [42, 43]. It has been shown that the B2AC/EB2AC method has better performance in terms of noise tolerance than its counterparts, such as BOOK [44], TAUB [45], GAND [46], BIAS [47], and etc. Therefore, it is *sufficient* to compare the proposed method with B2AC/EB2AC to show if the performance has been improved or not.

For the convenience of mathematical expression, the ellipse can be written as the follwing form

$$[c_x, c_y, r_x, r_y, \phi] \tag{4.20}$$

where (c_x, c_y) is the center of the ellipse, r_x and r_y are the semimajor and semiminor axis respectively, and ϕ is the counterclockwise orientation angle in radians or degrees of its major axis with respect to Cartesian X-axis.

Experiment Procedures 4.4. *This experiment is to obtain some initial results for the proposed robust object localization.*

1. *Sample the ellipse $[0, 0, 200, 100, 0.5\ rad]$ to obtain $N = 20$ points uniformly spaced around half of the circumference from $\theta = 0^o$ to 180° with respect to its major axis (i.e., half an ellipse can be seen, and the other half is occluded);*

2. *Add independent zero mean Gaussian noise with variance $\sigma^2 = 0.01 * r_y = 1$ to both $x's$ and $y's$ of the samples;*

3. *Turn 20% of the points (4 in this case) into outliers by adding a uniform deviate in $[-r_y, r_y]$ to their both coordinates. And now the samples are severely contaminated with noises;*

4. *Run B2AC and Algorithm 4.3 to get the comparative results.* ◇

An illustrative example is shown in Table 4.5.1 and Figure 4.9. In Table 4.5.1 the $\hat{F}_i$ is the predicted value of $\mathbf{F}$ in Equation (4.18). Since the true value $\mathbf{F} = 0$

$$e_i = \hat{F}_i - F_i = \hat{F}$$

Table 4.1: Adaptive process of the proposed ellipse fitting method.

No.	Points	$\hat{F}_i$	h_{ii}	s_{-i}	$t_i^{(1)}$	Removed	$t_i^{(2)}$	Removed	$t_i^{(3)}$
1	(257.10,135.87)	0.68	0.81	0.17	9.13	Yes			
2	(166.08,110.21)	-0.28	0.29	0.39	-0.88		1.39		0.67
3	(150.94,119.90)	-0.34	0.23	0.38	-0.99		0.15		0.14
4	(131.96,126.44)	-0.32	0.26	0.38	-0.96		-0.41		-0.15
5	(109.54,129.68)	-0.25	0.28	0.39	-0.75		-0.87		-0.42
6	(30.81,135.18)	0.49	0.32	0.36	1.64		4.26	Yes	
7	(56.13,125.68)	-0.06	0.17	0.40	-0.17		-1.27		-0.82
8	(26.45,119.56)	0.05	0.13	0.40	0.14		-0.86		-0.34
9	(-3.13,107.92)	0.05	0.12	0.40	0.14		-1.11		-1.07
10	(-32.01,96.18)	0.08	0.16	0.40	0.23		-0.61		-0.46
11	(-3.14,116.57)	0.32	0.21	0.39	0.93		1.21		3.28
12	(-90.31,59.89)	-0.08	0.21	0.40	-0.22		-0.40		-0.69
13	(-113.85,41.76)	-0.16	0.22	0.39	-0.46		-0.09		-0.27
14	(-138.41,19.19)	-0.25	0.21	0.39	-0.74		0.27		0.30
15	(-153.42,-1.76)	-0.36	0.21	0.38	-1.05		-0.12		-0.39
16	(-268.28,-64.45)	0.63	0.85	0.22	7.38	Yes			
17	(-176.34,-40.06)	-0.34	0.19	0.38	-0.97		0.16		0.27
18	(-182.69,-61.92)	-0.20	0.19	0.39	-0.57		0.25		0.51
19	(-180.89,-79.58)	0.00	0.28	0.40	0.01		-0.06		-0.10
20	(-175.60,-96.70)	0.34	0.64	0.37	1.53		0.01		-0.26
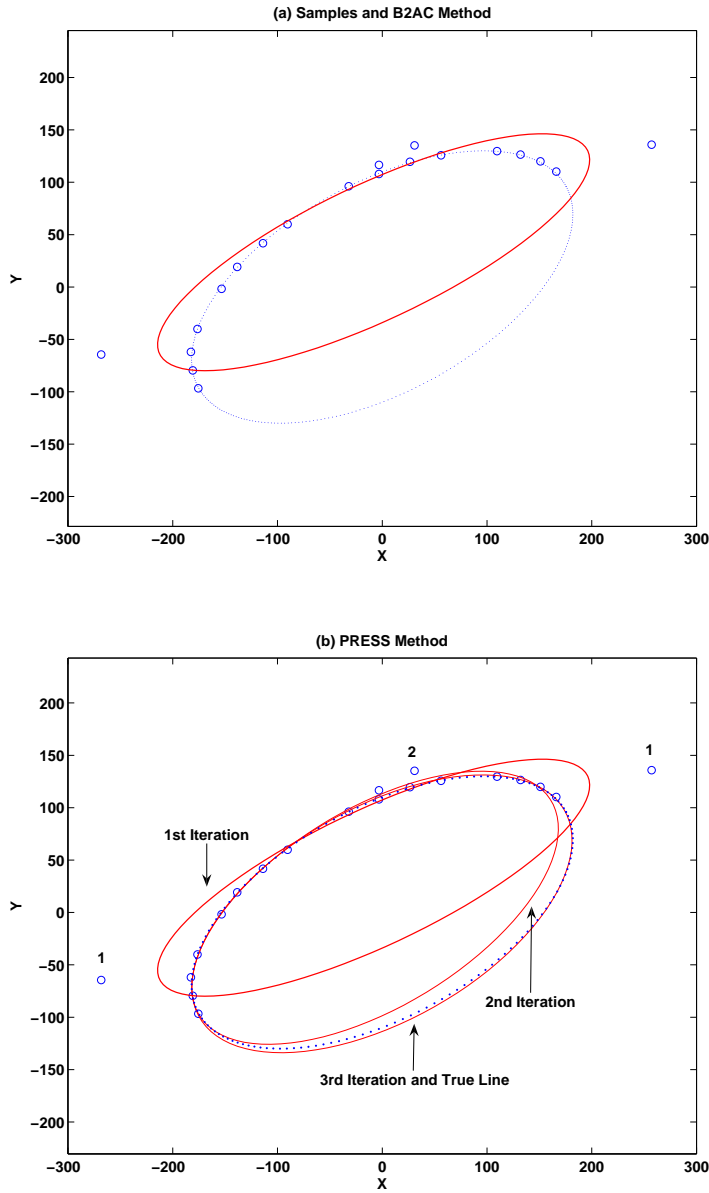
Figure 4.9: Adaptive process of the proposed fitting method: the true ellipse is represented by the dotted line, and the small circles stand for corrupted samples. (a) solid line is the result of the B2AC fitting method; (b) the adaptive process of the PRESS fitting method, the number i besides the small circles is the sequence of the sampled data being removed after i-th iteration.

70

The estimated variance of PRESS statistic t_i^j is calculated according to Equation (4.16), and the superscript j represents the iterative step. For the given samples, the estimated ellipse generated by the B2AC method:

$$[-8.23, 33.19, 226.21, 64.53, 0.44 \text{ rad}]$$

with coefficient of determination $R^2 = 0.8533$. This result was used as an initial guess for the Algorithm 4.3. A hypothesis is tested on the estimated value of the true variance σ according to Equation (4.17). For the data with 20 samples, 6 parameters and the confidence level $\alpha = 0.05$, the R-student statistic value is given as $t = 3.73$. Therefore, the data point is considered as an outlier if $t_i > 3.73$. It can be seen from Table 4.5.1 that the point 1 and 16 are removed, and the algorithm is repeated on the rest 18 data points. It gives the estimated ellipse as:

$$[-6.87, 4.48, 196.71, 94.42, 0.55 \text{ rad}]$$

For the data with 18 samples, 6 parameters and the confidence level $\alpha = 0.05$, the R-student statistic value is given as $t = 3.83$. Therefore, the data point 6 is eliminated. And the 3-rd iteration gives

$$[-0.27, -1.28, 101.90, 200.30, 0.51 \text{ rad}]$$

with $R^2 = 0.9983$. The adaptive process is also shown in Figure 4.9, where the true ellipse is represented by the dotted line, and the small circles stand for corrupted samples. The solid line in Figure 4.9(a) is the result of the B2AC fitting method; and the PRESS fitting method is illustrated in Figure 4.9(b), where the number i besides the small circles is the sequence of the sampled data being removed after i-th iteration. It can be seen the PRESS method converges nicely to an optimal solution.
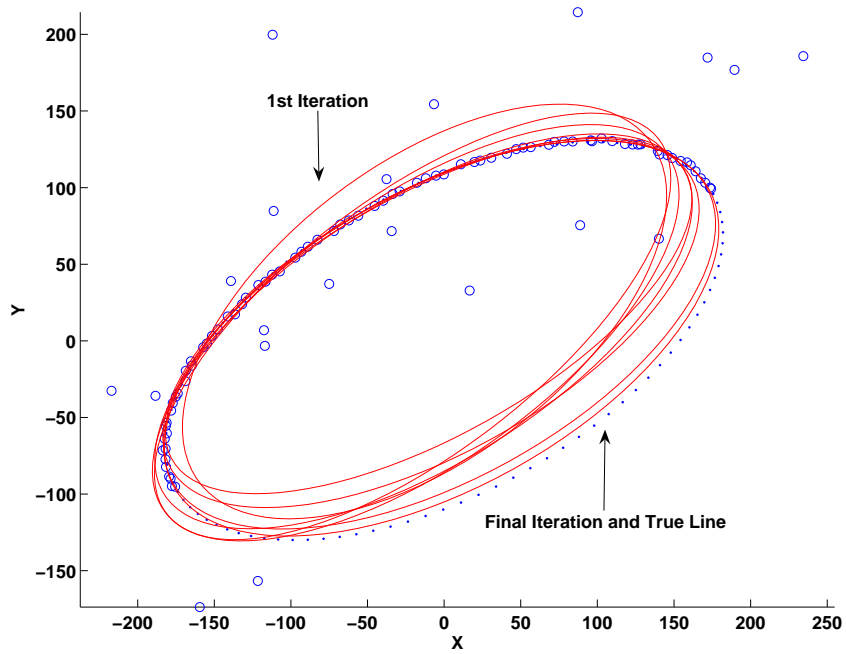
Figure 4.10: Adaptive process of the PRESS method with 100 sample points.

In order to see the evolution of the elliptic parameters along with iterative steps, another experiment is conducted as same as Experiment 4.4 except that the sample contains 100 points. The points are corrupted by zero mean Gaussian noise and 20% are turned into outliers. The adaptive process of the PRESS method are plotted in Figure (4.10). Evolution of the residual sum of squares and elliptic parameters along with iterative steps are also illustrated in Figure (4.11). It can be seen that the residual sum of squares R_{ss} are constantly being minimized at each step; while the change of the absolute error for elliptic parameters are irregular at the beginning, but they all converge to optimal values at the last couples of steps.

It can be seen qualitatively that the PRESS method has a better performance than B2AC. Its accuracy shall be extensively examined under different conditions, including:

1. level of outliers in the original data;

2. level of occlusion in the elliptic pattern;

3. level of noises in the original data;

4.5.2 Experiment 2: accuracy vs. outlier level

Figure 4.12 shows the results of comparison of accuracy with varying outlier level. The sample is taken from the ellipse $[0, 0, 200, 100, 0.5 \text{ rad}]$ with $N = 100$ points uniformly spaced around the circumference from $\theta = 0^o$ to 360° with respect to its major axis (i.e., no occlusion). The zero mean Gaussian noise is assumed as same as Algorithm 4.3 with variance $\sigma^2 = 0.01 * r_y = 1$, while the outlier level is varying
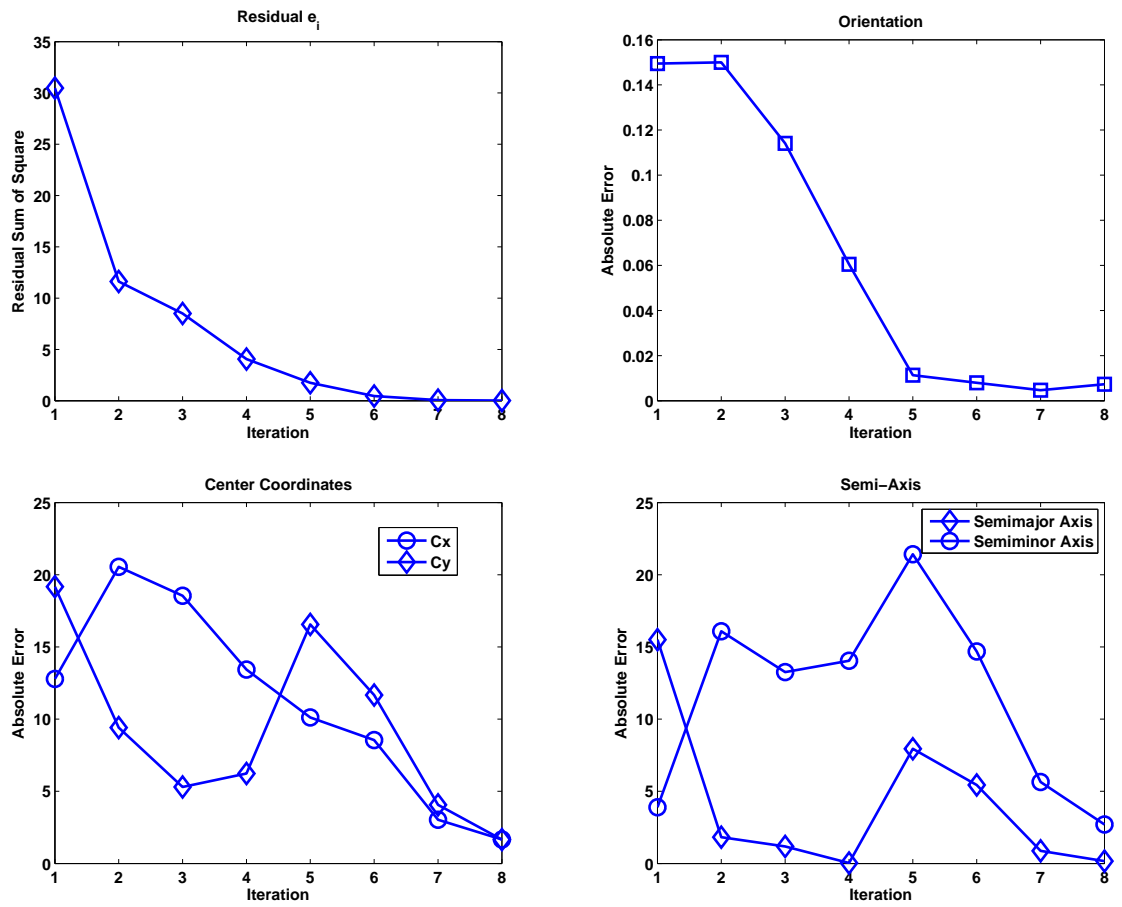
Figure 4.11: Evolution of the residual sum of squares and elliptic parameters along with iterative steps.

from 0% to 50% of the points (from 0 to 50 points in this case), and amplitude of the outlier is still a uniform deviate in $[-r_y, r_y]$. The elliptic parameters are taken by averaging 500 independent runs. Since the residual sum of square R_{ss} is a measure of how well a model fits a data set, it can be seen from the figure that the accuracy of the PRESS method always outperforms that of B2AC method.

Superaccuracy is attained by PRESS when the outlier level is less than 25%, where $R_{ss} \approx 0.1$ for 100 points. As the outlier level goes over 30%, R_{ss} increases and the accuracy of PRESS decreases closer to that of B2AC. The elliptic parameters also manifest the results as shown in Figure 4.12, where the absolute error of the PRESS method is very small at outlier level less than 25%.

The accuracy of the PRESS method outperforms that of B2AC at varying noise level σ. The comparative results are similar and hence omitted.

4.5.3 Experiment 3: accuracy vs. occlusion level

Figure 4.13 shows the performance of B2AC and PRESS at different occlusion level. The sample is taken from the ellipse $[0, 0, 200, 100, 0.5 \text{ rad}]$ with $N = 100$ points uniformly spaced around the circumference with $\theta = 360^o, 270^o, 180^o$ and 90° (i.e., 0, 1/4, 1/2 and 3/4 occluded) respectively. The zero mean Gaussian noise is assumed as same as Algorithm 4.3 with variance $\sigma^2 = 0.001 * r_y = 0.1$, while the outlier level is taken at 10% of the points (10 points in this case), and amplitude of the outlier is still a uniform deviate in $[-r_y, r_y]$. It can be seen that the PRESS method converges nicely to optimal solution. For the accuracy of both methods, the residual sum of square R_{ss} is taken by averaging 500 independent runs. It is clear from the Figure 4.14 that the accuracy of both B2AC and PRESS method decreases as the occlusion
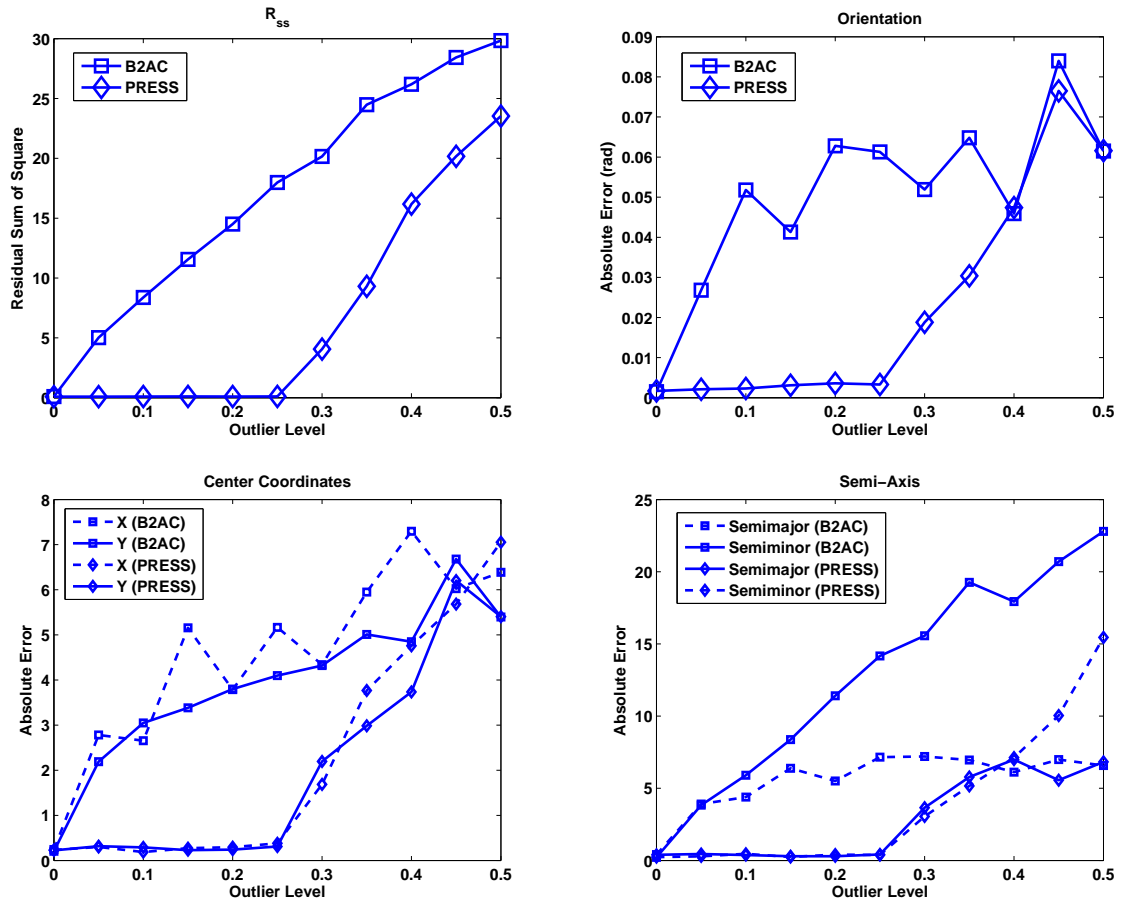
Figure 4.12: Comparison of accuracy with varying outlier level.
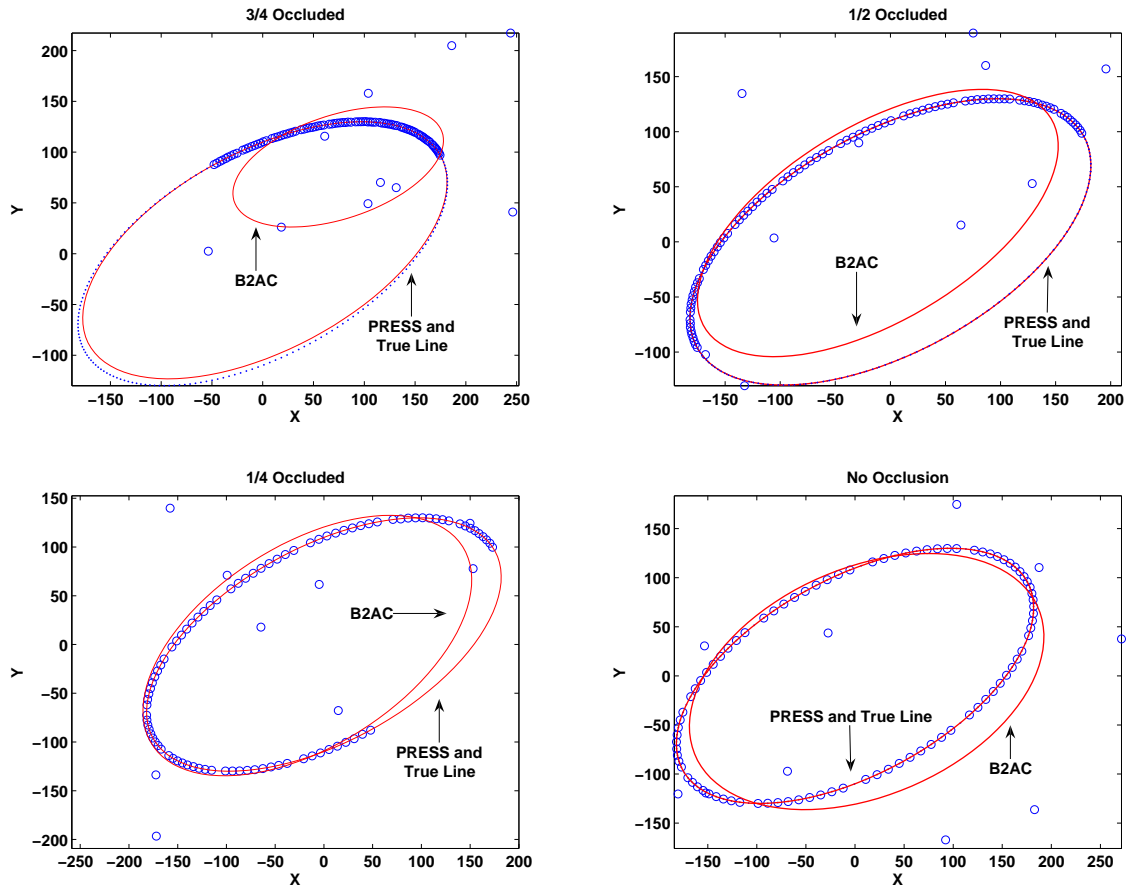
Figure 4.13: Performance of B2AC and PRESS at different occlusion level.

level increases, but the performance of PRESS always outperforms that of B2AC. The PRESS method can still achieve **superaccuracy** and find almost exactly solution to the right ellipse even if 3/4 of the ellipse is occluded and 20% of the samples are outliers.
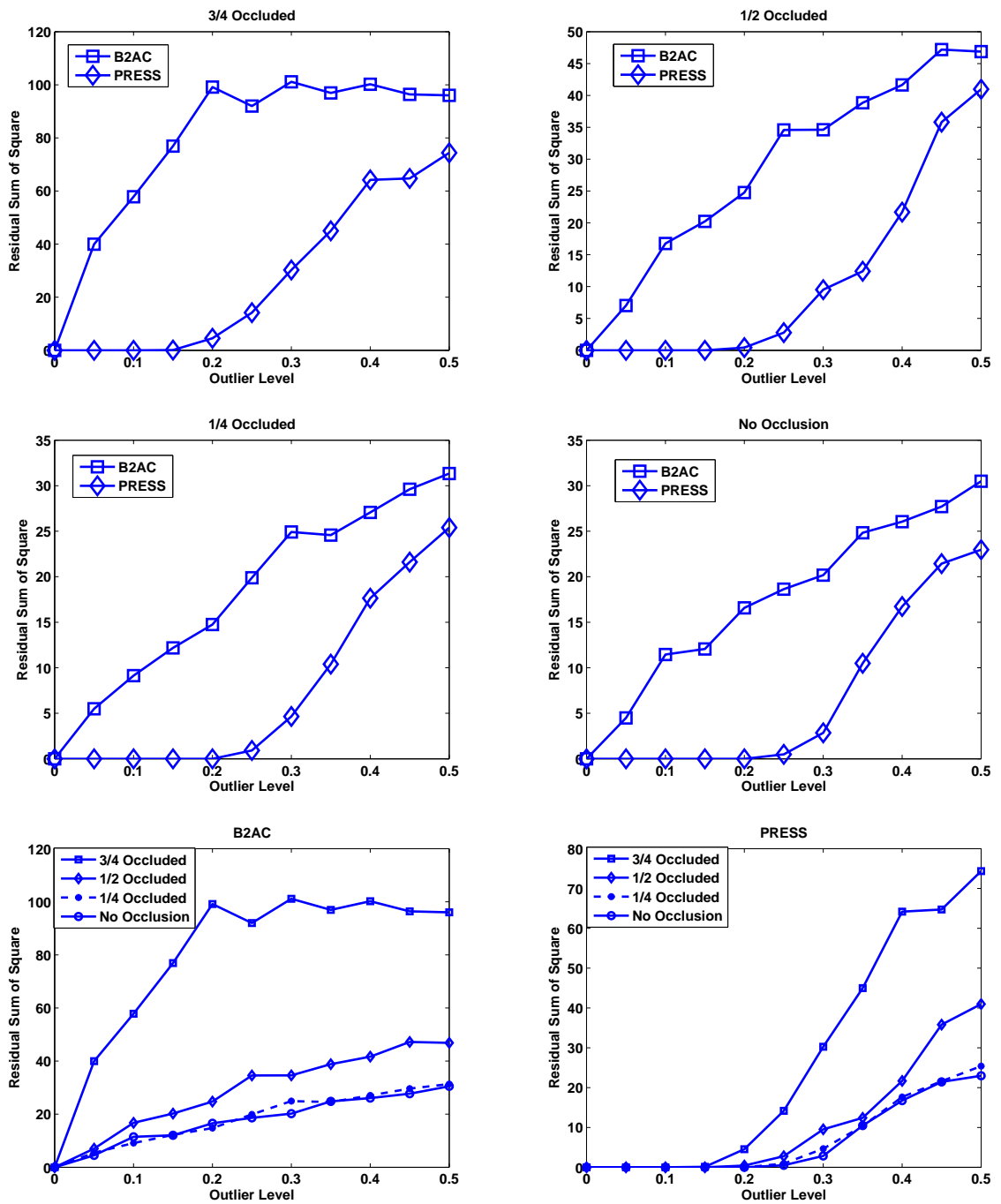
Figure 4.14: Comparison of accuracy between B2AC and PRESS at different occlusion level.

4.5.4 Experiment 4: stability and computational cost

The superaccuracy of the Algorithm 4.3 is achieved in a way that the outliers are extruded from the whole sample according to their PRESS statistic, so there arises a natural question: when will the extrusion process stop? While it is difficult to get a closed form solution for the stability of the algorithm, the question can be analyzed qualitatively. As least square method is a voting process that the regressive model takes care of majority of the points. The outliers are usually among the minority to be eliminated from the data set. When the number of outliers increase, the variance of the whole sample usually increases too. It can be seen from Equation (4.16) that the PRESS statistic t_i for a specific point will decrease, which decreases its opportunity to be marked as an outlier. Therefore, the algorithm is always stable since

1. The outliers can not increase to over 50%. If it were over 50%, the outliers become the majority. The least square method will take care of the outliers since they are majority. Of course the accuracy of the fitted model will decrease considerably under this circumstance. The trend can also be seen from Figure 4.12.

2. For the worst case, even though it will not happen in reality, majority points have been eliminated from the data set. The minimum points left can not be less than 5. Since an ellipse has 5 parameters (in polar form as in Equation (4.5.1), or 6 parameter in Cartesian form Equation (4.18)), it needs 5 points to get an exactly solution without any regression. That is to say that the 5-point model is error-free, and there will not exist any outlier. From this point of view, the algorithm always converges.

The algorithm has also been tested for tens of millions of independent runs, and no instability has been found.

For the computational cost of an algorithm, the concept FLOP will be used [105]. A flop is defined as a single floating point operation, such as a multiplication or addition, which provides a complexity measure that is independent of the hardware and operating system. For a B2AC method with N sample points, it requires $26N$ FLOPs to form the scatter matrix and additional 5182 FLOPs to perform the matrix inversion and solve the eigenvector problem [53]. The total is $26N + 5182$ FLOPs. A recent study has developed a fast method (CHORD) that can solve the elliptic problem in $13N + 109$ FLOPs [48].

When a sample contains $6,500$ points with $1,300$ outliers (20%), it may become a daunting task to distinguish these outliers at first glance. However, the PRESS method converges very fast. Table 4.5.4 shows the average iterative steps with different sample size and outlier levels. The sample is taken from the ellipse $[0, 0, 200, 100, 0.5$ rad$]$ and is uniformly spaced around the circumference with $\theta = 360^o$. The zero mean Gaussian noise is assumed to be $\sigma^2 = 0.01 * r_y = 1$, while the outlier level is taken at 10% and 20% of the points, and amplitude of the outlier is a uniform deviate in $[-r_y, r_y]$. The iterative steps are taken as an average of 500 independent runs. It can be seen that the convergence steps increase as the outlier levels and the data points increase. As the outliers are removed from a data set, the FLOPs required after each iteration will decrease. The algorithm can work alone or be combined with other methods. The average FLOPs for the PRESS method may be estimated as $n(26N + 5182)$ if working with B2AC method, or $n(13N + 109)$ if working with CHORD method, where n is the average value from Table 4.5.4.

Table 4.2: Average iterative steps with different sample size and outlier levels.

No. of	Iterations		No. of	Iterations	
Points	10% Outliers	20% Outliers	Points	10% Outliers	20% Outliers
6500	6.71	10.22	400	5.04	8.34
4000	6.54	9.78	250	4.88	8.09
2500	6.10	9.65	150	4.34	7.25
1500	5.83	9.38	100	3.86	6.74
1000	5.55	9.14	50	3.05	5.43
650	5.38	8.68	20	2.34	2.71

4.5.5 Experiment 5: real data

The proposed method is also tested on real image data. Figure 4.16 shows the experimental results of curve fitting on two die inserts: one contains straight lines and another has one ellipse. On both cases, there are small amount of outliers coming from the edge detection. The proposed method can detect the shapes more robustly.

4.5.6 Experiment 6: applications to casting dies

The purpose of this experiment is to acquire 2–D temperature signals from the surface of a die insert with varying flow rate. Analysis of the experimental data generates an understanding of the effect of internal cooling process on the averaged temperature of the die surface. The equipment and hardware used have been described in Chapter
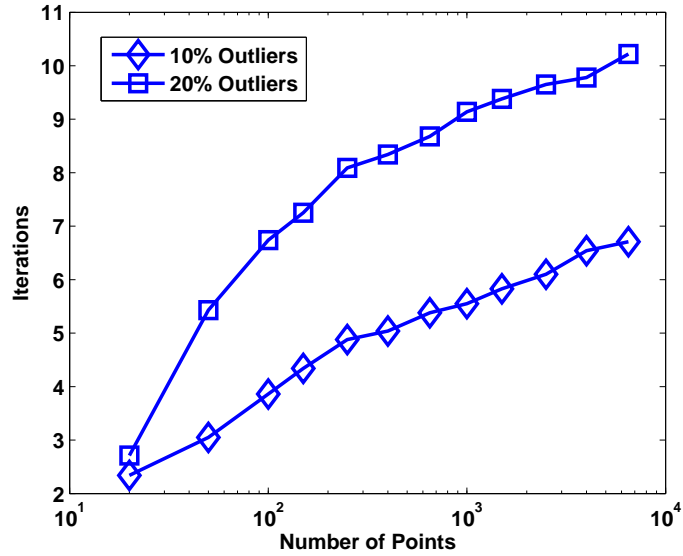
Figure 4.15: Average iterative steps at different number of points and occlusion levels.

2. The experimental procedures are summarized as follows.

Experiment Procedures 4.5. *Effect of cooling water flow rates on the averaged surface temperature of Channel 1.*

1. *Heat the die insert Channel 1 to 480^oC in the furnace;*

2. *Pull out the insert using the electric machine;*

3. *Turn on water supply to chill the insert with water flow rate to 2.65 L/min (liter per minute, or 0.7 Gallon per minute (GPM))), 3.79 L/min (1.0 GPM), 4.92L/min (1.3 GPM), 6.05 L/min (1.6 GPM), and 7.19 L/min (1.9 GPM) respectively;*

4. *At the same time when water is on, take photos on the insert surface, and record experimental data during the cooling stage for 20 seconds.*
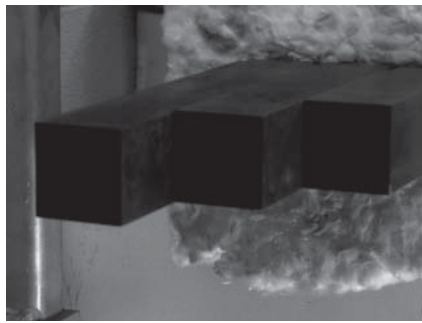
(a1) original image

(b1) original image
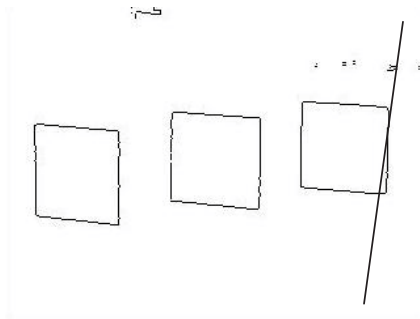
(a2) Edges and LS method (straight line)
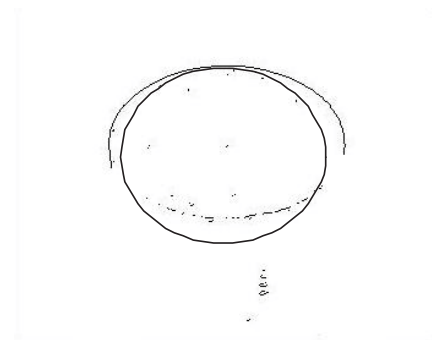
(b2) B2AC method (solid line)
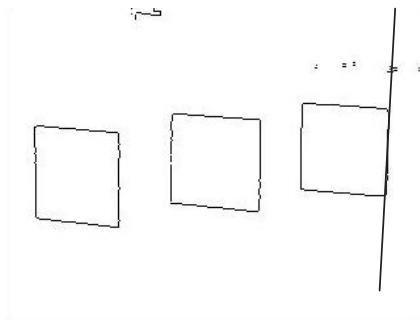
(a3) PRESS method (straight line)
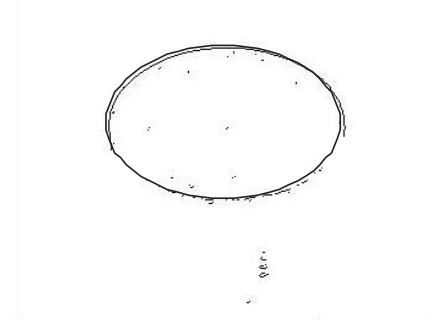
(b3) PRESS method (solid line)

Figure 4.16: Experimental results on curve fitting of two die inserts: (a) the line to be fitted on the right (only right part of the outliers are fed to the regression model); (b) ellipse fitting (the two straight lines of vertical edges are not shown).

83

(a) 0 Second   (b) 4th Second

(c) 8th Second   (d) 12nd Second

(e) 16th Second   (f) 20th Second
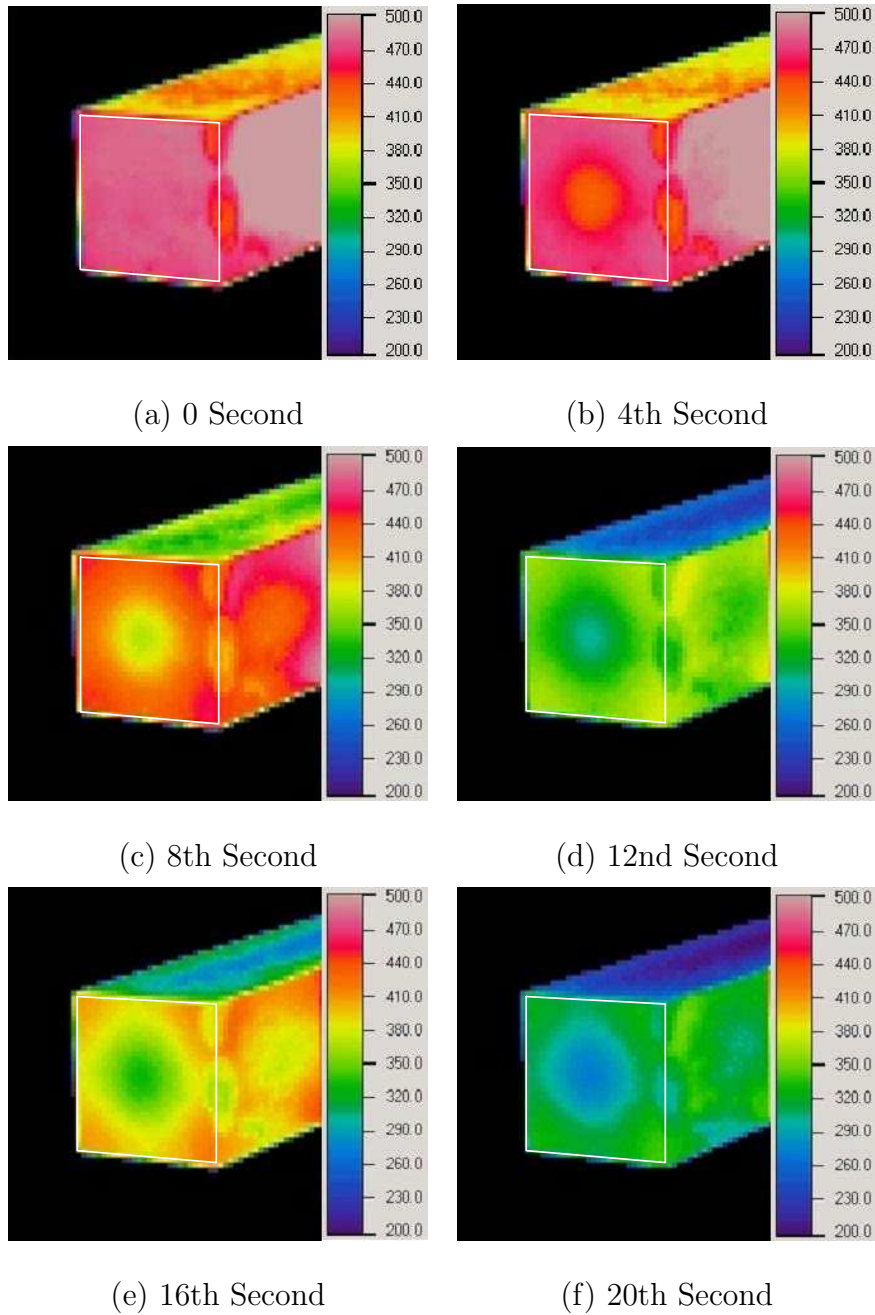
Figure 4.17: Temperature variations on the surface of Channel 1 with flow rate at 3.79L/min (color online). The white box is the shape of the surface fused from visual camera.
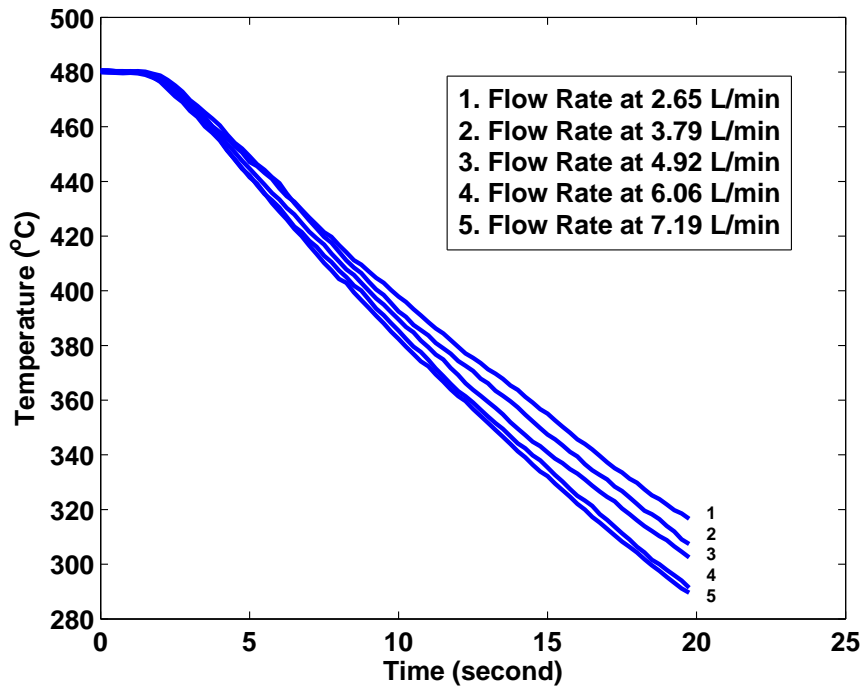
Figure 4.18: Averaged surface temperature of Channel 1 at different flow rate.

Figure 4.17 shows the temperature variations on the surface with flow rate at 3.79 L/min, where the white box is the identified circumference of the insert from the visual camera. It can be seen that the temperature drop starts from the center of the surface as the cooling waterline seats behind the center.

The experimental results are also plotted in Figure 4.18. It depicts the variation of the die insert temperature with cooling time under different water flow rates for a sampling period of 20 seconds recorded by the system with a sampling rate of 4 data per second. It can be seen from the figure that the surface temperature does not change at the first 2 seconds. It is reasonable since the bottom of cooling channel is 10 mm away from the surface as shown in Figure 2.4, and it needs time for the

heat to be diffused. The experimental data also show that the surface temperatures decrease rapidly after 2 seconds. An increase in the water flow rate reduces the surface temperature.

It is noted that the averaged surface temperature measured by the camera behaves quite differently with that of point based method measured by thermocouple [3, 16]. More of this will be explained in the next chapter after 3–D model.

4.6 Summary

This chapter proposed an adaptive curve fitting technique that can achieve robust results when the sampled data set containing certain amount of outliers. The method has been tested and compared with other techniques. Superaccuracy of curve fitting can be achieved under certain conditions. It is also applied to find optimal curves for casting dies in visual images. Finally, a 2D temperature measurement system is used to study the effect of cooling water flow rate on the averaged temperature of an insert surface.

Chapter 5

Three–Dimensional Temperature Measurement

In this chapter, computer vision techniques are applied to reconstruct a three- dimensional (3-D) thermal model of casting dies from two visual cameras and one infrared camera. Some new observations are reported on the die surface during cooling process. First a perspective camera model is introduced, then procedures of camera calibration and stereo reconstruction are presented. Finally, the thermal behavior on a insert surface is examined based on the 3D thermal model.

5.1 Introduction

Computer vision as a universe sensing method has a broad application in industries, such as agriculture [63], quality inspection [64], transportation [65], medical treatment [66], autonomous vehicles [67], to name a few. Stereo vision remains as a flushing field that attract attention from many researcher [68].

Camera parameters must be estimated for a stero vision system. Generally speaking, 3D information can be inferred from both calibrated and uncalibrated camera.

To reduce the computational cost , camera calibration is an effective way to achieve better performance in real-time applications. While there are lots of algorithms, the direct parameter calibration [69] is the most used one in industrial applications due to simplicity.

The 3D reconstruction is based on stereo correspondence between the images from two or more cameras [70]. If cameras are calibrated first, the reconstruction can be achieved without ambiguity. If only intrinsic parameters are known, the 3D object can be recovered up to an unknown scaling factor. Further, if there are no camera information available and only some correspondence points at hand, the shape of an object or scene can only be reconstructed up to an unknown projective transformation [71, 72].

The general procedure for 3D measurement in industrial automation can be followed as: camera calibration, stereo correspondence, and 3D reconstruction. The theory on 3-D computer vision used in this chapter are mainly from [36, 73].

5.2   Camera Calibration

Generally speaking, there are two most commonly used camera models: one is the perspective model which assumes the aperture of a camera lens decreases to zero, therefore all rays go through the optical center; another is the weak-perspective model which turns the mapping between camera frame and image plane into a linear one by assuming that the average depth of the scene is much smaller than the average distance between any two scene points along the optical axis. The former model is adopted in the section.
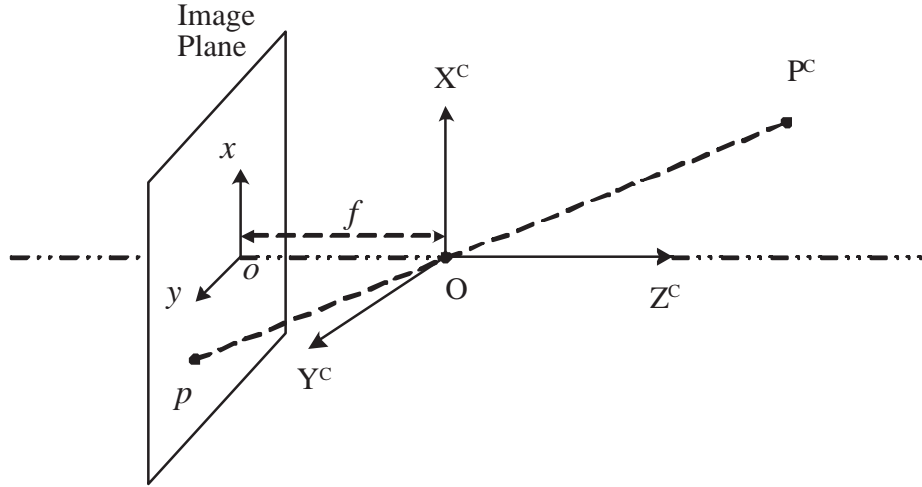
Figure 5.1: The perspective camera model.

Figure 5.1 shows the perspective camera model that consists of an image plane with coordinates $[x, y] \in \mathbb{R}^2$ and o the image center; a reference coordinates $[X^C, Y^C, Z^C] \in \mathbb{R}^3$ attached to the camera frame with a projection center $\mathbf{O}$; and the distance between o and O also called focal length $f \in \mathbb{R}$. Consider a 3D point $P^C(X^C, Y^C, Z^C)$ in camera reference coordinates and its image $p(x, y)$ in image plane, it can be written from the two similar triangles:

$$x = -f\frac{X^C}{Z^C}, \quad y = -f\frac{Y^C}{Z^C} \tag{5.1}$$

The above equations simply define a mapping

$$\pi : \mathbb{R}^3 \to \mathbb{R}^2; \quad P^C \mapsto p.$$

It is clear that the mapping loses one degree of freedom. In order to recover the original point P^C from it image p, additional images and/or sensors are needed. The image coordinates have negative sign to make p appear to be upside down. For computational convenience, it can be corrected by simply moving the image plane

89
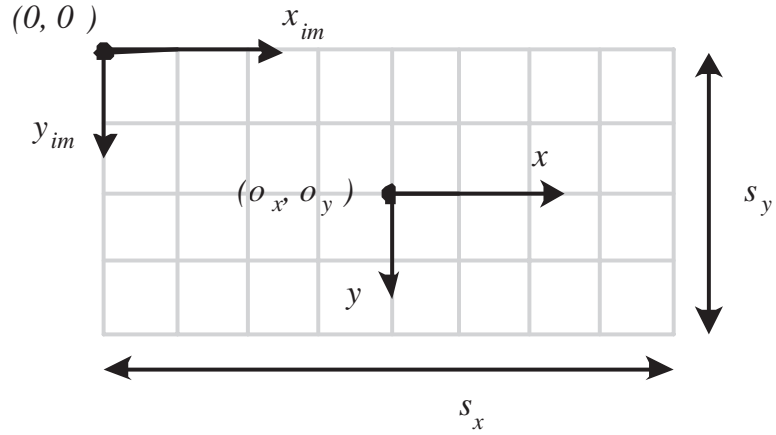
Figure 5.2: Coordinate transformation from metric to pixel.

to the position between O and P^C to generate the so-called frontal pinhole camera model.

Since images are usually expressed in pixels instead of metric unit as shown in Figure 4.3, coordinate transformation has to be carried out to transform the image point $p(x, y)$ into its pixel counterpart $p_{im}(x_{im}, y_{im})$. The transformation is illustrated in Figure 5.2, where each grey square represents an image pixle, (o_x, o_y) is the image center expressed in pixels, and s_x, s_y are the effective size of the pixel (in millimeters) in the horizontal and vertical direction respectively. It can be shown that

$$
\begin{aligned}
x &= -(x_{im} - o_x)s_x \\
y &= -(y_{im} - o_x)s_y
\end{aligned}
\tag{5.2}
$$

Substituting Equation (5.2) into (5.1) gives

$$
\begin{aligned}
x_{im} &= -f_x \frac{X^C}{Z^C} + o_x \\
y_{im} &= -f_y \frac{Y^C}{Z^C} + o_y
\end{aligned}
\tag{5.3}
$$

where $f_x = f/s_x$ and $f_y = f/s_y$. For simplicity, the subscript of x_{im} and y_{im} will be dropped from now on and x and y will be used respectively.

90

Figure 5.3: The 3 coordinate systems: arrow means linkage between two systems.

There are three coordinate systems in computer vision, namely, image plane, camera reference frame and world coordinates. The unknown camera reference frame is created to set up a link between images and the real world as shown in Figure 5.3. Now consider the same point $P^C(X^C, Y^C, Z^C)$ in camera reference frame and its expression in world coordinate $P^W(X^W, Y^W, Z^W)$, their relation can be written under the rigid body transformation

$$
\begin{bmatrix} X^C \\ Y^C \\ Z^C \end{bmatrix} = R \begin{bmatrix} X^W \\ Y^W \\ Z^W \end{bmatrix} + T \tag{5.4}
$$

where R and T are the rotation matrix and translation vector respectively, and given by

$$
R = \begin{bmatrix} r_{11} & r_{12} & r_{13} \\ r_{21} & r_{22} & r_{23} \\ r_{31} & r_{32} & r_{33} \end{bmatrix} \in \mathbb{R}^{3 \times 3}, \quad T = \begin{bmatrix} T_x \\ T_y \\ T_z \end{bmatrix} \in \mathbb{R}^{3 \times 1}
$$

with $RR^T = \mathbf{I}$ (i.e., R is orthogonal). If it is assumed that there is no radial distortion effect on the image, the unknown parameters in above equations are classified into two categories: extrinsic parameters (R and T), and intrinsic parameters (f_x, α and (o_x, o_y)), where aspect ratio $\alpha = s_y / s_x$.

Substituting Equation (5.1) into (5.4) generates

$$
x - o_x = -f_x \frac{r_{11}X^W + r_{12}Y^W + r_{13}Z^W + T_x}{r_{31}X^W + r_{32}Y^W + r_{33}Z^W + T_x} \tag{5.5}
$$

$$
y - o_y = -f_y \frac{r_{21}X^W + r_{22}Y^W + r_{23}Z^W + T_y}{r_{31}X^W + r_{32}Y^W + r_{33}Z^W + T_x} \tag{5.6}
$$

91

The above two equations can also be written in matrix form in a so-called homogeneous coordinates:

$$
\begin{pmatrix} x_1 \\ x_2 \\ x_3 \end{pmatrix} = M_{int} M_{ext} \begin{pmatrix} X^W \\ Y^W \\ Z^W \\ 1 \end{pmatrix}
\tag{5.7}
$$

where $x_1/x_3 = x$ and $x_2/x_3 = y$; M_{int} and M_{ext} are called intrinsic and extrinsic matrix respectively and are given by

$$
M_{int} = \begin{pmatrix} -f_x & o & o_x \\ 0 & -f_y & o_y \\ 0 & 0 & 1 \end{pmatrix} \in \mathbb{R}^{3\times3}
$$

and

$$
M_{ext} = \begin{pmatrix} r_{11} & r_{11} & r_{11} & T_x \\ r_{21} & r_{22} & r_{23} & T_y \\ r_{31} & r_{32} & r_{33} & T_z \end{pmatrix} \in \mathbb{R}^{3\times4}
$$

Further, from Equations (5.5) and (5.6), it is easy to show

$$
(x - o_x) f_y (r_{21} X^W + r_{22} Y^W + r_{23} Z^W + T_y) = (y - o_y) f_x (r_{11} X^W + r_{12} Y^W + r_{13} Z^W + T_x)
\tag{5.8}
$$

$$
(x - o_x)(r_{31} X^W + r_{32} Y^W + r_{33} Z^W + T_z) = -f_x (r_{11} X^W + r_{12} Y^W + r_{13} Z^W + T_x) \tag{5.9}
$$

These are direct link from image plane to the real world coordinates without the inaccessible camera reference frame. The unknown intrinsic and extrinsic parameters can be solved if a sufficient number of points can be found on a known calibration pattern. There are two steps to estimate the parameters.

Step 1: assume $(o_x, o_y) = (0, 0)$ and estimate other parameters:

From Equation (5.8), if n corresponding pairs of points $((X_i^W, Y_i^W, Z_i^W), (x_i, y_i))$ with $i = 1, 2, \cdots, n$ are identified from real world coordinates and image plane, the calibration problem turns to solve a homogeneous system with n linera equations

$$
\mathbf{Av} = \mathbf{0}
\tag{5.10}
$$

where

$$\mathbf{A} = \begin{bmatrix} x_1 X_1^W & x_1 Y_1^W & x_1 Z_1^W & x_1 & -y_1 X_1^W & -y_1 Y_1^W & -y_1 Z_1^W & -y_1 \\ x_2 X_2^W & x_2 Y_2^W & x_2 Z_2^W & x_2 & -y_2 X_2^W & -y_2 Y_2^W & -y_2 Z_2^W & -y_2 \\ \vdots & \vdots & \vdots & \vdots & \vdots & \vdots & \vdots & \vdots \\ x_n X_n^W & x_n Y_n^W & x_n Z_n^W & x_n & -y_n X_n^W & -y_n Y_n^W & -y_n Z_n^W & -y_n \end{bmatrix} \in \mathbb{R}^{n \times 8}$$

$$\mathbf{v} = (r_{21}, r_{22}, r_{23}, T_y, \alpha r_{11}, \alpha r_{12}, \alpha r_{13}, \alpha T_x) \in \mathbb{R}^{1 \times 8}$$

Once again, it is a singular value decomposition (SVD) problem of $\mathbf{A} = UDV^T$. $\hat{\mathbf{v}}$, the solution of $\mathbf{v}$ up to an unknown scale factor, is the column of V corresponding to the smallest singular value along the diagonal of D [107]. Let

$$\hat{\mathbf{v}} = (\hat{v}_1, \hat{v}_2, \hat{v}_3, \hat{v}_4, \hat{v}_5, \hat{v}_6, \hat{v}_7, \hat{v}_8)$$

and the unknown factor be γ, then

$$\mathbf{v} = \gamma \hat{\mathbf{v}}$$

From the fact that $RR^T = \mathbf{I}$, it gives

$$\sqrt{\hat{v}_1^2 + \hat{v}_2^2 + \hat{v}_3^2} = \sqrt{\gamma^2(r_{21}^2 + r_{22}^2 r_{23}^2)} = |\gamma| \tag{5.11}$$

$$\sqrt{\hat{v}_5^2 + \hat{v}_6^2 + \hat{v}_7^2} = \sqrt{\gamma^2 \alpha^2 (r_{11}^2 + r_{12}^2 r_{13}^2)} = \alpha|\gamma| \tag{5.12}$$

Then α and $|\gamma|$ can be determined from the above two equations. Recall that for every point $Z^C > 0$, as expressed in Equation (5.5), x and $(r_{11}X^W + r_{12}Y^W + r_{13}Z^W + T_x)$ must have opposite sign. Therefore, the sign of γ is determined to ensure that

$$x(r_{11}X^W + r_{12}Y^W + r_{13}Z^W + T_x) < 0 \tag{5.13}$$

Next the parameters T_x and f_x are to be determined. Similarly, according to Equation 5.9 for n corresponding pairs of points, it gives

$$\mathbf{B} \begin{pmatrix} T_z \\ f_x \end{pmatrix} = \mathbf{b}$$

93

where

$$\mathbf{B} = \begin{bmatrix} x_1, & (r_{11}X_1^W + r_{12}Y_1^W + r_{13}Z_1^W + T_x) \\ x_2, & (r_{11}X_2^W + r_{12}Y_2^W + r_{13}Z_2^W + T_x) \\ \vdots, & \vdots \\ x_n, & (r_{11}X_n^W + r_{12}Y_n^W + r_{13}Z_n^W + T_x) \end{bmatrix} \in \mathbb{R}^{n \times 2}$$

and

$$\mathbf{b} = \begin{bmatrix} -x_1(r_{31}X_1^W + r_{32}Y_1^W + r_{33}Z_1^W + T_x) \\ -x_2(r_{31}X_2^W + r_{32}Y_2^W + r_{33}Z_2^W + T_x) \\ \vdots \\ x_n(r_{31}X_n^W + r_{32}Y_1^W + r_{33}Z_n^W + T_x) \end{bmatrix} \in \mathbb{R}^{n \times 1}$$

Using the least square method, the two parameters can be found as

$$\begin{pmatrix} T_z \\ f_x \end{pmatrix} = (\mathbf{B}^\mathbf{T}\mathbf{B})^{-1}\mathbf{B}^\mathbf{T}\mathbf{b} \tag{5.14}$$

Step 2: estimate (o_x, o_y):

The estimation of the image center is relatively simple. In perspective projection, straight line in $\mathbb{R}^3$ is projected onto a straight line in the image plane. However, the projection of two parallel lines intersect in the image plane. The concept of vanishing point will be used to estimate the image center (o_x, o_y). A vanishing point is defined as the common intersection of all the image lines taken from several parallel lines in $\mathbb{R}^3$. For a triangle Δ formed on the image plane by three vanishing points of three mutually orthogonal sets of parallel lines in $\mathbb{R}^3$, the orthocenter of Δ is the image center.

The calibration tools for the three cameras are shown in Figure 5.4. A standard cube [36] is usually employed for visual cameras as shown in (a). While for thermal camera, a plastic board with holes 4mm apart is used as illustrated in Figure 5.4(b). It can be placed before a thermal source, and an image of the board is shown in (c). For calibration purpose, the center of each holes are located first, then Zhang's

method [74] can be applied to obtain the intrinsic and extrinsic parameters of the thermal camera.

Algorithm 5.1. *Camera calibration for two visual cameras [36, 73].*

1. *Measure the world coordinates of the vertex of the calibration squares;*

2. *Use edge, corner or line detectors to locate the image lines the squares;*

3. *Compute three vanishing points and find the orthocenter of the three points. The orthocenter is also the image center;*

4. *Use pairs of corresponding points to calculate the SVD in Equation (5.10), and find its vector associated with the smallest singular value to determine part of rotation matrix R and translation vector T;*

5. *Determine α, γ and its sign from Equations (5.11),(5.12),(5.13);*

6. *Solve Equation (5.14) and hence find the rest part of the R and T.* ◇

5.3   Epipolar Geometry

The epipolar geometry plays an important role in 3-D computer vision. As shown in Figure 5.5, there are two perspective cameras 1 and 2 with projection center O_1 and O_2 respectively. Vectors P_1 and P_2 are the same point in different coordinates with respect to camera 1 and 2, and vectors p_1 and p_2 are projections of the point P on camera 1 and 2 respectively. All the coordinates are in their respective camera reference frame. The line through (O_1, O_2) intersects the image plane 1 and 2 (or its extension) respectively at point e_1 and e_2 that are called epipoles. The plane

(a) a standard calibration cube for visual cameras
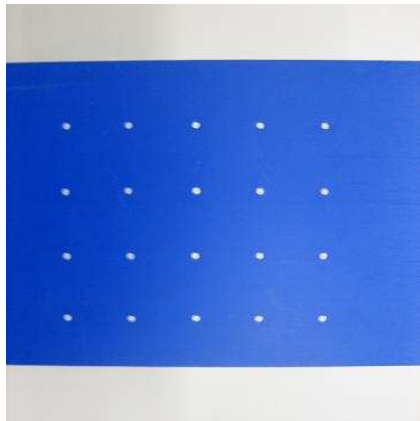
(b) a plastic board with holes for thermal camera
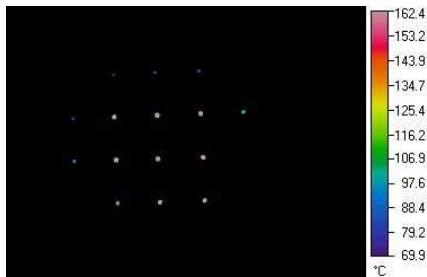
(c) thermal image of the plastic board

Figure 5.4: Calibration tools for three cameras (color online).
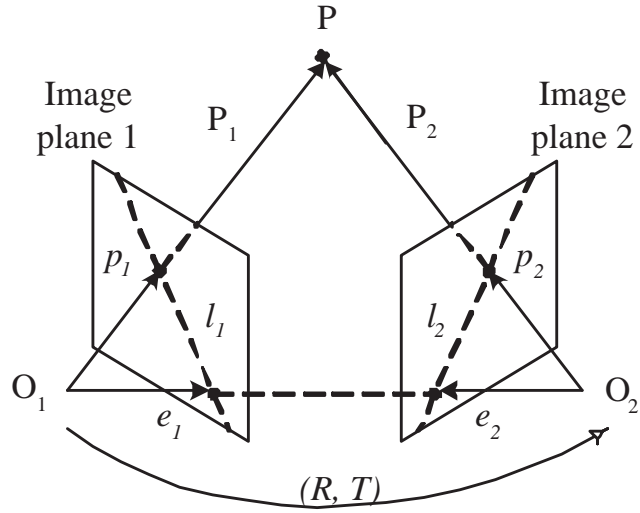
Figure 5.5: The epipolar geometry:

determined by (O_1, O_2, P) is called epipolar plane. The epipolar lines l_1 and l_2 are the intersections of epipolar plane with image plane 1 and 2 respectively.

From rigid body transformation, the two camera reference frames are linked through a rotation matrix $R \in \mathbb{R}^{3\times3}$, and a translation vector $T = (O_2 - O_1) \in \mathbb{R}^{3\times1}$. Therefore,

$$P_2 = R(P_1 - T) \tag{5.15}$$

Given p_1, from image plane 1's perspective, the real point P could be anywhere on the ray from O_1 to p_1. However, the image of of this ray is the epipolar line in the image plane 2. Therefore, p_2, the correspondence point of p_1 must lie on the epipolar line. As a result, searching for correspondence point can be conducted only on a 1-D line, which greatly improve the computational efficiency of the 3-D reconstruction. It is noted that only one epipolar line passes through any image point and all the epipolar lines of one camera must go through its epipole.

The epipolar plane can be written in a cross product form:

$$
\begin{aligned}
0 &= (P_1 - T)^T T \times P_2 \\
&= P_2^T RT \times P_2 \text{ (substitute 5.15)} \\
&= P_2^T RS P_1
\end{aligned}
$$

In the last step, the fact that a vector product can be written as a multiplication by a rank-deficient matrix has been used, where

$$
S = \begin{pmatrix} 0 & -T_z & T_y \\ T_z & 0 & -T_x \\ -T_y & T_x & 0 \end{pmatrix}
$$

It is clear that S has rank 2. Let $E = RS$. Then E is called the essential matrix, the mapping between points and epipolar lines. it also directly gives

$$
p_2^T E p_1 = 0 \tag{5.16}
$$

The above equation is in camera reference frame, and has to be transformed into image frame in pixel coordinates. Let M_1 and M_2 be the intrinsic matrices from Equation 5.7 associated with camera 1 and 2 respectively, and let $\tilde{p}_1$ and $\tilde{p}_2$ be the points in pixel coordinates corresponding to p_1 and p_2, then

$$
\tilde{p}_1 = M_1 p_1, \quad \tilde{p}_2 = M_2 p_2
$$

Plugging into Equation (5.16):

$$
\tilde{p}_2^T F \tilde{p}_1 = 0 \tag{5.17}
$$

where $F = M_2^{-T} E M_1^{-1}$ is called fundamental matrix.

Algorithm 5.2. *Compute essential, fundamental matrices and epipoles [36, 73].*

For n input correspondence points with $n \geq 8$

98
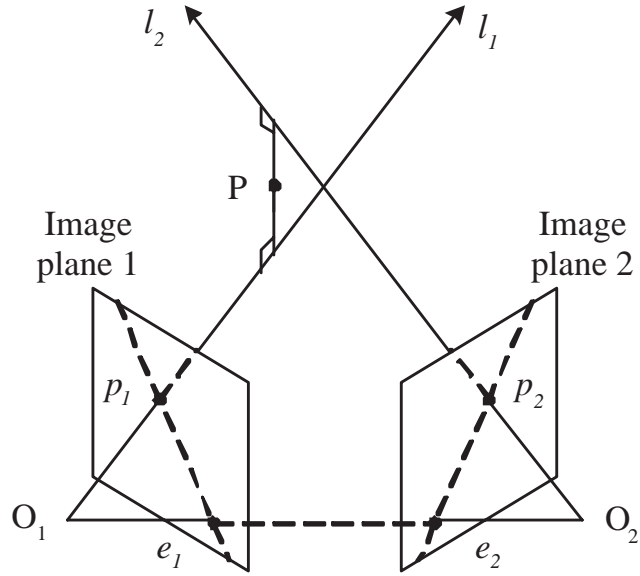
Figure 5.6: Reconstruction by triangulation.

1. *construct n linear equations according to Equation (5.17) as in the camera calibration algorithm;*

2. *calculate the SVD of the n equations. F is the column vector associated with the smallest singular value, up to an unknown signed scale factor;*

3. *compute the SVD of F: $F = UDV^T$; set the smallest singular value in D to 0 in order to ensure the singularity constraint;*

4. *the F is then given by $F = UDV^T$;*

5. *the epipole e_1 is the column vector of V associated with 0 singular value, and e_2 is the column vector of U associated with 0 singular value.*

In some applications, one pair of conjugate epipolar lines can be further transformed to be collinear and parallel to one of the image axies.
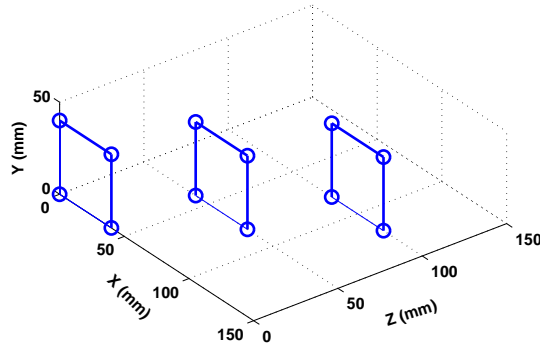
(a) image feature points shown in small circles
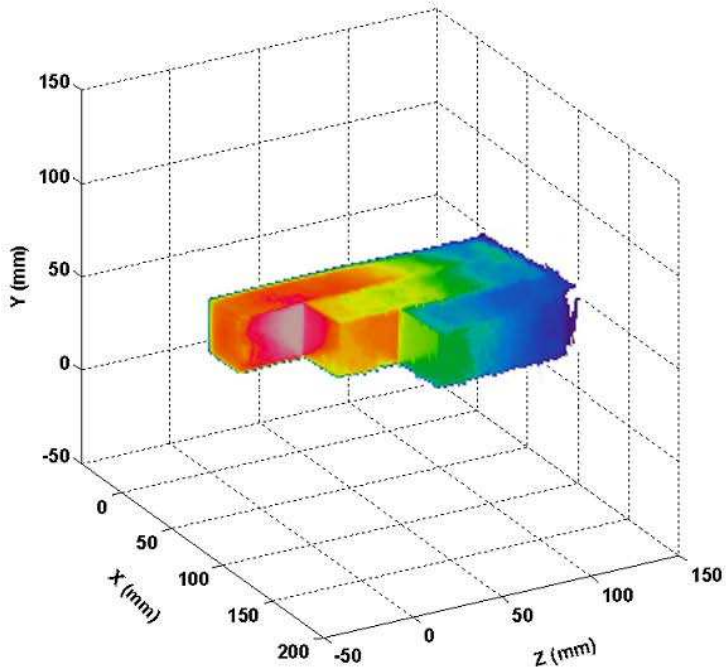
(b) reconstructed thermal image

Figure 5.7: Reconstruction by triangulation: (a) image corners are extracted first which are also the corners of inserts; (b) thermal data are then patched among these corners to form a 3D thermal image (color online).

5.4   3-D Reconstruction

If the intrinsic and extrinsic parameters of a stereo system are known, the 3-D shape of an object can be reconstructed unambiguously. Figure 5.6 shows the reconstruction by triangulation. Let R_1 and T_1, and R_2 and T_2 be the extrinsic parameters of camera 1 and 2 with respect to the same world coordinates, and let R and T be the extrinsic parameters between the two cameras as shown in Figure 5.5, then for a point P in the world coordinates, there exist

$$P_1 = R_1 P + T_1$$
$$P_2 = R_2 P + T_2$$
$$P_2 = R(P_1 - T)$$

Using P_2 as a medium, it can be solved

$$R = R_2 R_1^T, \quad T = T_1 - R^T T_2$$

In reality, the two rays (O_1, p_1) and (O_2, p_2) may not intersect in space due to computational accuracy. Under this circumstance, the reconstruction problem becomes to find the shortest line that joins l_1 and l_2, the middle point of the is the reconstructed 3-D point.

Algorithm 5.3. *Reconstruction from triangulation [36, 73]. For the conjugate image pairs p_1 and $p2$,*

1. *l_1 is represented by $a p_1$ with $a \in \mathbb{R}$, and l_2 is represented by $b R^T p_2 + T$ with $b \in \mathbb{R}$;*

2. Solve the linear equation to find the shortest line that joins l_1 and l_2:

$$ap_1 - (bR^Tp_2 + T) + c(p_1 \times R^Tp_2) = 0;$$

3. find the midpoint of the line.

The output is a set of reconstructed 3-D points

5.5 Experimental Results

In this application, the 3D thermal image reconstruction follow two main steps :

1. extract feature points from two visual cameras. The most important image feature in this application is the image corners, which are also coincident to be the corners of the die inserts. The world coordinates of these corners are calculated based on the camera calibration information;

2. patch thermal data. Since the correspondence has already been built between one visual image and the thermal image, the thermal data can then be patched to among the corners to form the 3D image. As the surface of the insert is planar, projective transformation can be used.

The experimental results of reconstruction is shown is Figure 5.7. 3D thermal images contain a large amount information that can be used to calculate the surface temperature distribution, heat removal rate on the surface, and etc. These information are only partially available in 2D images, hence can not used for accurate computation.
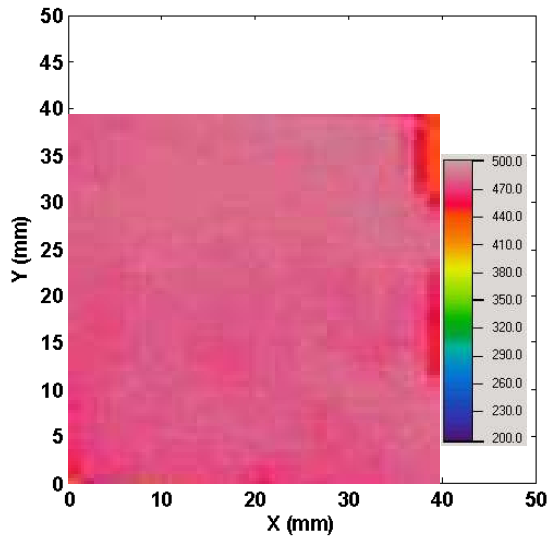
(a) at 0 second
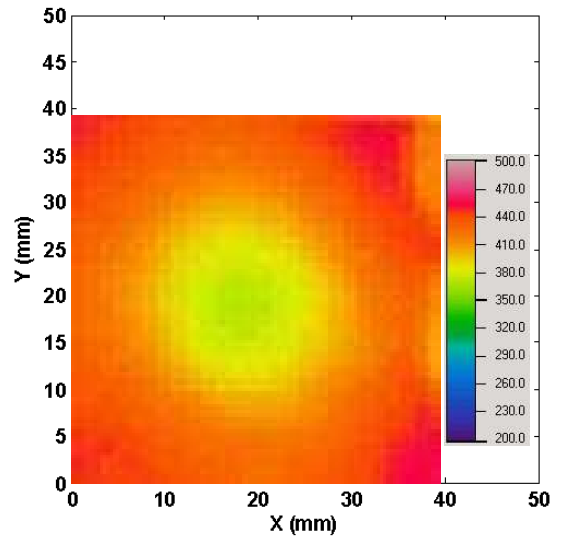
(b) at 8th second
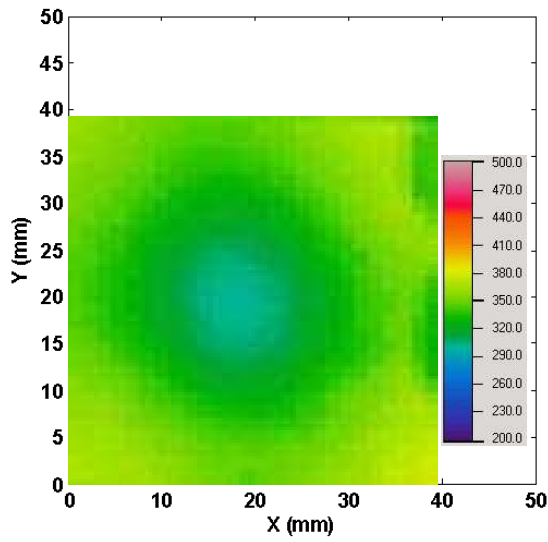
(c) at 16th second
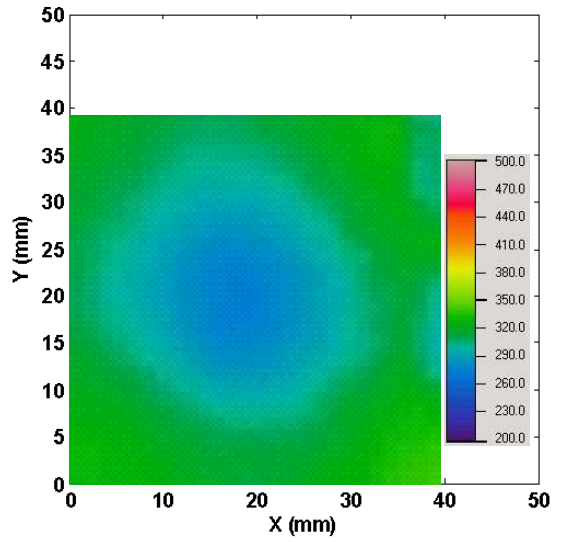
(d) at 20th second

Figure 5.8: Rectified thermal images of Channel 1 at flow rate 3.79 L/min (color online).

103

5.5.1 Temperature distribution on insert surface

In projective geometry, the straight lines in real world are mapped to straight lines in image plane, but a pair of parallel lines tend to intersect at the vanishing point. Therefore, the shape of a rectangle in real world may not be kept in image plane. It is clear from the previous chapter that the square surface of the die insert is distorted in a 2D thermal image and is no longer a square. However, the geometric information is directly accessible from the 3D thermal image. Therefore, the thermal behavior on the die surface should be re-examined after 3D reconstruction.

The rectified images of Channel 1 are shown in Figure 5.8 at $0, 8, 16, 20$ seconds respectively with cooling water flow rate at 3.75 L/min. It can be seen that the measured surface is approximately $40mm \times 40mm$ square close to the real one.

The Cooling induced temperature inhomogeneity on the surface of Channel 1 is plotted in Figure 5.9 at flow rate 3.79 L/min. The area of the surface to be plotted is $30mm \times 30mm$ square centered on the whole insert surface. It can be seen from the figure that the temperature distribution is more homogeneous at 0 second when cooling water is not applied. As the cooling process proceeds after 0 second, although the averaged surface temperature drops, the temperature inhomogeneity is generated and remains to the end of the sampling period. The temperature difference are listed in Table 5.1.

5.5.2 Comparison with thermocouple

Traditionally thermocouple has been widely used in temperature monitoring in die casting industry. A thermocouple is inserted into the die insert through a hole drilled
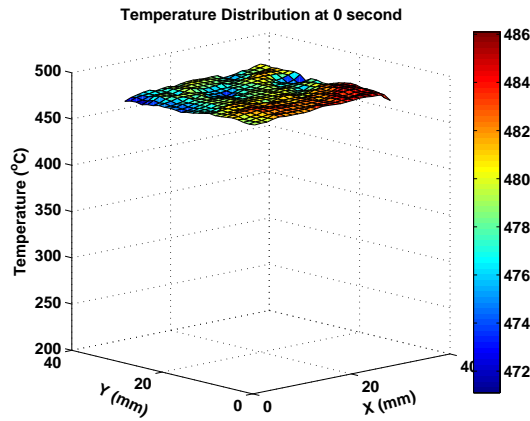
(a) at 0 second
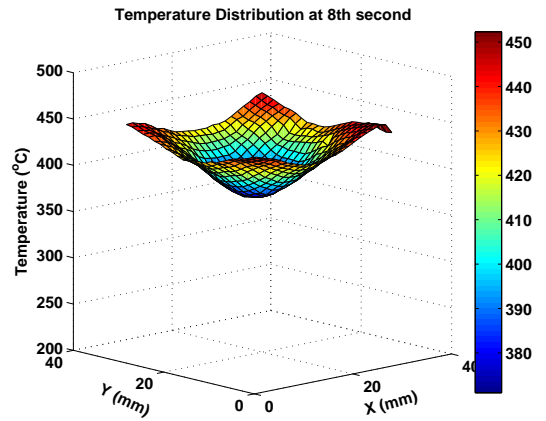
(b) at 8th second
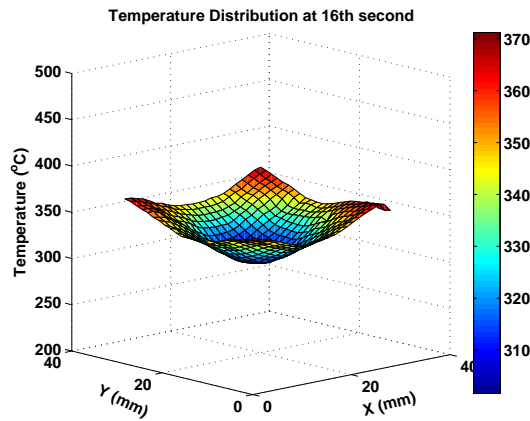
(c) at 16th second
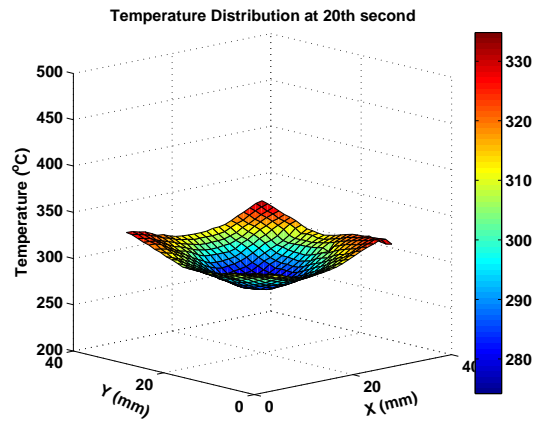
(d) at 20th second

Figure 5.9: Cooling induced temperature inhomogeneity on the surface of Channel 1 at flow rate 3.79 L/min (color online).

Table 5.1: Temperature difference (in ^{o}C) at different cooling time

Time (s)	0	8	16	20
Max Temperature	486.1	452.3	371.2	334.8
Min Temperature	471.1	371.0	301.6	274.2
Difference	15.0	81.3	69.6	60.6
Mean on Surface	479.8	415.0	336.0	303.5
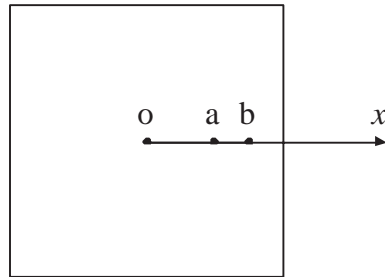
Figure 5.10: Different sensor locations.

from its back. It is also called point sensing method because temperature information can only be acquired at a specific position where the thermocouple seats. The destructive sensing method upsets the operation of die maintenance, and makes casting production costly.

As thermal imaging is a surface sensing method, it can be demonstrated that measurement accuracy of a point sensing method is very sensitive to the location of the point. Assume there are no other radiation effect, it is sufficient to pick up several points on the insert surface to see how their temperatures vary along with time.

For simplicity, two points are selected as shown in Figure 5.10, where o is the geometric center of the die insert, and the distances $oa = 10$ mm and $ob = 15$ mm. Once again, the experiment is taken on Channel 1 with flow rate at 3.79 L/min. The results are shown in Figure 5.11, where measured temperature at location a is always lower than that of location b since a is closer to the cooling channel. Therefore, the point based temperature measurement is sensitive to geometric locations, and can not be used as a direct control reference for real time thermal management system.

5.5.3   Heat flux

Conductive heat transfer occurs due to the temperature gradients in the die insert. To understand the effect of the cooling on heat transfer away from the die insert surface, the heat flux is calculated in Figure 5.10 along $x - axis$. According to Fouriers law:

$$\dot{q}_n = -k\frac{dT}{dn}$$

where $\dot{q}_n$ is the heat flux in the n-direction $(J/s/m^2)$, k stand for the die H13 thermal conductivity $(J/s/m)$, T represents the die temperature distribution along n-direction
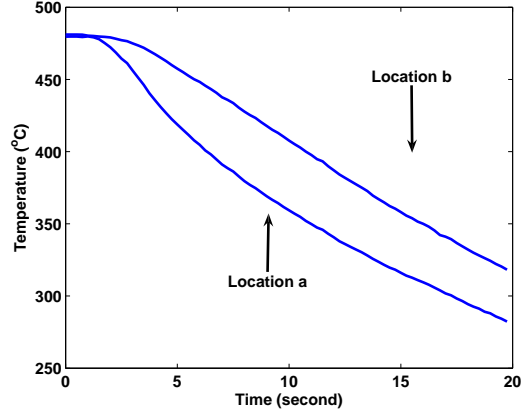
Figure 5.11: Temperature variations at two different locations .

(K), and n depicts the direction along which temperature gradient exists (m). It is reasonable to assume that there are local isothermal surfaces around locations a and b. The temperature distribution is assumed to be linear along the x-direction from o to a, and o to b respectively. Instantaneous heat flux across the isothermal location a and b in the x-direction can be estimated by using the following equation:

$$\dot{q}_a(t) = -k\frac{T_o - T_a(t)}{x_o - x_a} = -k\frac{\Delta T_{o-a}}{\Delta x}$$

where $\dot{q}_a(t)$ is the heat flux across location a at instant time t in the x-direction, $T_o(t)$ the absolute temperature at location o at instant time t, $T_a(t)$ the absolute temperature at location a at instant time t, and Δx is the distance between location o and a in the x-direction. Same equation can be established for location b.

The transient response of the die insert temperature at location o is depicted in Figure 5.12(a). The heat flux across locations a and b in x-direction is shown in Figure 5.12(b). Experimental results show that the heat flux across both locations increases rapidly after the cooling water is applied, and decreases slightly after reaching its
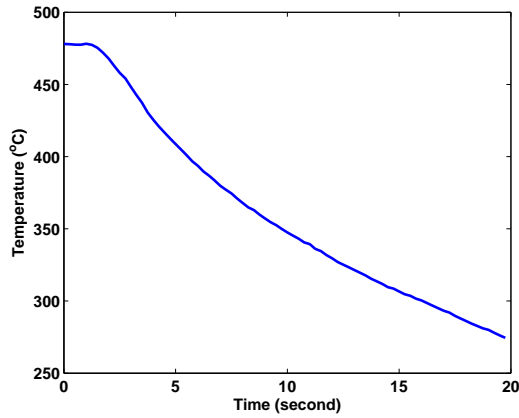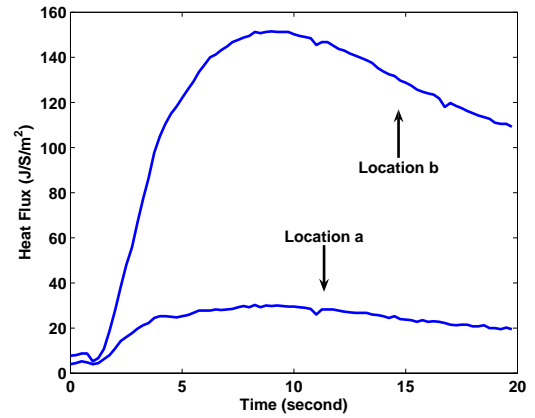
(a) Temperature at location o. (b) Heat flux.

Figure 5.12: Heat flux: (a) temperature variations at center location o; (b)heat flux across location a and b.

peak value at about the 8th second.

5.6 Summary

A 3D vision system is built to study the thermal behavior of a die insert surface. It is found that the temperature on the surface may become inhomogeneous during cooling processes. The center temperature, due to closer to the cooling channel, is usually lower than that of its surrounding neighbors. It is also shown that the point based temperature measurement is sensitive to geometric locations, and hence should be cautious when used for real time thermal control system.

Chapter 6

Robust Temperature Measurement

In this chapter, graph cuts are applied to classify the thermal pattern on the insert surface. The loss of temperature measurement due to packet loss of thermal images over a networked system can be recovered using the graph cut method. Synthesized data are used for simulation.

6.1   Introduction

Nowadays the manufacturing processes are mostly operated and coordinated through industrial communication networks, where sensing components and processing center may be in difference places. A networked sensing and control system is illustrated in Figure 6.1, where the thermal images must be encoded before they can be transmitted to the network. After the processing center gets the decoded images from the network, it may compute the temperature of the target, then send control command over the network. Since there are other traffic running over the same network, the image packets may be lost over a busy network. The loss is usually modeled as Markov chain [76]. Two typical effect caused by packet loss over network are shown

in Figure 6.2, where black areas are lost pixels. The temperature measurement may become inaccurate due to the loss, and malfunction may be caused by the inaccuracy. Furthermore, a factory is usually noisier in terms of the working environment for a camera. There may be thousands of machines running at the same time in a factory which may introduce electromagnetic interference with the camera, and hence further corrupts the performance of the vision guided control system.

In the past, lots of algorithms are proposed to recover the image loss over a network (see [80] and the reference therein). However, most of them are focused on encoder and decoder side, which may work better with motion pictures. The static scene is typical for an industrial process where there are less or no motions at all.

Graph theory has been widely used in machine vision [81]. It has been demonstrated that efficient image segmentation can be achieved by graph cuts and its derivatives [82]. Broadly speaking, the loss recovery can be simplified as a thermal pattern classification problem. The chapter proposes to use graph cuts to recover the packet loss directly from the thermal image. It is assumed that

1. Packet loss should not be over 50% of the thermal image of a target;

2. The scene is static, and the location of packet loss is known;

3. The image is encoded by square blocks.

Synthesized data are used for simulation. For convenience, the surface images of Channel 1 are used directly in this study to test the performance of proposed algorithm.
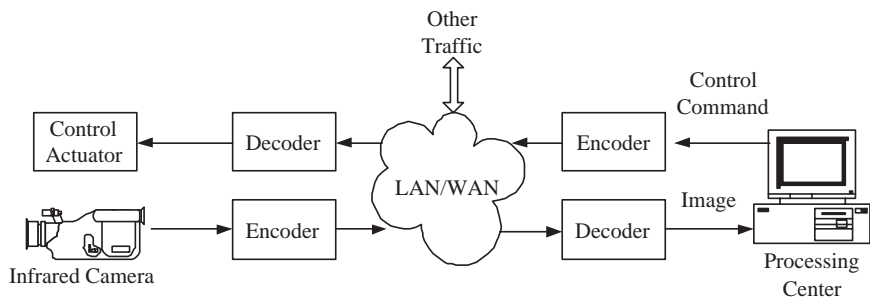
Figure 6.1: A networked sensing and control system.

(a) Jitter Effect   (b) Block Loss
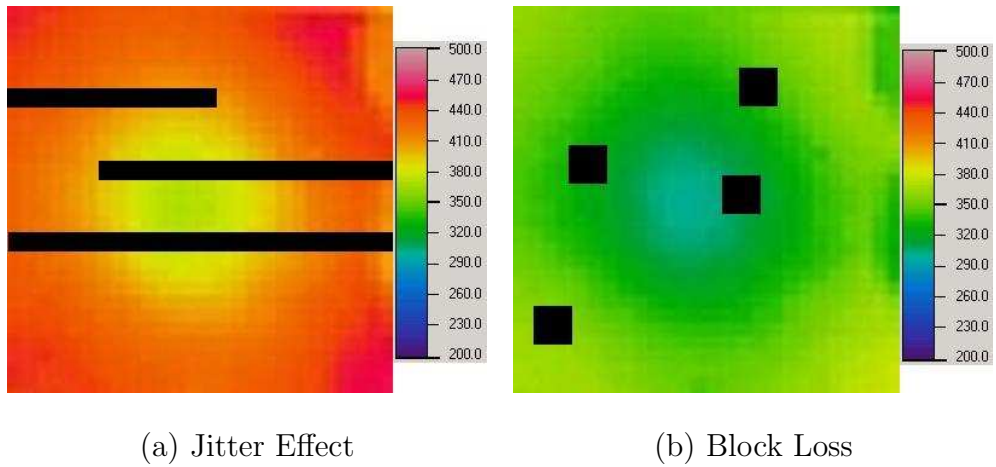
Figure 6.2: Two typical effect caused by packet loss over network where black areas are lost pixels.
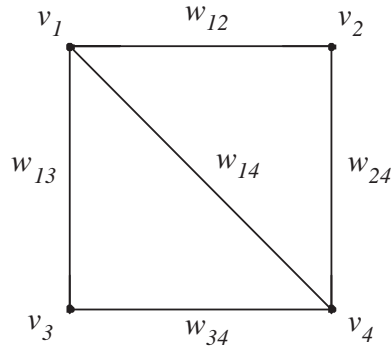
Figure 6.3: A weighted graph.

6.2 Graph Cuts

A graph $G = (V, E)$ is an ordered pair, where V is a nonempty set whose elements are called *vertices* or *nodes*, and where E is a set of unordered pairs of distinct vertices of V whose elements are called *edges* or *links*. A simple graph is illustrated in Figure 6.3, where $v_1, v_2, v_3, v_4 \in V$ are vertices, and the pair $\{v_1, v_2\} \in E$ that joins the vertices v_1 and v_2 is one of its five edges. The edge $\{v_1, v_2\}$ is often abbreviated as $v_1 v_2$ for brevity.

If $v_i v_j \in E$ with $v_i, v_j \in V$, then v_i and v_j are said to be adjacent to each other. The adjacency matrix $A = (a_{ij})_{n \times n}$ for a graph G with n vertices is defined as $a_{ij} = 1$ if v_i and v_j are adjacent to each other, and $a_{ij} = 0$ otherwise, where $i, j = 1, 2, \cdots, n$. The adjacency matrix of Figure 6.3 can be written as

$$A = \begin{bmatrix} 0 & 1 & 1 & 1 \\ 1 & 0 & 0 & 1 \\ 1 & 0 & 0 & 1 \\ 1 & 1 & 1 & 0 \end{bmatrix}$$

A graph G is called weighted graph if there exists a function $w : E \to \mathbb{R}$. The weight $w(v_i v_j)$ with $v_i v_j \in E$ is often abbreviated as w_{ij}. The weight matrix $W =$

113
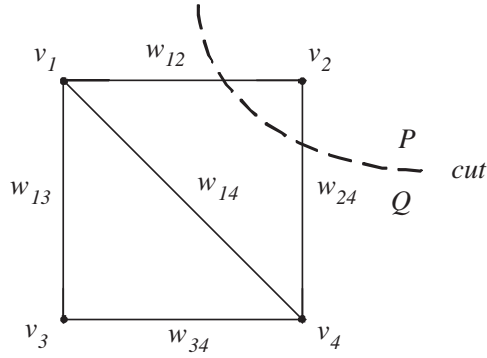
Figure 6.4: A graph cut.

$(w_{ij})_{4\times4}$ for the Figure 6.3 can be written as

$$W = \begin{bmatrix} 0 & w_{12} & w_{13} & w_{14} \\ w_{12} & 0 & 0 & w_{24} \\ w_{13} & 0 & 0 & w_{34} \\ w_{14} & w_{24} & w_{34} & 0 \end{bmatrix}$$

A graph can be partitioned into two disjoined set P and Q with $P \cup Q = V$, and $P \cap Q = \emptyset$. The partition is called *cut*, and its numeric value is defined as

$$cut(P,Q) = \sum_{p\in P, \ q\in Q} w_{pq} \tag{6.1}$$

An example of graph cut is illustrated in Figure 6.4, where the dash line partition the graph into two parts P and Q, with $cut(P,Q) = w_{12} + w_{24}$.

Similarly, graph *association* can be defined as

$$assoc(P,V) = \sum_{p\in P, \ v\in V} w_{pv}$$

which measures the total connections from all nodes in P to the entire nodes in V, where $P \subset V$.

Let X be a $n \times 1$ indicator vector for P with its element $x_i = 1$ if $v_i \in P$ and $x_i = -1$ otherwise, then $(X+\mathbf{1})/2$ and $(X-\mathbf{1})/2$ are also indicator vector for $x_i > 0$

114

and $x_i < 0$ respectively with $\mathbf{1}$ an $n \times 1$ vector of all ones. The X in Figure 6.4 is given by

$$X = (-1, 1, -1, -1)^T$$

Let $d_i = \sum_j w_{ij}$ be the total connection from v_i to all other nodes, and let $D = diag\{d_1, d_2, \cdots, d_n\}$ with $i = 1, 2, \cdots, n$, then it is easy to show that

$$\mathbf{1}^T(D - W)\mathbf{1} = 0 \tag{6.2}$$

Let k and b be two ratios defined as

$$b = \frac{\sum_{x_i>0} d_i}{\sum_{x_i<0} d_i}, \quad k = \frac{\sum_{x_i>0} d_i}{\sum_i d_i}$$

then

$$k = \frac{\sum_{x_i>0} d_i}{\sum_{x_i>0} d_i + \sum_{x_i<0} d_i} = \frac{(\sum_{x_i>0} d_i / \sum_{x_i<0} d_i)}{1 + (\sum_{x_i>0} d_i / \sum_{x_i<0} d_i)} = \frac{b}{1+b} \tag{6.3}$$

The optimal bi-partition of a graph can be achieve by minimizing the cut value in Equation 6.2. A clustering method is proposed in [78] to partition a graph into k subgraphs. However, the method tends to cut small isolated nodes in the graph. To avoid the bias, a normalized cut is proposed. The normalized cut value can be written as [79]:

$$
\begin{aligned}
Ncut(P, Q) &= \frac{cut(P,Q)}{assoc(P,V)} + \frac{cut(Q,P)}{assoc(Q,V)} \\
&= \frac{\sum_{(x_i>0, x_j<0)} -w_{ij}x_i x_j}{\sum_{x_i>0} d_i} + \frac{\sum_{(x_i<0, x_j>0)} -w_{ij}x_i x_j}{\sum_{x_i<0} d_i} \\
&= \frac{(\mathbf{1}+X)^T(D-W)(\mathbf{1}+X)}{4k\mathbf{1}^T D\mathbf{1}} + \frac{(\mathbf{1}-X)^T(D-W)(\mathbf{1}-X)}{4(1-k)\mathbf{1}^T D\mathbf{1}} \\
&= \frac{X^T(D-W)X + \mathbf{1}^T(D-W)\mathbf{1} + 2(1-2k)\mathbf{1}^T(D-W)X}{4k(1-k)\mathbf{1}^T D\mathbf{1}} \\
&= \frac{(1+b)^2 \left[X^T(D-W)X + \mathbf{1}^T(D-W)\mathbf{1} \right] + 2(1-b^2)\mathbf{1}^T(D-W)X}{4b\mathbf{1}^T D\mathbf{1}} \\
&= \frac{\left[(\mathbf{1}+X) - b(\mathbf{1}-X) \right]^T (D-W) \left[(\mathbf{1}+X) - b(\mathbf{1}-X) \right]}{4b\mathbf{1}^T D\mathbf{1}}
\end{aligned}
\tag{6.4}
$$

In the above derivation, Equations 6.2–6.3 are used.

Let $Y = (\mathbf{1} + X) - b(\mathbf{1} - X) \in \{1, -b\}$, then

$$Y^T D Y = \sum_{x_i > 0} d_i + b^2 \sum_{x_i < 0} d_i = b \sum_{x_i < 0} d_i + b^2 \sum_{x_i < 0} d_i = b\mathbf{1}^T D \mathbf{1}$$

Therefore, the optimal partition of G under normalized graph cuts becomes [79]:

$$\min_X Ncut(X) = \min_Y \frac{Y^T(D - W)Y}{Y^T D Y}$$

subject to $y_i \in \{1, -b\}$. Since above equation is the Rayleigh quotient [105], it can be solved by the generalized eigenvalue problem:

$$(D - W)Y = \lambda D Y \tag{6.5}$$

The minimum value is achieved by the second smallest eigenvector, and its minimum value is the corresponding eigenvalue [105]. Ideally the eigenvectors take two discrete values with different signs, but if the eigenvectors take continuous values, it can be split into evenly spaced parts [79].

The normalized graph cut is used first to classified the thermal pattern on a insert surface into several clusters, then the lost packet (image pixels) is patched with the value corresponding to the averaged temperature of the cluster where the packet belongs to.

Algorithm 6.1. *Packet loss recovery: the input is the thermal image subject to packet loss over transmission network, and the position of the lost packet in the image is assumed to be known.*

1. *Find the temperature range of the insert surface excluding the lost regions;*

2. *Construct a graph $G = (V, E)$ with each pixel as a vertex and connect each pair of pixels by an edge. Calculate the weight matrix according to*

$$w_{ij} = \begin{cases} exp\{\frac{-\|T_i - T_j\|_2^2}{\sigma_T^2}\} * exp\{\frac{-\|Z_i - Z_j\|_2^2}{\sigma_Z^2}\}, & if \quad \|Z_i - Z_j\|_2 < r \\ 0, & otherwise \end{cases}$$

where T_i is the temperature at the pixel position i in V, Z_i is the the pixel position of i in original image, σ_T can be taken as 10% to 20% of the temperature range, and σ_Z can be taken as 10% to 20% of the diagonal length of the original image; and

3. *Solve the generalized eigenvalue problem in Equation 6.5, then partition the thermal image into several clusters with each cluster defined by two or more isotherm;*

4. *For each lost image packet, patch the pixels with the value corresponding to the averaged temperature where the packet loss resides.*

6.3 Experimental Results

In this section, an subjective result is presented first to show how the algorithm works, then quantitative comparison between lost and recovered temperature is examined.

6.3.1 General results

An example showing that is illustrated in Figure 6.5. The image is taken from the insert surface of Channel 1 at 8-th second with cooling water flow rate at 3.78L/min. When a packet loss is detected in the thermal image, its thermal pattern can be

classified into three clusters using normalized graph cuts. The lost pixels are patched with the values corresponding to the average temperatures of each cluster. Although the recovered result is rather rough, it can be refined by partitioning the thermal image into more classes. Its accuracy shall be extensively examined under different conditions, including:

1. level of packet loss;

2. level of data length;

3. level of clusters.

6.3.2 Accuracy

Since ground truth image is available, the comparison of accuracy between lost and recovered images can be conducted by computing the absolute error with the original temperature contained in the ground truth image.

The averaged temperature of the insert surface of Channel 1 at 8-th second with cooling water flow rate at 3.78L/min is used as comparison. The experimental results are shown in Tables 6.1-6.2, which is averaged over 100 independent runs. Since the temperature is encoded with 2 bytes length (from 0^oC to 500^oC), the packet length of $32, 128, 512$ bytes is corresponding to 4×4, 8×8, and 16×16 pixels in the image. It can be seen from the tables that the proposed method can recover the almost 50% of the lost temperature under the probability of packet loss less than 0.1. Hence the control system with the proposed robust measurement technique may have better performance.
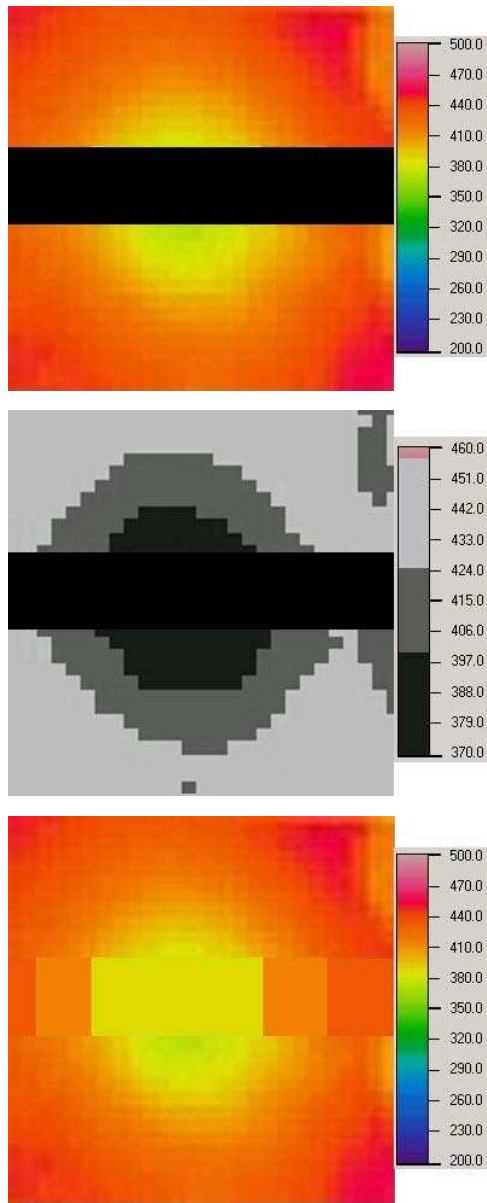
Figure 6.5: Roughly recovered thermal image: (top) a thermal image with a packet loss; (middle) the thermal pattern is classified into three clusters; (bottom) lost pixels are patched with the values corresponding to the average temperatures of each cluster.

Table 6.1: Absolute error (^oC) with variations in packet length and probability of packet drop (3 clusters)

| Method | Packet Length (bytes) | | | Prob. of |
	32	128	512	Packet Loss
Lost	3.83	4.07	4.28	0.01
Recovered	1.26	1.92	2.33	
Lost	18.87	19.25	19.94	0.05
Recovered	9.01	9.89	10.11	
Lost	39.83	40.44	41.77	0.1
Recovered	21.65	23.91	25.07	
Lost	79.72	80.16	82.35	0.2
Recovered	56.88	58.26	60.93	

Table 6.2: Absolute error (^oC) with variations of cluster level (probability of packet drop at 0.1)

| Level | Packet Length (bytes) | | |
	32	128	512
2	26.86	29.35	31.73
3	21.65	23.91	25.07
4	16.89	19.32	21.11
5	10.82	14.17	16.74

6.4   Summary

Graph cuts are applied to recover the packet loss of thermal images. When a packet loss is detected in the thermal image, its thermal pattern can be classified into several clusters using normalized graph cuts. The lost pixels are patched with the values corresponding to the average temperatures of each cluster. Simulation results show that the proposed method can recover part of the temperature loss due to network effect.

Chapter 7

Thermal Process Control

A fuzzy PID controller is designed to demonstrate the possibility to implement the vision-based thermal control system. The respectively averaged surface temperature of three die inserts, which are measured by cameras, are used as state feedback, and the control goal is to minimize the temperature difference among the inserts. The demo shows that the system can work efficiently.

7.1   Introduction

As mentioned in previous chapter, the improper distribution of die temperatures may cause many casting defects [3]. Conventionally, control of die temperature is based on operators' experience and trial-and-error. On the one hand, localized over-cooling which leads to the formation of defects such as poor fill can be manually adjusted by decreasing water flow rates in a specific cooling line. On the other hand, casting defects such as porosity and hot tearing, which result from hot spots with abnormal high temperatures present in the die, become difficult to alleviate if the established cooling lines are already running at maximum flow rates.

In general, a system model is necessary for applying traditional control approach to design an effective controller. However, distribution of die temperature depends on a lot of factors such as geometry of die and casting process variables, for which it would be difficult to derive a detailed model. Instead of modeling a complex process, an operator's skilled control actions can also be modeled in terms of fuzzy implications using the input-output data associated with the control actions. Then a fuzzy controller can be designed based on the "input-output model" to compensate the undesirable behavior of the process [83]. This section will use the configuration in Figure 2.1. Consider that Water Inlets 1 and 2 are established cooling waterlines in a die. In this scheme, an extra waterline supplying water with a water tank from Water Inlet 0 controlled by a pump and solenoid valves is connected to the existing cooling channels. The pump and solenoid valves can be actuated automatically to bring additional cooling water to the locally overheated die insert. Since it has been demonstrated that an increase in internal cooling water flow rates reduces the temperatures of casting dies rapidly [3], the desired thermal pattern of the die insert becomes achievable through this scheme. The fuzzy PID controller is designed to minimize the temperature differences among multiple channels in a die insert.

7.2   Two-input Fuzzy PID Controller

Fuzzy control, in principle, imitates human being's fuzzy thinking style and implements control action without having much knowledge on the underlying dynamics of the system [83, 84, 85]. The basic architecture of the fuzzy control system is shown in Figure 7.1, where $\mu(x)$ is the membership function of input vector x, and $\mu(c)$ is
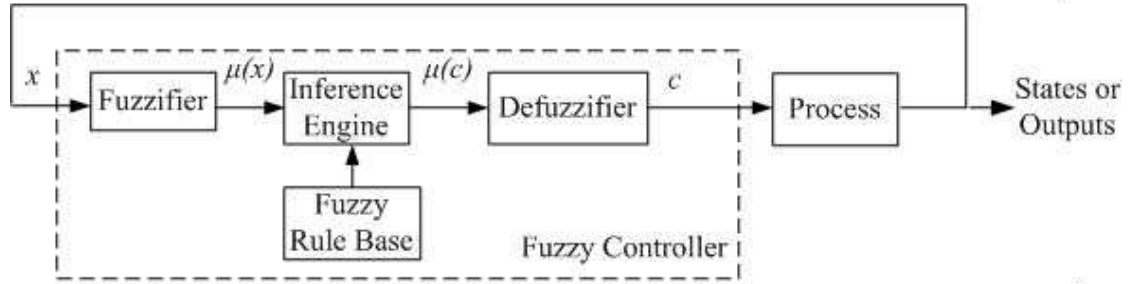
Figure 7.1: Basic Structure of Fuzzy control system
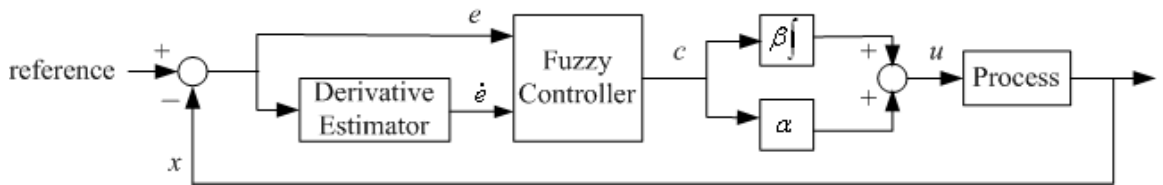
Figure 7.2: Fuzzy PID control system

the membership function of output vector c.

The empirical knowledge on how the domain experts operate the process is modeled and stored in the fuzzy rule base. Sugeno-type fuzzy model is widely used in various industrial applications. In general form, it can be written as [85]

Rule k: IF x_1 is $A_1{}^i$, and x_2 is $A_2{}^j$, THEN $c_k = a_i x_1 + b_j x_2 + c_{k_0}$

where $A_1{}^i$ and $A_2{}^j$ are the fuzzy sets in antecedent that describe the nature of the inputs, such as *low*, *okay* or *high*, and a_i, b_j, and c_{k_0} are constants. If $a_i = b_j = 0$, the rule base becomes a zero-order Sugeno fuzzy model, i.e., the consequent part of the fuzzy rule is a singleton spike.

It is known that fuzzy PI control has poor performance in transient response for

	Antecedent		Conseqence	Weight
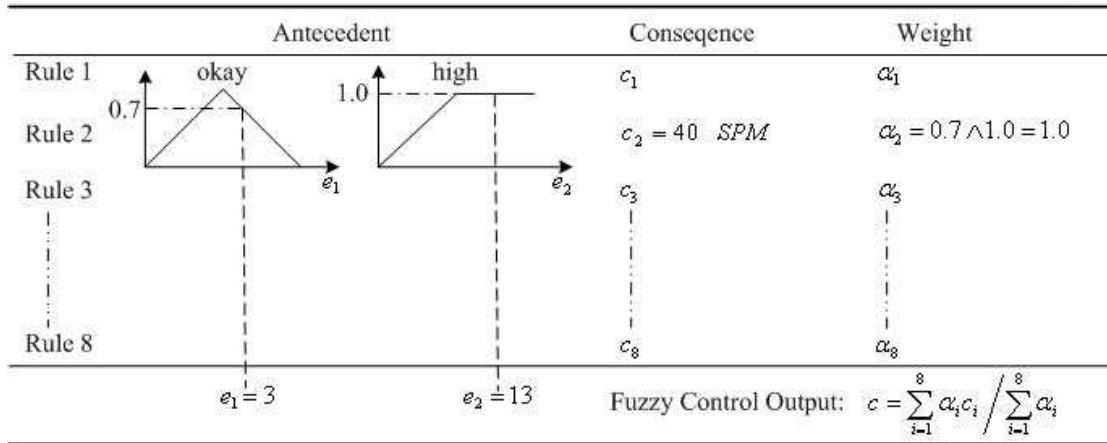
Figure 7.3: Fuzzy reasoning process

higher order processes due to the integration operation, while it is difficult for fuzzy PD to remove steady state error. Therefore fuzzy PID control has more advantageous. Various architectures of fuzzy PID control are available in literature. The one used in this application is shown in Figure 7.2 [88, 89], where α and β are constants. At any time $t = k$, the crisp error e and error change $\dot{e}$ are defined as

$$e(k) = r - x(k)$$
$$\dot{e}(k) = e(k) - e(k - 1)$$
(7.1)

where r is the reference signal. It has also been shown in [88, 90] that if a fuzzy controllers with 1)Larsen's product-sum inference method or Mamdani's minimum inference engine; 2)center of gravity defuzzification method; 3)triangular uniformly distributed membership functions for the inputs; and 4)singleton output (zero-order Sugeno model), the output of the fuzzy controller has a PD form:

$$c = c_0 + k_p e + k_d \dot{e}$$

where c_0, k_p, and k_d are coefficients. Then it follows that the control signal u in

125

Figure 7.2 can be written as

$$
\begin{aligned}
u &= (\alpha c_0 + \beta c_0 t) + (\alpha k_p + \beta k_d)e + \beta k_p \int e\, dt + \alpha k_d \dot{e} \\
&= u_0 + \bar{k}_p e + \bar{k}_i \int e\, dt + \bar{k}_d \dot{e}
\end{aligned}
\tag{7.2}
$$

where $u_0 = \alpha c_0 + \beta c_0 t$, $\bar{k}_p = \alpha k_p + \beta k_d$, $\bar{k}_i = \beta k_p$, and $\bar{k}_d = \alpha k_d$. Thus a fuzzy PID controller can be obtained from a fuzzy PD controller.

The control goal in this application is to limit the absolute value of the temperature differences between two channels in a given bound within a given time period, i.e., to find a time t such that

$$
e_i(k) = |M_i(k) - M_3(k)| \leq \delta, \quad i = 1, 2, \quad \forall t \geq T
\tag{7.3}
$$

where $M_i(t)$ and $M_3(t)$ represent measured temperatures at time $t = k$ in Celsius Degree at Channel i ($i = 1, 2$) and Channel 3, δ and T are positive constants in Celsius Degree and Second respectively. Temperature of Channel 3 $M_3(t)$ is used as reference signal since it is the lowest among the three from observations.

The input variables to the fuzzy controller are temperature differences between two channels (abbreviated as *error*) and the error changes, denoted as e_i and $\dot{e}_i$ with ($i = 1, 2$) respectively. The system has three output variables, namely, pump speed and on/off signals of two solenoid valves. Let c be the output pump speed, and s_1, s_2 be the status of the solenoid valves with 0 representing *close* and 1 representing *open*. The operator's control actions can be modeled as a collection of Sugeno fuzzy rules combined by the connective ELSE. A possible rules are listed below:

Rule 1: IF e_1 and e_2 are *okay*, THEN $c_1 = 0$, $s_1 = 0$, $s_2 = 0$, ELSE;

Rule 2: IF e_1 is *okay* and e_2 is *high,*, THEN $c_2 = 40\text{SPM}$, $s_1 = 0$, $s_2 = 1$, ELSE;

Rule 3: IF e_1 is *high* and e_2 is *high,*, THEN $c_3 = 100\text{SPM}$, $s_1 = 1$, $s_2 = 1$, ELSE;

Rule 4: IF $e_1, e_2, \dot{e}_2$ are *okay* and $\dot{e}_1$ is *positive*, THEN $c_4 = 40$SPM, $s_1 = 1$, $s_2 = 0$, ELSE;

Rule 5: IF $e_1, e_2, \dot{e}_1$ are *okay* and $\dot{e}_2$ is *positive*, THEN $c_5 = 20$SPM, $s_1 = 0$, $s_2 = 1$, ELSE;

Rule 6: IF e_1, e_2, are *okay* and $\dot{e}_1, \dot{e}_2$ are *positive*, THEN $c_6 = 80$SPM, $s_1 = 1$, $s_2 = 1$, ELSE;

Rule 7: IF e_1 is *low*, THEN $s_1 = 0$, ELSE;

Rule 8: IF e_2 is *low*, THEN $s_0 = 0$, ELSE;

The output consequences are not symmetry with respect to the origin due to the fact that the temperature sensors are buried in different depths in each channel in order to simulate temperature gradient for control purpose. See Section 2 for more details.

Suppose that at time $t = k$, the four input variables are given by e_i and $\dot{e}_i$ with $i = 1, 2$ respectively. A crisp output of the fuzzy controller, c, may be inferred from the Mamdani's minimum inference method through following procedures:

Step 1: For each implication Rule i, find c_i from fuzzy rule base listed above;

Step 2: Let α_i be the weighting factor of the ith rule, which is a measure of the contribution of the ith rule to the fuzzy control action. The α_i is given as

$$\alpha_i = A_1^i(e_1) \wedge A_2^i(\dot{e}_1) \wedge A_3^i(e_2) \wedge A_4^{\,i}(\dot{e}_2) \equiv min[A_1^{\,i}(e_1), A_2^{\,i}(\dot{e}_1), A_3^i(e_2), A_4^{\,i}(\dot{e}_2)]$$

Step 3:   The fuzzy controller output c can be calculated as the average of all c_i with the weights α_i .

$$c = \frac{\sum_{i=1}^{8} \alpha_i c_i}{\sum_{i=1}^{8} \alpha_i}$$

The fuzzy reasoning process is shown in Figure 7.3, where only Rule 2 is listed as examples with input variables $e_1 = 3$, and $e_2 = 13$ respectively. For each given pair of input $(e, \dot{e})$, the consequences c_i can be find directly from the fuzzy rule base. The weight factors are calculated through fuzzy min operator between the memberships from the two inputs. Control output is then averaged over all consequences with the weight factors.

Final control signal u as shown in Figure 7.2 can be obtained by taking $\alpha = 1$ and $\beta = 0.1$ in this application, and integral is taken from $t = k - 4$ to $t = k$. Since Windows XP used in this study is an operating system that does not have real-time performance, the latency, which is defined as the time interval for application software to transmit command to hardware, is unpredictable. Malfunction of the controller may be caused, especially when the control action updating rates are faster than the latency. For example, control failure may happen when the next control command comes while the previous control command has not been executed yet. In addition, sensors and actuators also introduce time delays to the control system, which further corrupts the performance of the controller. Therefore, it is impractical to send out control command after every sampling (0.25 second in this application). Experimental results to be shown in Section 5 will also indicate that there are significant time delays in the process. In order to minimize the adverse effect of the time delay, fuzzy values can be quantized and stored in memory in the form of a look-up table as shown in Table 7.1. The computer acquires temperature signals from each cooling channel at

128

Table 7.1: Look-up table for Fuzzy PID Controller (unit: SPM)

Error(^oC)	$e_1 \geq 10$	$-10 < e_1 < 10$	$e_1 < -10$
$e_2 \geq 10$	100 ($s_1 = 1, s_2 = 1$)	40 ($s_1 = 0, s_2 = 1$)	40 ($s_1 = 0, s_2 = 1$)
$-10 < e_2 < 10$	60 ($s_1 = 1, s_2 = 0$)	0 ($s_1 = 0, s_2 = 0$)	0 ($s_1 = 0, s_2 = 0$)
$e_2 < -10$	60 ($s_1 = 1, s_2 = 0$)	0 ($s_1 = 0, s_2 = 0$)	0 ($s_1 = 0, s_2 = 0$)

a fixed sampling rate; then e and $\dot{e}$ are calculated after each sampling. For a given temperature error and error change, the corresponding pump speed can be found from the table.

7.3 Experimental Results

As the furnace is bottom heated and the length of the three die inserts is different, their temperatures are different when pulled out from the furnace. Then, the fuzzy controller set in to adjust the temperature differences between two channels. In this experiment, the control goal is set to $\delta = 10^oC$ and $T = 20$ seconds in Equation 7.3. The experimental procedures are summarized as follows:

Experiment Procedures 7.1. *A fuzzy controller.*

1. *Preheat the die insert to 480ºC ; pull them out of the furnace; and*

2. *Open Water Inlet 1 and 2 at a flow rate of 2.65 L/min (0.7 GPM) to cool down Channel 1 and 2 respectively, while keep a small amount of water running through Channel 3 (less than 0.55 GPM); and at the same time*

3. *Use the cameras as temperature sensors, and start the fuzzy controller to supply*
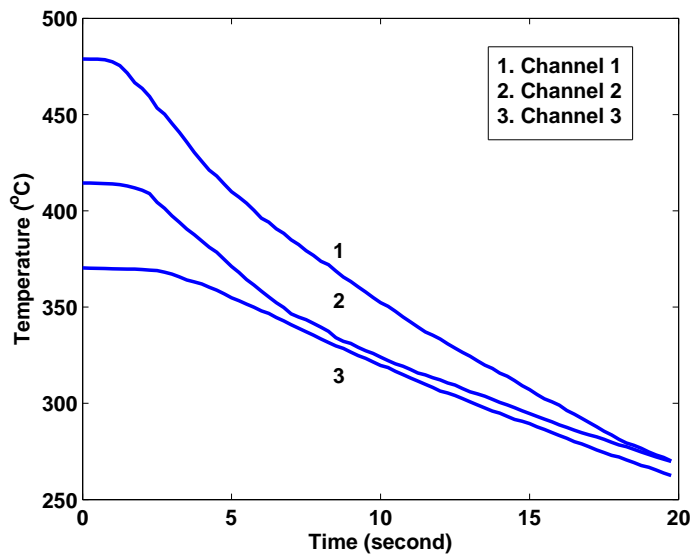
Figure 7.4: Temperature variations of three surfaces under a fuzzy controller.
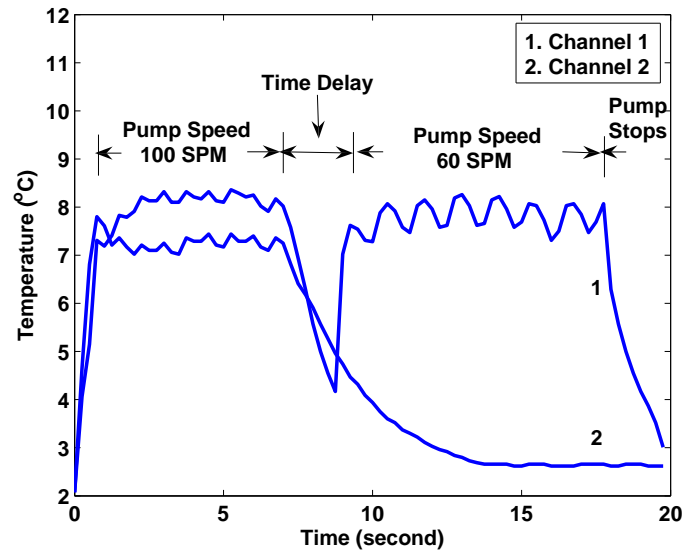
Figure 7.5: Flow rates under a fuzzy controller

130

extra water to Channel 1 and 2.

Figure 7.4 illustrates the temperature variation of the die insert at three locations (Channel 1, 2 and 3). It can be seen from the figure that the temperature at Channel 1 is much higher than that of Channel 2 and 3 at 0 second. The flow rates of Channel 1 and 2 are also plotted in Figure 7.5. At the first 7 seconds, the pump speed is adjusted to 100 SPM since the temperatures of both Channel 1 and 2 are higher than that of 3. Upon the opening of Water Inlet 0, 1 and 2, the temperature at locations 1 and 2 decreases rapidly. As the temperature difference between Channel 2 and 3 is minimized to within 10^oC, the pump speed changes to 60 SPM in accordance with the fuzzy control table and the solenoid valve 2 closes, which cuts off the extra water to Channel 2. At around 19 seconds, the temperature difference between Channel 1 and 3 is minimized to within 10^oC, the pump stops and solenoid valve 1 closes. In contrary, the constant water flow rate of Channel 2 decreases the temperature at location 2 steadily. There is a difference in the behaviour of the temperature drops between the two locations of the die insert. This observation indicates that the designed vision based control system is capable of reducing die temperature locally by varying the water flow rates of each individual channel in a die which may contain multiple cooling lines.

It should be noted that time delay (latency) occurs when the fuzzy controller updates the pump speed as shown in Figure 7.5. Therefore, it is impractical to change the control action after each sampling.

The averaged temperature of the insert surfaces before and after control is listed in Table 7.2. The graphic comparison of the temperatures is also plotted in Figure 7.6. Although there are specific hot/cool spots on each surface, the temperature

131

Table 7.2: Averaged temperature (^{o}C) of the insert surfaces before and after control

Time	Channel 1	Channel 2	Channel 3
0-th second	479.8	414.4	370.3
20-th second	270.1	26980	262.5

distribution among three channels become more homogeneous.

7.4 Summary

A simply Fuzzy PID controller has been designed and implemented to test the performance of the visual sensor. The experimental results show that the system has a great potential for real world applications.

Channel 1 at 0 second   Channel 1 at 20 second

Channel 2 at 0 second   Channel 2 at 20 second

Channel 3 at 0 second   Channel 3 at 20 second
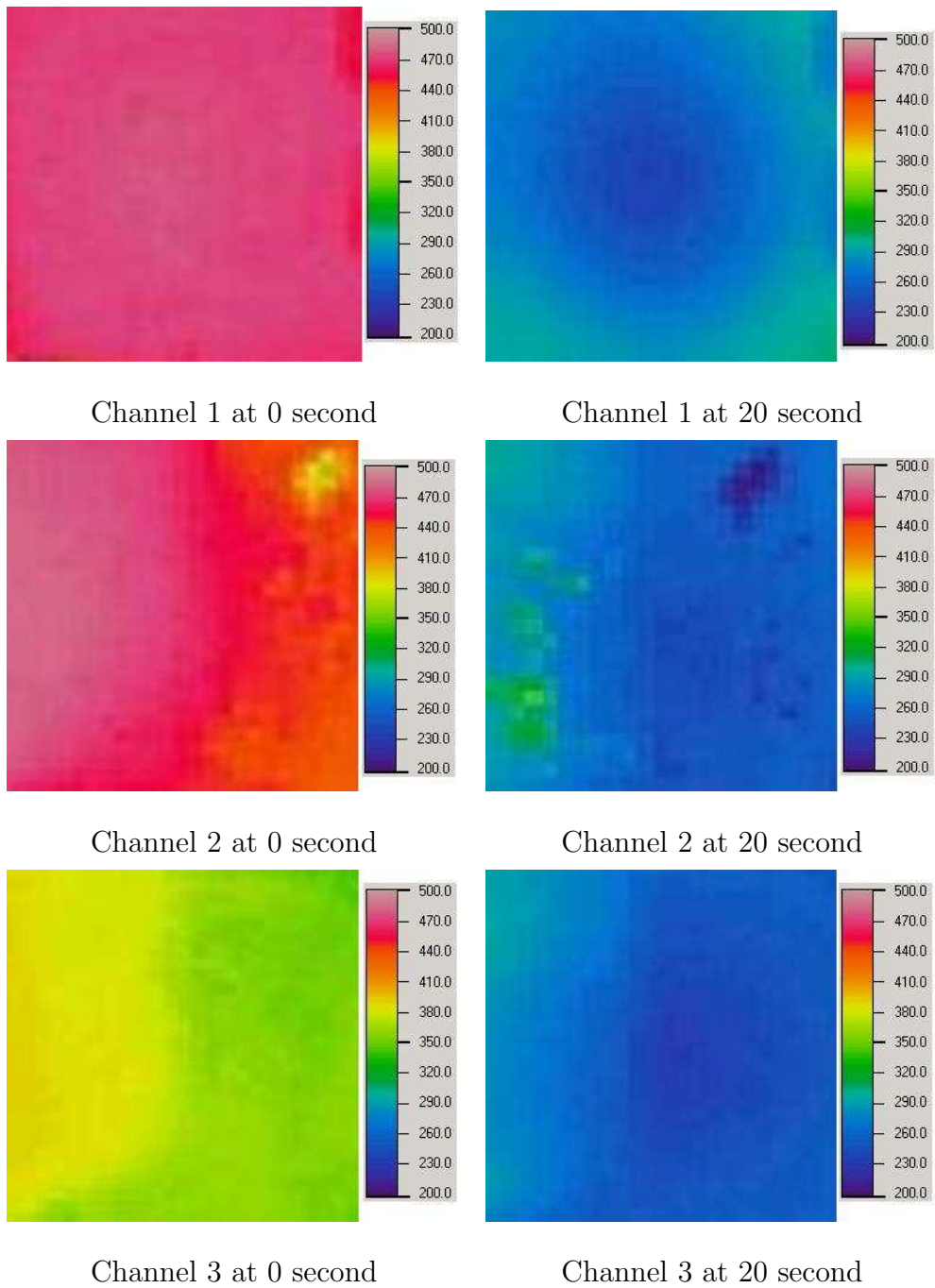
Figure 7.6: Comparison of the temperatures of the insert surfaces before and after control.

Chapter 8

Conclusions and Future Work

This chapter summarizes the main conclusions of the present work, and suggestions for future research are also provided.

8.1   Summary of Main Contributions

In this study, a vision-based thermal control system has been developed for industrial automation. Two new methods have been proposed to achieve robust temperature measurement. The primary original contributions of the dissertation can be summarized as follows:

1. An adaptive curve fitting technique is proposed based on PRESS statistic test for the sampled data set containing noises or outliers. The method converges very fast, and superaccuracy can be obtained under certain conditions when compared with other methods. The method is applied to estimate an optimal curve of casting dies from the visual images;

2. A method for the recovery of thermal image loss is proposed. The thermal image loss generated by network traffic from camera nodes to fusion center is modeled

as a Markov chain. A graph cuts method is used to recover the loss based on thermal pattern classification. Simulation results show that thermal information can be partially retrieved, which may greatly increase the robustness of a thermal management system.

Other contributions may include:

1. A vision-based fuzzy PID controller has been implemented to minimize the temperature difference among the die inserts. The controller is capable of effectively adjusting the pump speed and turn on/off the solenoid valves according to the temperature difference and the error change. Consequently the flow rate of cooling water can be varied to reduce the temperature of the hot insert;

2. A 3D thermal model has been reconstructed. It has been found that temperatures on individual insert surface are locally inhomogeneous during the cooling processes. The center temperature, due to closer to the cooling channel, is usually lower than that of its surrounding neighbors. But globally, the averaged temperature of several die inserts can be controlled to achieve more homogeneous temperature distribution as demonstrated by the controller; and

3. Different influential factors on the emissivity of die surface have been discussed and experiments have been conducted to examine the factors qualitatively and quantitatively.

8.2   Suggestions for Future Research

It should be noted that numerous improvements need to be carried out in order to put the results of the present work into practical use. The major suggestions for future research can be divided into two categories.

On the technical side:

1. It should be noted that it is possible to generate a 3D thermal image from an infrared camera alone and the two visual cameras can be eliminated on the condition that: 1) the CAD information is available; 2) the outer contour of the die can be detected from its thermal image. A laser profiler can also be used to replace the two visual camera;

2. Robust thermal image features. It is an interesting topic in visual image on how to find the robust image features. In the thermal image domain, it becomes more challenging since image corners in visual images may disappear in thermal image when they have the same or similar temperature with their neighbors. If image features decreases, it will have adverse effect on the image correspondence, local shape determination, especially in an unstructured environment;

3. The two robust algorithm can be further improved. As both of them involves iterations, so it may become a time consuming process especially for the second one. Since thermal image is formed from temperatures, a simple contour connection algorithm needs to be designed for practical use.

4. It has been found that for the adaptive curve fitting algorithm, if the outliers are over 50%, there is no room to improve the accuracy of the algorithm. Except

for those searching algorithm such as RANSAC, new method has to be designed for real time applications.

On the application side:

1. Die casting simulator. The currently used simulator has limited functions that hinder its ability to simulate complexity involved in real die casting processes. Although it simulates the solidification stage of the die casting process, the stage of die lubrication and the cycling nature of the process cannot be obtained from the current settings. The simulator has to be re-designed to consider the entire cycle of die casting processes, including die lubrication which reduces the temperature of the die surface and consequently makes contribution to heat transfer from the die to its surroundings.

2. Since the die is closed during production, it is impossible to acquire thermal images at that stage. The image of a die surface is accessible only after the die is open and the casting is ejected. It is reasonable to assume that a hot spot, after the die is open, is still a hot spot before the die is open. Under this circumstances, if the control goal is to minimize the final temperature differences, a controller needs to be redesigned through an iterative process.

As vision-based control system is relatively a new addition to the control field, new theories and applications come out frequently. Also at the same time, new emerging industrial problems become increasingly challenging.

Bibliography

[1] M. Vincze, and G.D. Hager (eds.), "Robust Vision for Vision-based Control of Motion," Wiley-IEEE Press, 2000.

[2] F. Chen, "Data acquisition system for die casting processes," M.A.Sc. Thesis, University of Windsor, 2002.

[3] H. Hu, F. Chen, X. Chen, Y. Chu, and P. Cheng, "Effect of cooling water flow rates on local temperatures and heat transfer of casting dies," *Journal of Materials Processing Technology*, Vol. 148, Iss. 1, pp. 57-67, 2004.

[4] H. Hu, F. Chen, X. Chen, Y. Chu, and P. Cheng, "Development of a computer-based data acquisition and control system for die casting Processes," *Proceedings of the EPD Congress, TMS*, pp.439-451, 2002.

[5] B.K. Dent, and R. Fifer, "Production operation with the Llzro-Battelle die temperature controller," *Proceedings of the Seventh SDCE International Die Casting Congress*, paper number 5572, 1972.

[6] A.P. Peterson, "Thermocycling control of aluminum die casting machines," *Proceedings of the Eighth SDCE International Die Casting Congress*, paper number B-t75-024, 1975.

[7] S.E. Booth, "A die temperature cycle time controller," *Proceedings of the Sixth SDCE International Die Casting Congress*, 54, 1970.

[8] W. Bishenden, and R. Bhoia, "Die temperature control," *Proceedings of the Transactions of 20th International Die Casting Congress*, pp. 161-164, 1999.

[9] T. Yang, X. Chen, H. Hu, Y. Chu, and P. Cheng, "A fuzzy PID thermal control system for casting dies," *Journal of Intelligent Manufacturing,* Springer, Vol. 19, pp. 375-382, 2008.

[10] T. Yang, H. Hu, X. Chen, Y. Chu, and P. Cheng, "Thermal analysis of casting dies with local temperature controller," *International Journal of Advanced Manufacturing Technology*, Vol. 33, No. 3-4, pp. 277-284, 2007.

[11] X. Niu, J. Kiriakakis, and K. Steinbauer, "Application of Infrared Thermal Imaging Technique in High Pressure Die Casting," Proc. NADCA Transactions, pp.101–108, T03–023, 2003.

[12] S.W. Hao, B.H. Hu, and X.P. Niu. "Die temperature study by infrared thermography," *Die Casting Engineer*, Vol. 42, No. 2, pp.62–66, 1998.

[13] R.J. Larkin, "Automatic control die temperature in zinc die casting," *Proceedings of the Sixth SDCE International Die Casting Congress*, paper number 62, 1970.

[14] R. Reddy, "Temperature control of die casting dies," *Proceedings of the Eighth SDCE International Die Casting Congress,*paper number B-t75-025, 1975.

[15] T. Yang, H. Hu, X. Chen, Y. Chu, and P. Cheng, "On-line Thermal Management System for Die Casting Processes," *Proceedings of 5th International Workshop on Advanced Manufacturing Technologies*, National Research Council Canada, pp189-196, 2005.

[16] T. Yang, H. Hu, X. Chen, Y. Chu, and P. Cheng, "An Intelligent Control System for Die Thermal Management," *Proc. Materials Science and Technology, Sub-symposium on Automation and Control,* TMS, Pittsburg, PA, USA, pp.11-20, Sept. 2005.

139

[17] P. Gorbach, "The use of temperature control unit in die casting dies," *Die Casting Engineer,* Vol. 46, No. 6, pp.50-55, 2002.

[18] H. Wang, X. Yi, J. Lai, and Y. Li, "Fabricating microbolometer array on unplanar readout integrated circuit," *International Journal of Infrared and Millimeter Waves*, Vol. 26, No.5, pp.751–762, 2005.

[19] L. Ibos, M. Marchetti, A. Boudenne, S. Datcu, Y. Candau, and J. Livet, "Infrared emissivity measurement device: principle and applications," *Measurment Science and Technology*, Vol. 17, pp.2950–2956, 2006.

[20] R.J. Chandos, and R.E. Chandos, "Radiometric properties of isothermal diffuse wall cavity sources," *Applied Optics*, Vol. 13, No. 9, pp.2142-2152, 1974.

[21] M. Q. Brewster, *Thermal radiative transfer and properties,* Wiley-Interscience, 1992.

[22] J.R. Mahan, *Radiation heat transfer: a statistical approach,* Wiley-IEEE, 2002.

[23] P. Dash, F.-M. Gottsche, F.-S. Olesen, and H. Fischer, "Land surface temperature and emissivity estimation from passive sensor data: theory and practiceCcurrent trends," *Internatinal Journal of Remote Sensing*, Vol. 23, No. 13, pp.2563–2594, 2002.

[24] W. Gogol, and B. Staniszewski, "Thermophysical properties research in Poland," *Proceedings of the Symposium on Thermophysical Properties*, Gaithersburg, MD, USA, pp.55–66, 1977.

[25] M. Prystay, C.A. Loong, and K. Nguyen, "Optimization of cooling channel design and spray patterns in aluminum die casting using infrared thermography," *Proc. Thermosense XVIII,* SPIE Vol. 2766, pp.15–24, 1996.

[26] F.Y. Sorrell, and R.S. Gyurcsik, "Model-based emissivity correction in pyrometer temperature control of rapid thermal processing systems," *IEEE Transactions on Semiconductor Manufacturing,* Vol. 6, No. 3, pp.273–276, 1993.

[27] F. Ghmari, T. Ghbara, M. Laroche, R. Carminati, and J.-J. Greffet, "Influence of microroughness on emissivity," *Journal of Applied Physics,* Vol: 96, Issue: 5, pp.2656–2664, 2004.

[28] M. Siroux, E. Tang-Kwor, and S. Mattei, "A periodic technique for emissivity measurements of insulating materials at moderate temperature," *Meas. Sci. Technol.,* Vol: 9, pp.1956–1962, 1998.

[29] T. Furukawa, and T. Luchi, "Experimental apparatus for radiometric emissivity measurements of metals," *Rev. Sci. Instrum.* Vol.71, pp.2843–7, 2000.

[30] A. Pantinakis, and N. Kortsalioudanis, "A simple high-sensitivity radiometer in the infrared for measurements of the directional total emissivity of opaque materials at near-ambient temperatures," *Int. J. Thermophys.* Vol.22, pp.1843–54, 2001.

[31] S.L. Liang, " Inversion of land surface temperature and emissivity simultaneously from multispectral thermal infrared imagery," *Proc. IEEE IGARSS,* IEEE Proc. Cat. No. 00CH37120, vol 7, pp.3133–5, 2000.

[32] R.P. Madding, " Emissivity measurement and temperature correction accuracy considerations," *Proc. SPIE*, Vol. 3700, pp.393–401, 1999.

[33] R.P. Madding, "Temperature dependence of the graybody approximation to emissivity for some common materials," *Proc. SPIE*, Vol. 4170, pp.37–43, 2002.

[34] M. Born, and E. Wolf, "Principles of Optics," Elmsford, NY: Pergamon, 1980.

[35] B.Widrow, and S.D. Stearns, "Adaptive Signal Processing," Prentice Hall, Englewood Cliffs, NJ, 1985.

[36] E. Trucco, and A. Verri, "Introductory techniques for 3–D computer vision," Prentice Hall, 1998.

[37] A.V. Oppenheim, R.V. Schafer, and J.R. Buck, "Discrete-time digital signal processing," Prentice Hall, 1999.

[38] N. Bennet, R. Burridge, and N. Saoki, "A method to detect and characterize ellipses using the Hough transform," *IEEE Trans. Patt. Anal. Mach. Intell.* 21: 652–657, 1999.

[39] J. Porrill, "Fitting ellipses and predicting confidence envelopes using a bias corrected Kalman filter,"*Imag. Vis. Comput.* 8: pp.37–41, 1990.

[40] P.L. Rosin, "Ellipse fitting by accumulating five-point fits,"*Patt. Recogn. Lett.* 14 pp.661–699, 1993.

[41] I. Markovsky, and S. Van Huffel, "Overview of total least squares methods," *Signal Processing,* vol. 87, pp. 2283–2302, 2007.

[42] A. Fitzgibbon, M. Pilu, and R.B. Fisher, "Direct least square fitting of ellipses," *IEEE Trans. PAMI,* 21(5), pp. 476–480, May 1999.

[43] E. S. Maini, "Enhanced direct least square fitting of ellipses," *International Journal of Pattern Recognition and Artificial Intelligence,* Vol. 20, No. 6, pp. 939–953, 2006.

[44] F. L. Bookstein, "Fitting conic sections to scattered data, " *Comput. Graph. Imag. Process,* Iss. 9, pp. 56–71, 1979.

[45] G. Taubin, "Estimation of planar curves, surfaces and non- planar space curves defined by implicit equations, with applications to edge and range image segmentation," *IEEE Trans. Pattern Analysis and Machine Intelligence,* vol. 13, no. 11, pp. 1,115–1,138, Nov. 1991.

[46] W. Gander, G.H. Golub, and R. Strebel, "Least-square fitting of circles and ellipses," *BIT,* no. 43, pp. 558–578, 1994.

[47] K. Kanatani, "Statistical bias of conic fitting and renormalization," *IEEE Trans. Pattern Analysis and Machine Intelligence,* vol. 16, no. 3, pp. 320–326, 1994.

[48] D. S. Barwick, "Very fast best-fit circular and elliptical boundaries by chord data," *IEEE Trans. Pattern Analysis and Machine Intelligence,* VOL. 31, NO. 6, pp.1147–1152, JUNE 2009.

[49] Z. Zhang, "Parameter estimation techniques: a tutorial with application to conic fitting," *Image and Vision Computing Journal,* Vol.15, No.1, pp. 59–76, 1997.

[50] M. Sid-Ahmed, *Image Procesing: Theory, Algorithms, and Architectures,* Mcgraw-Hill, New York, NY, 1995.

[51] S. Jo, and S. W. Kim, "Consistent normalized least mean square filtering with noisy data matrix," *IEEE Trans. Signal Processing,* vol. 53, no. 6, pp. 2112–2123, Jun. 2005.

[52] P. O'Leary, and P. Zsombor-Murray, "Direct and specific least-square fitting of hyperbolic and ellipses" *Journal of Electronic Imaging,* Vol. 13, 492, 2004.

[53] A.W. Fitzgibbon, and R.B. Fisher, "A buyer's guide to conic fitting," *Proceedings of the 6th British conference on Machine vision,* Vol. 2, pp.513–522, 1995.

[54] P.M. Ramos, F. M. Janeiro, M. Tlemcani, and A. C. Serra, "Recent developments on impedance measurements with DSP-based ellipse-fitting algorithms," *IEEE Transactions on Instrumentation and Measurement,* VOL. 58, NO. 5, pp.1680–1689, MAY 2009

[55] B. Zitova, and J. Flusser, "Image registration methods: a survey," *Image Vis. Comput.,* 21.977–1000, 2003.

[56] P. Meer, D. Mintz, A. Rosenfeld, and D.Y. Kim, " Robust regression methods for computer vision: A review," *International Journal Computer Vision,* 6(1):59–70, 1991.

[57] R.C. Bolles and M.A. Fischler, "A RANSAC-based approach to model ftting and its application to finding cylinders in range data," *Proc. Int'l Joint Conf. Artif. Intell.,* pages 637–643, Vancouver, Canada, 1981.

[58] F.A. Graybill, *Theory and Application of teh Linear Model,* Duxbury, Boston, MA, 1976.

[59] M.G. Kendall, and A. Stuart, *The advanced Theory of Statistics, vol. 2, Inference and Relationship, 3ed.,* Hafner, New York, 1973.

[60] G.A.F. Seber, *Linear Regression Analysis,* John Wiley & Sons, New York, 1977.

[61] H. Bay, A. Ess, T. Tuytelaars, and L. Van Gool, "SURF: Speeded Up Robust Features", *Computer Vision and Image Understanding,* Vol. 110, No. 3, pp. 346–359, 2008

[62] D.G. Lowe," Distinctive Image Features from Scale-Invariant Keypoints, " *International Journal of Computer Vision,* 60 (2): 91–110 , 2004.

[63] E.R. Davies, "The application of machine vision to food and agriculture: a review," *Imaging Science Journal,* Volume: 57 Issue: 4 Pages: 197-217, Published: AUG 2009.

[64] A. Kumar, "Computer-vision-based fabric defect detection: A survey," *IEEE Transactions on Industrial Electronics,* Volume: 55 Issue: 1 Pages: 348-363, Published: JAN 2008.

[65] V. Kastrinaki, M. Zervakis, and K. Kalaitzakis, "A survey of video processing techniques for traffic applications," *Image and Vision Computing,* Volume: 21 Issue: 4 Pages: 359-381, Published: APR 1 2003.

[66] E.D. Cohen, "Prosthetic interfaces with the visual system: biological issues," *Journal of Neural Engineering,* Volume: 4 Issue: 2 Pages: R14-R31, Published: JUN 2007.

[67] A. Beyeler, J.C. Zufferey, and D. Floreano, "Vision-based control of near-obstacle flight," *Autonomous Robots,* Volume: 27 Issue: 3 Pages: 201-219, Published: OCT 2009.

[68] N. Lazaros, G.C. Sirakoulis, and A. Gasteratos, "Review of stereo vision algorithms: from software to hardware," *Internatinal Journal of Optomechatronics,* Volume: 2, Issue: 4, Pages: 435-462, 2008.

[69] R.Y. Tsai, "A versatile camera calibration technique for high accuracy 3D machine vision metrology using off the shelf TV cameras and lenses," *IEEE Jounal of robotics and Automation,* Vol. RA-3, No.4, pp.323–344, 1987.

[70] D. Scharstein, and R. Szeliski, "A taxonomy and evaluation of dense two frame stereo correspondence algorithms," *International Journal of Computer Vision,* 47(1C3), pp.7–42,2002.

[71] R. Hartley, and A. Zisserman, *Multiple View Geometry in Computer Vision, Second ed.,* Cambridge, UK: Cambridge University Press, 2004.

[72] D.A. Forsyth, and J. Ponce, *Computer Vision: A modern Approach,* Upper Saddle River, NJ, USA: Prentice Hall, 2002.

[73] Y. Ma, S. Soatto, J. Košeckă, and S.S. Sastry, "An invitation to 3-D vision: from images to geometric models," Springer-Verlag, 2004.

[74] Z. Zhang, "A flexible new technique for camera calibration," *IEEE Transactions on Pattern Analysis and Machine Intelligence,* Vol.22, No.11, pp. 1330–1334, 2000.

[75] R.S. Blum, and Z. Liu (eds.), *Multi–sensor Image Fusion and Its Applications,* Taylor & Francis, 2006.

[76] D. Drajic, and N. Cvejic, "Adaptive fusion of multimodal surveillance image sequences in visual sensor networks," *IEEE Transactions on Consumer Electronics,* Vol. 53, No. 4, NOVEMBER 2007.

[77] L.R. Foulds, *Graph Theory Applications,* Springer-Verlag, 1992.

[78] Z. Wu, and R. Leahy, "An optimal graph theoretic approach to data clustering: theory and its application to image segmentation," *IEEE Transactions on Pattern Analysis and Machine Intelligence,* 11:1101–1113, 1993.

[79] J. Shi, and J. Malik, Normalized Cuts and Image Segmentation, *IEEE Trans. Pattern Analysis and Machine Intelligence,* vol. 22, no. 8, pp. 888-905, Aug. 2000.

[80] M. Yang, and N.G. Bourbakis, "An Efficient Packet Loss Recovery Methodology for Video Streaming Over IP Networks," *IEEE Trans. on Broadcasting,* VOL. 55, NO. 2, pp.190–200,JUNE 2009.

[81] A. Kandel, H. Bunke, and M. Last (Eds.), *Applied Graph Theory in Computer Vision and Pattern Recognition,* Springer-Verlag Berlin Heidelberg 2007.

[82] I.S. Dhillon, Y. Guan, and B. Kulis, "Weighted Graph Cuts without Eigenvectors: A Multilevel Approach," *IEEE Transactions on Pattern Analysis and Machine Intelligence,,* VOL. 29, NO. 11, pp.1944–1957, 2007.

[83] C.T. Lin, and C.S.G. Lee, "Neural fuzzy systems: a neuro-fuzzy synergism to intelligent systems," Prentice Hall, Upper Saddle River, NJ, 1996.

[84] L. H. Tsoukalas, and R. E. Uhrig, "Fuzzy and neural approaches in Engineering," Jonh Wiley & Sons, New York, NY, 1996.

[85] T. Takagi, and M. Sugeno, "Derivation of fuzzy control rules from human operator's control actions," *Proc. IFAC Symposium on Fuzzy Information, Knowledge Representation and Decision Analysis*, Marseilles, France, pp.55-60, 1983.

[86] J.X. Xu, C.C. Hang, and C. Liu, "Parallel structure and tuning of a fuzzy PID controller," *Automatica*, Vol. 36, pp. 673-684, 2000.

[87] S.Z. He, T.D. Shaoua, and F.L. Xu, "Fuzzy self-tuning of PID," *Fuzzy Sets and Systems*, Vol.56, pp. 37-46, 1993.

[88] W.Z. Qiao, and M. Mizumoto, "PID type fuzzy controller and parameters adaptive method," *Fuzzy Sets and Systems*, Vol. 78, pp. 23-35, 1996.

[89] S.Z. He, T. D. Shaoua, and F.L. Xu, "Fuzzy self-tuning of PID," *Fuzzy Sets and Systems*, Vol.56, pp. 37-46, 1993.

[90] T.T. Huang, H.Y. Chung, and J.J. Lin, "A fuzzy PID controller being like parameter varying PID," *IEEE International Fuzzy Systems Conference Proceeding*, Seoul, Korea, pp.269-275, 1999.

[91] M. Guzelkaya, I. Eksin, and E. Yesil, "Self-tuning of PID-type fuzzy logic controller coefficients via relative rate observer," *Engineering Applications of Artificial Intelligence*, Vol. 16, pp.227-236, 2003.

[92] T. Yang, H. Hu, X. Chen, Y. Chu, and P. Cheng, "A correlation analysis of cooling-induced temperature change," *ASME Journal of Manufacturing Science and Engineering,* Volume 131, Issue 1, Paper No. 011003 (7 pages), 2009.

[93] T. Yang, H. Hu, X. Chen, Y. Chu, and P. Cheng, "Performance of a real-time local thermal management system for casting dies with multiple cooling channels," *International Journal of Manufacturing Research,* Vol. 2, No. 1, pp. 74-87, 2007.

147

[94] T. Yang, X. Chen, and H. Hu, "A fuzzy PID thermal control system for die casting processes," *Proc. 22nd IEEE International Symposium on Intelligent Control,* Singapore, pp.389-394, Oct. 2007.

[95] T. Yang, H. Hu, X. Chen, Y. Chu, and P. Cheng, "A local temperature control system for die casting processes," *Proc. European Metallurgic Conference,* Düsseldorf, Germany, pp. 1305-1316 , June 2007. *Proc. 9th International Conference on Advances in Materials and Processing Technology,* Las Vegas, NV, USA, July 2006.

[96] T. Yang, H. Hu, X. Chen, Y. Chu, and P. Cheng, "Local temperature control for die casting processes," *Proc. 135th TMS Annual Meeting,* San Antonio, TX, USA, pp. 1015-1021, March 2006.

[97] T. Yang, H. Hu, X. Chen, Y. Chu, and P. Cheng, "Thermal analysis of a die cooling system," *Proc. NADCA Transactions,* St. Louis, MO, USA, Paper No. T05-132, 2005.

[98] J. Papai, and C. Mobley, "Die thermal fields and heat fluxes during die casting of 380 aluminum alloy in H-13 steel dies," *Proceedings of the NADCA Congress and Exposition Detroit,* Paper No. Detroit-T91-OC1, October 1991.

[99] S. Bounds, K. Davey, and S. Hinduja, "An Experimental and Numerical Investigation into the Thermal Behavior of the Pressure Die Casting Process," *Transactions of the ASME,* Vol. 122, pp90–99, 2000.

[100] J. Campbell, *Casting,* Butterworth Heinemann, Oxford,1991.

[101] D.R. Poirier, and G.H. Geiger, *Transport Phenomena in Materials Processing,* John Wiley & Sons, 1960.

[102] F.P. Incropera, and D.P. Dewitt, *Introduction to Heat Transfer,* John Wiley & Sons, 1990.

148

[103] L.C. Thomas, *Heat Transfer - Professional Version,* Capstone Publishing Corporation, 1999.

[104] G. Dour, M. Dargusch, C. Davidson, and A. Nef, "Development of a non intrusive heat transfer coefficient gauge and its application to high pressure die casting," *Journal of Materials Processing Technology,* Vol. 169: pp. 223–233,2005

[105] G. H. Golub, and C. F. van Loan, *Matrix Computations,* Johns Hopkins, 2nd. edition, 1989.

[106] A.W.J. Fitzgibbon, *Stable Segmentation of 2D Curves,* Ph.D. Thesis, University of Edinburgh, 1997.

[107] G. Strang, *Linear Algebra and its Applications,* HarcourtBrace Jovanovich, Orlando, FL, 1988.

[108] R. J. Radke, S. Andra, O. Al-Kofahi, and B. Roysam, "Image Change Detection Algorithms: A Systematic Survey," *IEEE Trans. on Image Processing,* VOL. 14, NO. 3, pp.294–307, 2005.

[109] R.A. Farrugia, and C. J. Debono, "A Support Vector Machine Approach for Detection and Localization of Transmission Errors Within Standard H.263++ Decoders," *IEEE Trans. on Multimdia,* VOL. 11, NO. 7, pp.1323–1330, November 2009.

[110] Z. Li, J. Chakareski, X. Niu, Y. Zhang, and W. Gu "Modeling and Analysis of Distortion Caused by Markov-Model Burst Packet Losses in Video Transmission," *IEEE Trans. on Circuits and Systems for Video Technology,* VOL. 19, NO. 7, pp.917–931,July 2009

[111] J. Wang, L. Ju, and X. Wang, "An Edge-Weighted Centroidal Voronoi Tessellation Model for Image Segmentation," *IEEE Trans. on Image Processsing,* VOL. 18, NO. 8, pp. 1844–1858, August 2009.

Vita Auctoris

Name: Tie Bao Yang

Education: Ph.D in Electrical Engineering, 2009 (expected)
               University of Windsor, Canada

               M.A.Sc. in Electrical Engineering, 2005
               University of Windsor, Canada

               B.Eng in Aeronautical Engineering, 1993
               Civil Aviation University of China, PR China

Awards: NSERC Postdoctoral Fellowship, 2010–2012
               NSERC Postgraduate Scholarship–Doctoral, 2007–2009
               Ontario Graduate Scholarship (OGS), 2005–2007
               UWindsor Tuition Scholarship, 2005–2009

Affiliation: Student Member, ASME
               Student Member, IEEE